2016

Monolithically Integrated InP-based Unidirectional Circulators Utilizing non-Hermiticity and Nonlinearity

Parinaz Aleahmad
University of Central Florida

MONOLITHICALLY INTEGRATED INP-BASED UNIDIRECTIONAL CIRCULATORS UTILIZING NON-HERMITICITY AND NONLINEARITY

by

PARINAZ ALEAHMAD
M.S. University of Central Florida, 2012
M.S. University of Toronto , 2011

A dissertation submitted in partial fulfillment of the requirements
for the degree of Doctor of Philosophy
in the College of Optics and Photonics: CREOL
at the University of Central Florida
Orlando, Florida

Spring Term
2016

Major Professor: Demetrios Christodoulides

ABSTRACT

The need to integrate critical optical components on a single chip has been an ongoing quest in both optoelectronics and optical communication systems. Among the possible devices, elements supporting non-reciprocal transmission are of great interest for applications where signal routing and isolation is required. In this respect, breaking reciprocity is typically accomplished via Faraday rotation through appropriate magneto-optical arrangements. Unfortunately, standard light emitting optoelectronic materials like for example III-V semiconductors, lack magneto-optical properties and hence cannot be directly used in this capacity. To address these issues, a number of different tactics have been attempted in the last few years. These range from directly bonding garnets on chip, to parametric structures and unidirectional nonlinear arrangements involving ring resonators, to mention a few [1-4]. Clearly, of importance will be to realize families of non-reciprocal devises that not only can be miniaturized and readily integrated on chip but they also rely on physical processes that are indigenous to the semiconductor wafer itself. Quite recently we have theoretically shown that such unidirectional systems can be implemented, provided one simultaneously exploits the presence of gain/loss processes and optical nonlinearities. In principle, these all-dielectric structures can be broadband, polarization insensitive, color-preserving, and can display appreciable isolation ratios provided they are used under pulsed conditions. In this study, we experimentally demonstrate a compact, monolithically integrated unidirectional 4×4 optical circulator, based on non-reciprocal optical transmission through successive amplification/attenuation stages and elements with very large resonance nonlinearities associated with InGaAsP quantum wells. Our results indicate that isolation ratios

over 20dB can be experimentally achieved in pulse-mode operation. Our design can be effortlessly extended to other existing optoelectronic device systems beyond InP.

In the second part of this report we study the dynamics of accelerating Helmholtz Bessel beams. We present closed form expressions describing the intensity profile of these wavepackets during propagation and we investigate the contribution of evanescent field components. We show that for higher-order Bessel beams, these non-paraxial classes of wave packets can still accelerate on circular trajectories up to 90^{o} even in presence of evanescent components. We have also showed that new families of diffraction-free non-paraxial accelerating optical beams can be generated by considering the symmetries of the underlying vectorial Helmholtz equation. Both two-dimensional transverse electric and magnetic accelerating wave fronts are possible, capable of moving along elliptic trajectories. Experimental results corroborate these predictions when these waves are launched from either the major or minor axis of the ellipse. In addition, three-dimensional spherical non-diffracting field configurations are presented along with their evolution dynamics. Finally, fully vectorial self-similar accelerating optical wave solutions are obtained via oblate-prolate spheroidal wave functions. In all occasions, these effects are illustrated via pertinent examples.

This dissertation is dedicated to my parents and my husband who was extremely patient and supportive with me during all these years

ACKNOWLEDGMENT

Faculty Advisors

Dr. Demetrios Christodoulides

Pegasus Professor of Optics & Photonics/Cobb Family Endowed Chair

CREOL, The College of Optics & Photonics

University of Central Florida

Committee Member

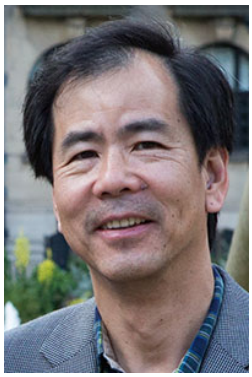

Dr. Patrick L. LiKamWa

Associate Professor of Optics & Photonics, ECE

CREOL, The College of Optics & Photonics

University of Central Florida

Dr. Peter J. Delfyett

University Trustee Chair & Professor of Optics, ECE & Physics

CREOL, The College of Optics & Photonics

University of Central Florida

External Committee Member

Dr. Héctor Manuel Moya-Cessa

ICTP's Regular associate

Fellow of the Mexican Academy of Sciences (AMC - MAS)

I want to take this opportunity to thank my advisers Dr. Demetrios Christodoulides. Being part of the nonlinear waves group (NLW) was a rich experience for me. I feel very fortunate for having this opportunity to interact and learn from him and to take advantage of the great insight he always provided.

I would like to thank Dr. Patrick LikamWa. I'm very gratefull for the chance that he gave me to be part of his group and walking me through my research with his patience and deep insight on the field.

I would also like to extend my thanks to the members of the committee, Dr. Peter J. Delfyett, and Dr. Héctor Manuel Moya-Cessa. I am grateful for their advice and help, kindly given whenever it was sought, particularly in my final years.

I feel very fortunate to have interacted with all the NLW group members. It is because of them that I could build my theoretical as well as experimental skills. I want to thank here the current members of our group, particularly Amin, Absar, and Midya for their support. The discussions with you guys were always eye-opening. I would like to thank past members Armando, Mattew, and Ali who have helped me in so many ways in my research.

I would like to thank Enrique, Miguel, Edris and Jesus for their help and continuous suggestion in fabrication and lab work.

Being part of CREOL was indeed a great experience. The people here were always happy to help and always had a smile on their faces. I would like to thank Rachel Amy, Gail, Mark, Matt, Maria, Richard, for making administrative works simple and giving a pleasant experience from beginning to the end. Particularly, Rachel thank you for the extra effort and care you have put in my PhD, without you things would have been really complicated.

Last, but not least, I would like to thank my parents for their love and support in difficult and disturbing situations. Many thanks to my husband (Mahdi) whose presence was always inspiring. He was not only tolerating me working long hours in lab but also provided moral support in overcoming difficult situations possible. He has always pushed the limit of help and support toward me.

TABLE OF CONTENTS

LIST OF FIGURES

LIST OF TABLES

LIST OF ACRONYMS/ABBREVIATIONS

BOE	Buffered Oxide Etchant
EL	Electroluminescence
FDTD	Finite-difference time-domain
ICP	Inductively Coupled Plasma
IID	Impurity Induced Disordering
IFVD	Impurity Free Vacancy Disordering
MMI	Multimode Interference
MQW	Multiple Quantum Well
PECVD	Plasma Enhanced Chemical Vapor Deposition
PL	Photoluminescence
QW	Quantum Well
QWI	Quantum Well Intermixing
RIE	Reactive Ion Etching
RTA	Rapid Thermal Annealing
SEM	Scanning Electron Microscope
TE	Transverse Electric
TIR	Total Internal Reflection
TM	Transverse Magnetic
WCE	Wet Chemical Etching

CHAPTER 1: INTRODUCTION

1.1. Non-reciprocal nonlinear circulator

Nonreciprocal elements are essential components in many optical systems. In principle however, non-reciprocity is inherently difficult due to the time-reversal symmetry in light matter interaction. Therefore any attempt to make an optical isolator needs a mechanism to break the Lorentz reciprocity[5]. According to the Lorentz reciprocity theorem, two states of excitation with their corresponding magnetic and electric fields of $\vec{H}_1/\vec{E}_1$ and $\vec{H}_2/\vec{E}_2$, should satisfy the following equation.

$$\nabla \cdot(\vec{E}_1 \times \vec{H}_2 - \vec{E}_2 \times \vec{H}_1) = j\omega(\vec{E}_2 \cdot \bar{\bar{\epsilon}}\vec{E}_1 - \vec{E}_1 \cdot \bar{\bar{\epsilon}}\vec{E}_2 - \vec{H}_2 \cdot \bar{\bar{\mu}}\vec{H}_1 + \vec{H}_1 \cdot \bar{\bar{\mu}}\vec{H}_2) \qquad (1.1)$$

The right side of equation (1) would be equal to zero if ϵ and μ were scalars. This is known as reciprocity theorem. Consequently any asymmetry in the permittivity or permeability tensor will yield to the directionality of the light propagation. The most common approach to break this reciprocity relies on the Faraday Effect utilizing magneto-optical materials in the presence of magnetic fields [1, 2, 6-9]. Reciprocity would also be broken under the nonlinear condition where the permittivity is influence by the electric field. This has attracted a lot of attention in recent years from directional coupler in quantum well structures [10], to the PT symmetry broken designs in ring resonators on silicon platforms [3, 4, 11-26]. The latter however present a very narrow spectral band-width isolation due to the high quality factor of the resonators.

Following the imparted motive, by characterizing and fully understating the directional coupler On QW platforms, based on the similar principles, we introduce a novel design for a three and four port circulator. This device is designed to perform in an active status where each port would be monitored electro optically to fulfill its capacity to circulate the light in all four

hands. The following report is a comprehensive explanation of the theory, design, fabrication and measurements of such devices.

1.2. Accelerating diffraction-free beams

Since the prediction and experimental observation of optical Airy beams,[27, 28] there has been a flurry of activities in understanding and utilizing accelerating nondiffracting wave fronts.[29-37]As first indicated within the context of quantum mechanics,[38] Airy wave packets tend to accelerate even in the absence of any external forces—a property arising from the inertial character of free-falling systems in a gravitational environment.[39] Interestingly, Airy waves represent the only possible self-similar accelerating solution to the free-particle Schrödinger equation when considered in one dimension. In optics, this peculiar class of waves is possible under paraxial diffraction conditions provided that they are truncated so as to have a finite norm.[27, 28] In this realm, the intensity features of Airy beams propagate on a parabolic trajectory and exhibit self-healing properties, desirable attributes in a variety of physical settings.[29] In the last few years, such accelerating beams have been utilized in inducing curved plasma filaments,[40] synthesizing versatile bullets of light,[41] carrying out autofocusing and supercontinuum experiments,[42] as well as manipulating microparticles.[29] The one-dimensional nature of these solutions was also successfully exploited in plasmonics.[43-46] Interestingly, shape-preserving accelerating beams can also be found in nonlinear settings, with Kerr, saturable, quadratic, and nonlocal nonlinearities.[47-49] In principle accelerating beams can also be generated though caustics.[33, 34] Yet, such wave fronts are by nature not self-similar and thus cannot propagate over a long distance, a necessary feature to reach large

deflections. Until recently, it was generally believed that shape preserving accelerating beams belong exclusively to the domain of Schrödinger-type equations,[38] which for general waves (e.g., electromagnetic, acoustic, etc.) will only be valid under paraxial conditions. Quite recently, however, nonparaxial, shape-preserving accelerating beams in the form of higher-order Bessel functions have been found as solutions of Maxwell equations[50] and experimentally demonstrated.[51, 52] This new family of waves represents exact vectorial solutions to the two-dimensional Helmholtz equation, and as such they follow circular trajectories (on a quadrant) on which the magnitude of acceleration is constant. Unlike paraxial Airy beams, these nonparaxial waves can in principle intersect the propagation axis at 90, thus considerably expanding their bending horizon. Such behavior can be particularly useful in many and diverse applications such as in nanophotonics where nonparaxiality is absolutely necessary. Apart from optics, these solutions can be similarly realized in other electromagnetic frequency bands as well as in acoustics.

Here it is important to emphasize that all these accelerating wavefronts are solutions to the full vector Maxwell equations in coordinate systems where the Helmholtz problem can be successfully separated. In fact, they correspond to modes in cavity configurations, when the enclosing “perfect metallic boundary” is eventually pushed to infinity. For instance, the Bessel waves (TE or TM) happen to be the circulating modes in a cylindrical cavity, of infinite extent. As a result, when this solution is launched in free space, it tends to self-bend along a circular trajectory, as in a cavity, until the open boundary conditions take a toll. Given that these are highly non-paraxial solutions, of importance will be to understand the role of evanescent contributions on their propagation. In addition, it is not at this point very clear how these beams will dynamically evolve even if they are not truncated. In other words, how will they propagate if

the entire waveform (that in principle extends to infinity) is provided? These questions can only be answered through an exact analytical approach since any numerical attempt has to rely on apodized versions of such beams. Moreover given that Airy beams are unique within 1D paraxial optics, the question naturally arises if the aforementioned higher-order Bessel accelerating diffraction-free waves represent the only possible solution. In other words, are there any other vectorial solutions to the full-Maxwell equations that could in general accelerate along more involved trajectories? If so, can they be extended in the three-dimensional vectorial regime, and are they again self-healing in character?

In this report, we present analytical results describing the evolution of accelerating Helmholtz Bessel beams. The contribution of the evanescent field components on the propagation of these vectorial wavepackets is investigated in detail. We show, that in spite of evanescent components, these non-paraxial Bessel beams can still accelerate up to a point, along circular trajectories, and in doing so they can exhibit large deflections. Both apodized and non-apodized Bessel beam configurations are considered in our study. We have also showed that indeed other families of accelerating nondiffracting wave solutions to Maxwell's equations also exist. [53, 54] By utilizing the underlying symmetries of the corresponding Helmholtz problem, we demonstrate both theoretically and experimentally self-healing vectorial wave fronts—capable of following elliptic trajectories and hence experiencing a nonuniform acceleration. The existence of such beams clearly indicates that shape preservation is not an absolute must in attaining accelerating diffraction-free propagation. In addition, we theoretically explore the dynamics of self-similar accelerating 3D vectorial spherical wave functions along with their power flow characteristics. Other solutions of such classes of 3D accelerating ring wave fronts are also obtained via prolate spheroidal wave functions. Our results may pave the way toward

synthesizing more general classes of accelerating waves for applications in optics and ultrasonics.

1.3. Dissertation outline

The outline of this report is as follows. In chapter 2, we investigate theoretical and numerical beam propagation methods to study and simulate optical wave packet dynamics in directional coupler and circulator devices. Chapter 3 is a comprehensive review of the fabrication process to develop such devices. In chapter 4, we investigate and characterize the quantum well platform including gain and loss along with nonlinear response of the system. The selective band gap tuning of the quantum wells is also discussed in this section. Chapter 5, focus on the setup design and measurements of such devices. Finally in chapter 6, we will switch the topic from nonreciprocal devices to explore the theoretical and numerical investigations of propagation dynamics of fully vectorial accelerating diffraction-free wave packets.

CHAPTER 2: THEORY AND SIMULATION OF THE DEVICE DESIGN

2.1. Theory and beam propagation analysis of the directional coupler

Obeying the wave equation, applying the slowly varying envelope approximation, one can show that the electric fields in two adjacent waveguides in a linear regime can be modeled by a set of coupled equations as follows

$$i\frac{dE_1}{dz} + \beta_1 E_1 + \kappa_{12} E_2 = 0$$

$$i\frac{dE_2}{dz} + \beta_2 E_2 + \kappa_{21} E_1 = 0 \tag{2.1}$$

where E_1 and E_2 refers to the electric fields in first and second waveguides with β_1 and β_2 representing their propagation constants. Here, κ_{21} and κ_{12} are the coupling coefficients. Solving equations (2.1), for the general for of solutions, $E_1 = a(z)e^{i\beta_1 z}$ and $E_2 = b(z)e^{i\beta_2 z}$, the answers demonstrate a harmonic behavior.

$$a(z) = e^{-\frac{i\delta z}{2}}\left\{a_0 \cos\left(\frac{\kappa}{F}z\right) + iF\left(b_0 + \frac{\delta}{2\kappa}a_0\right)\sin\left(\frac{\kappa}{F}z\right)\right\}$$

$$b(z) = e^{\frac{i\delta z}{2}}\left\{b_0 \cos\left(\frac{\kappa}{F}z\right) + iF\left(a_0 - \frac{\delta}{2\kappa}b_0\right)\sin\left(\frac{\kappa}{F}z\right)\right\} \tag{2.2}$$

Where δ is the value of detuning and $\kappa = \kappa_{12} = \kappa_{21}$, with $F = {1}/{\sqrt{1 + \delta^2/4\kappa^2}}$. The above solutions for zero amount of detuning would result in complete switching of power from one waveguide to the other (figure 2.1), however this amount of coupling can be controlled by changing the propagation constant in the waveguides in respect to each other. As an example when ${\delta}/{\kappa} = 4$, this coupling will change to about twenty percent (figure 2.2).

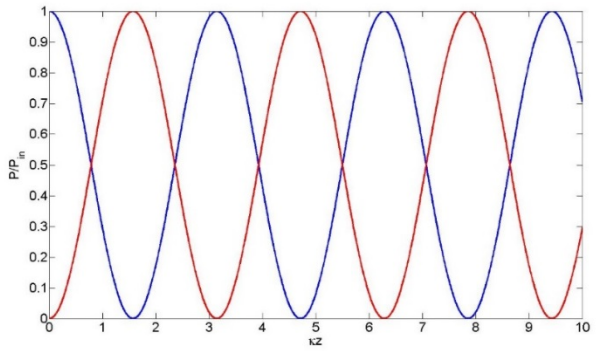

Figure 2.1. Power distribution in directional coupler for zero detuning. Red and blue color indicate waveguide number 1 and 2 respectively.

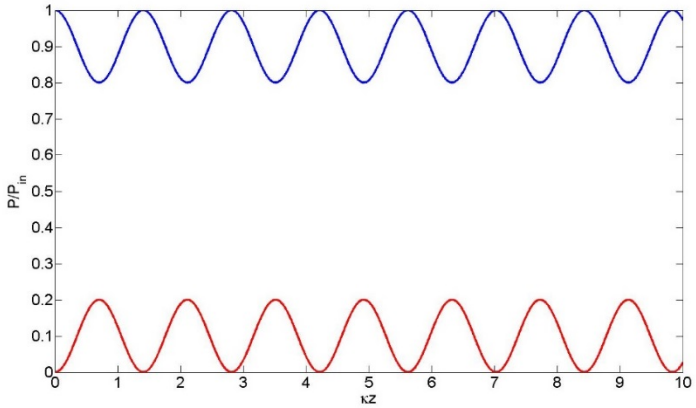

Figure 2.2. Power distribution in directional coupler when $\delta = 4\kappa$. Red and blue color indicate waveguide number 1 and 2 respectively.

One approach to detune the two waveguides is by applying the nonlinearity. In the presence of nonlinearity, equation (2.1) would be modify as

$$i\frac{dE_1}{dz} + \beta_1 E_1 + \kappa_{12} E_2 + \left(k_0 \frac{n_2}{2}\right)|E_1|^2 E_1 = 0$$

$$i\frac{dE_2}{dz} + \beta_2 E_2 + \kappa_{21} E_1 + \left(k_0 \frac{n_2}{2}\right)|E_2|^2 E_2 = 0 \qquad (2.3)$$

with n_2 representing the nonlinear refractive index of the material. A solution to the equation of (2.3) has been proposed using the Stokes parameters in 1985 by B. Daino, et al [55]. These solutions are expressed in terms of Jacobi elliptic functions, $cn(u,m)$ and $dn(u,m)$ where m is the modulus of the elliptic function. Following Daino's method, after few steps of calculations, one can derive the output power of one waveguide in respect to the input power as follows

$$P_{out} = \begin{cases} \frac{P_{in}}{2}\left[1 + cn\left(2Z, \frac{|a_0|^2}{4}\right)\right] & ; \frac{|a_0|^2}{4} \leq 1 \\ \frac{P_{in}}{2}\left[1 + dn\left(\frac{|a_0|^2}{2}Z, \frac{4}{|a_0|^2}\right)\right] & ; \frac{|a_0|^2}{4} > 1 \end{cases} \qquad (2.4)$$

where a_0 indicate the initial amplitude of the field in channel 1. Figure 2.3 shows the cn part of equation (2.4) for different values of a_0, in respect to z. as it is shown in this figure, the $|a_0| = 2$ is a critical power in respect to the oscillatory behavior for these set of functions, for any initial intensity in the range $|a_0|^2 \leq 2$, the power switch back and forth between the waveguides. In dn solutions however (figure 2.4), for the power range of $|a_0|^2 > 4$, although the power oscillate in the launching channel, it will never switch back to the adjacent waveguide thoroughly.

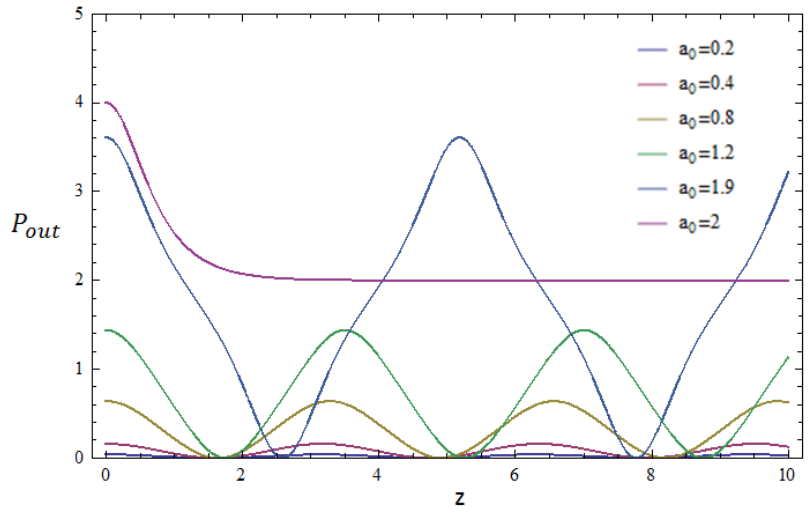

Figure 2.3. Output power behavior for one channel in low intensity nonlinear coupler, cn solutions ($|a_0|^2 \leq 4$).

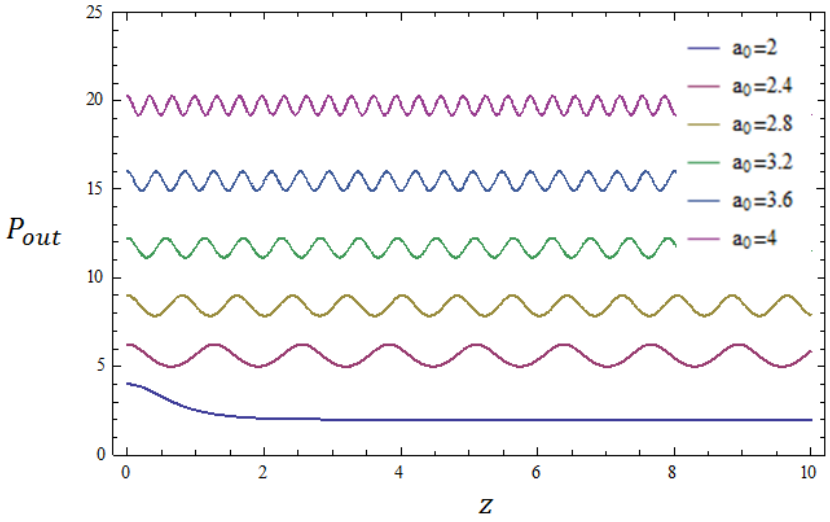

Figure 2.4. Output power behavior for one channel in high intensity limit of nonlinear coupler, dn solutions ($|a_0|^2 > 4$).

To better understand the effect of nonlinearity in these set of solutions, we have plotted the output power in respect to the input power. As it can see from figure 2.5, the oscillatory behavior start to shift from the switching behavior between two channels in the coupler as we increase the input power. One should keep in mind that the expressed analytical solutions in equation 2.4 in

the absence of any loss. In the presence of loss however one should numerically solve the equations to reach an analytical description of the field distributions.

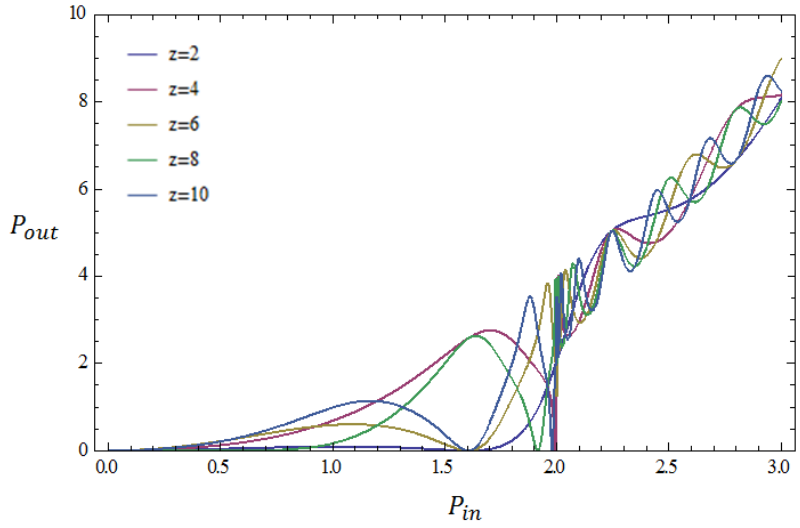

Figure 2.5. Nonlinear directional coupler behavior in respect to the input power.

The first experimental observation of this all optical switching has been performed on a GaAs/GaAlAs multiple-quantum-well structure in 1985 by P. LiKamWa, et al [56]. Later on, other experiments shows the same notion in a dual core fiber and a strained GaAs/InGaAs superlattice[57, 58].

In this study we have exploited numerical beam propagation methods (BPM) to deliver a robust design adequate for easy and standard optoelectronic device fabrication methods. As a consequence a ridge waveguide platform has been employed and designed to ensure a single mode structure to avoid any complexity rising from multiple mode interactions. An important parameter to warrant this latter requirement is the so-called V number defining as

$$V = \frac{2\pi a}{\lambda_0}\sqrt{n_1^2 - n_2^2} \cong \frac{2\pi a}{\lambda_0} n_1 \sqrt{2\Delta} \qquad (2.5)$$

with n_1 and n_2 being the refractive indices of core and cladding respectively. The waveguide is single mode if $V \leq 2.4$. With this considerations in mind, utilizing the “Split-Step Fourier

algorithm", we explored different designs for a ridge waveguide directional coupler. However to find the effective refractive indices of the multiple quantum well (MQW) material, to insert in our one dimensional model in beam propagation, we advantage from COMSOL program to find the equivalent of effective indices in such material. Figure 2. 6 shows the effective refractive index of the core measured to be $n_1 = 3.18$ while figure 2. 7 indicate $n_2 = 3.20$, refractive index of the cladding of our waveguide.

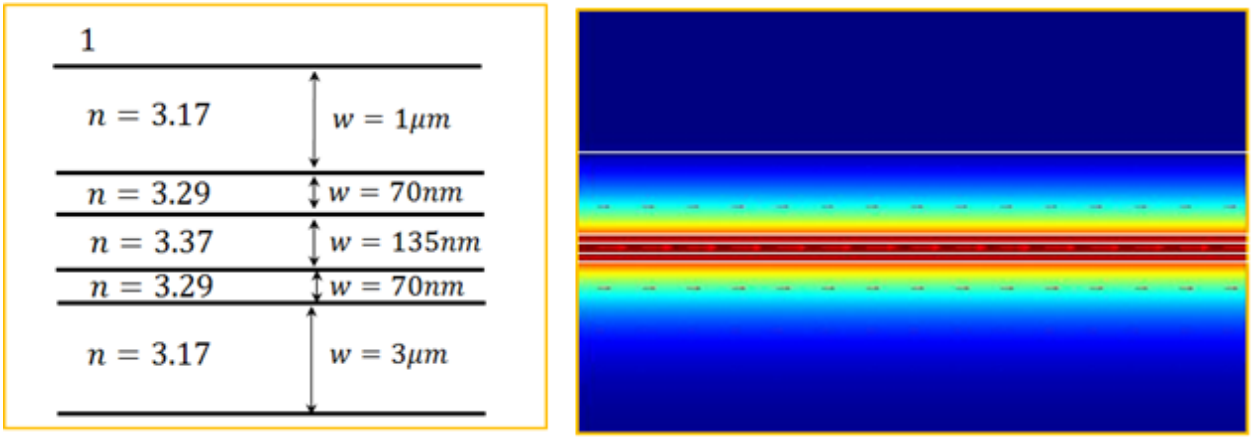

Figure 2. 6. Effective refractive index simulations of the core for a multiple layer quantum well structure from COMSOL.

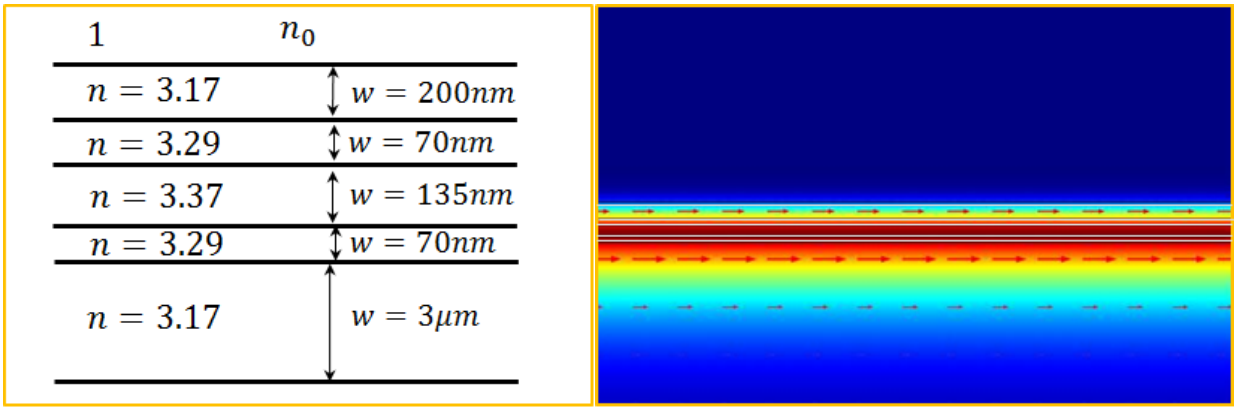

Figure 2. 7. Effective refractive index simulations of the cladding for a MQW structure from COMSOL.

Different waveguide widths have been explored utilizing our BPM to find the best coupling and yet satisfying the condition $V \leq 2.4$ for the single mode criteria. The final design has been set for two waveguides with $2\mu m$ width and spacing of $2\mu m$. A single mode field distribution in such structure is simulated using COMSOL reported in figure 2. 8.

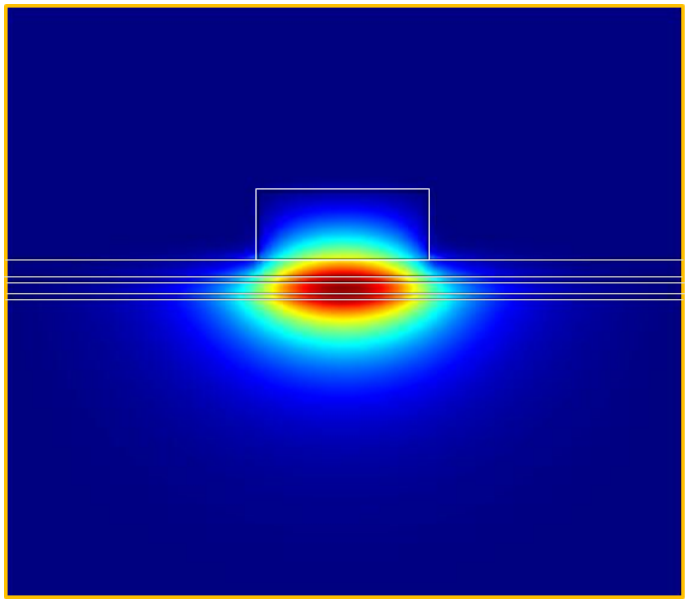

Figure 2.8. Mode shape inside the ridge waveguide of MQW structure.

In the one dimensional BPM, the values for nonlinearity and losses are assumed to our best knowledge from our previous measurements of fabricated devices. In this case the nonlinearity coefficient is set to $n_2 = -10^{-12} m^2/W$, while the amount of loss is assume to be $2000 cm^{-1}$ along the coupler area. The simulations are performed for communication wavelength, $\lambda = 1550 nm$. Figure 2.9 shows the intensity distribution and the coupling length for a structure artificially set to have no loss, while figure 2.10 shows the results considering all the losses. The degree of isolation in first case with no loss is about 22dB, while in the presence of losses it drops to 18dB. In the latter, the coupler is design with a combination of optical amplifiers in a way that the input power equals to the output in both linear and nonlinear regime.

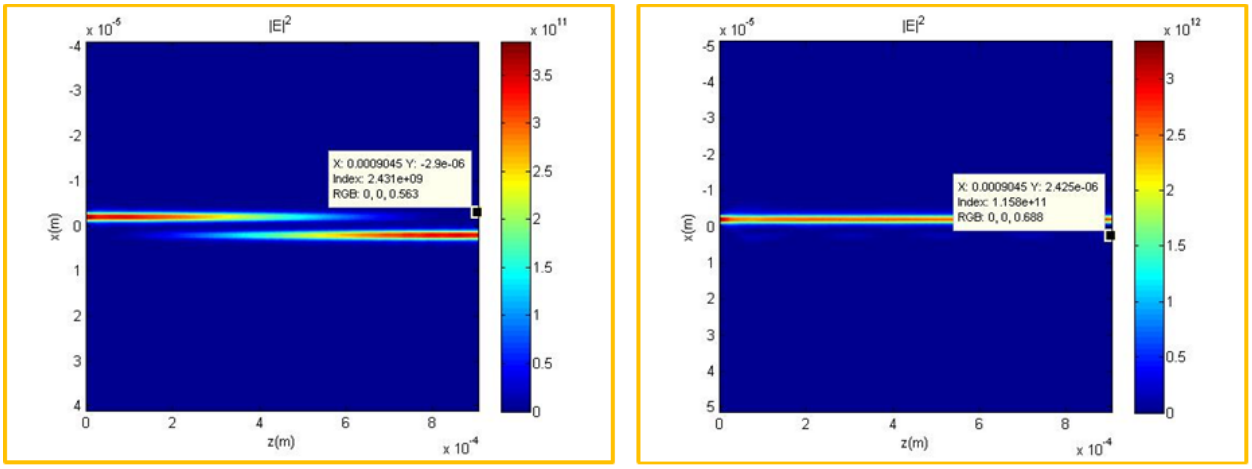

Figure 2.9. BPM results for two adjacent waveguides with $2\mu m$ width each and spacing of $2\mu m$ with no loss. The left shows the linear regime when the power is set to 1mW, while the right figure shows the intensity distribution when the initial power is 10mW.

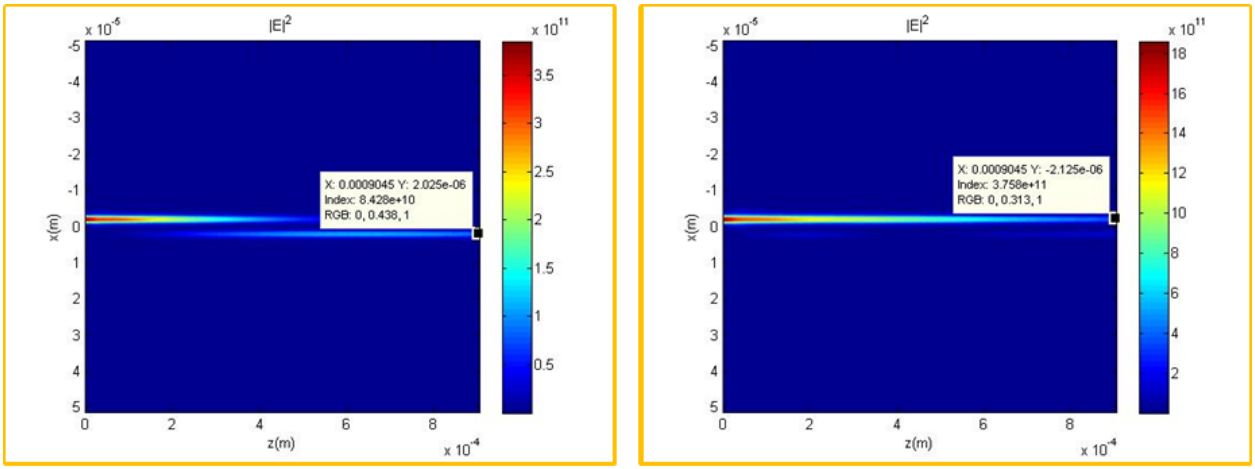

Figure 2.10. BPM results for two adjacent waveguides with $2\mu m$ width each and spacing of $2\mu m$ considering the loss amount of $\alpha = 2000cm^{-}1$ along the propagation. The left shows the linear regime when the power is set to 1mW, while the right figure shows the intensity distribution when the initial power is 10mW.

The single mode field distribution shown in figure 2. 8 is exceptionally susceptible to the ridge waveguide height as one would expect, given that the cladding effective refractive index of the waveguide depend on the etched height. Figure 2. 11 shows the electric field distribution of single mode shape for different ridge waveguide heights where the parameter w, shows the cladding thickness of InP on top of the quantum well structure. As it is expected, for lower values of w, the mode is more confined in the ridge waveguide. Table 2. 1 shows the cladding (n_0), and core (n_1) effective refractive indices for different thickness of the buffered InP on top of quantum wells.

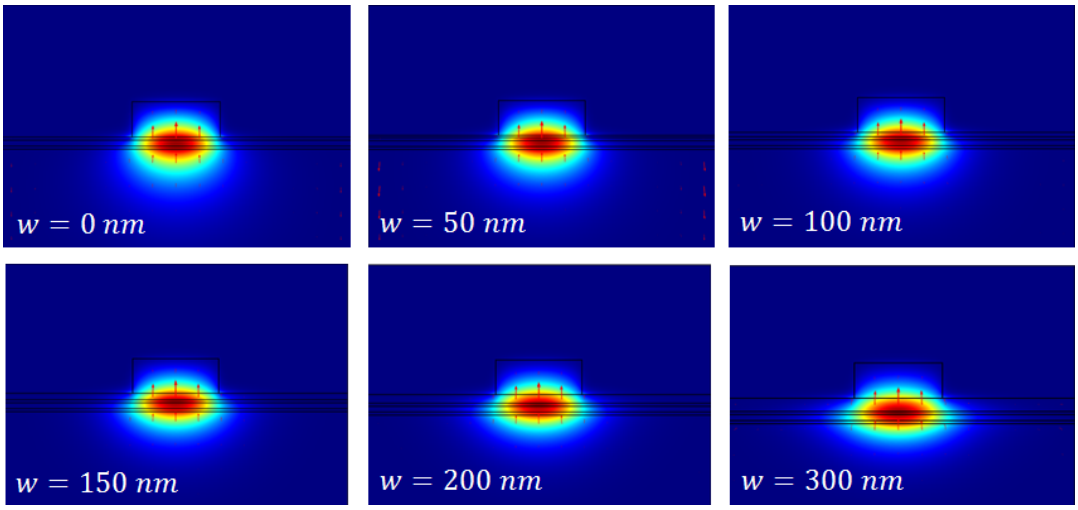

Figure 2. 11. Single mode, electric field distribution in a ridge waveguide with two micron width for different waveguide heights.

Table 2. 1. Effective refractive indices of the cladding (n_0) and core (n_1) for single mode waveguide in respect to remaining thickness of the buffered InP on top of quantum well layer.

W(nm)	$n0_{eff}$	$n1_{eff}$	Δn
0	3.158163	3.208319	0.050156
50	3.167481	3.208319	0.040838
100	3.178121	3.208319	0.030198
150	3.188932	3.208319	0.019387
200	3.199068	3.208319	0.009251
250	3.208166	3.208319	0.000153

Although the mode confinement would be desirable for the passive regions where guiding the light is the main objective, it would be a disadvantage in the coupler section where cross talk between the two adjacent waveguide depends on interaction of the two mode. Figure 2. 12 shows the coupling length in respect to the parameter w.

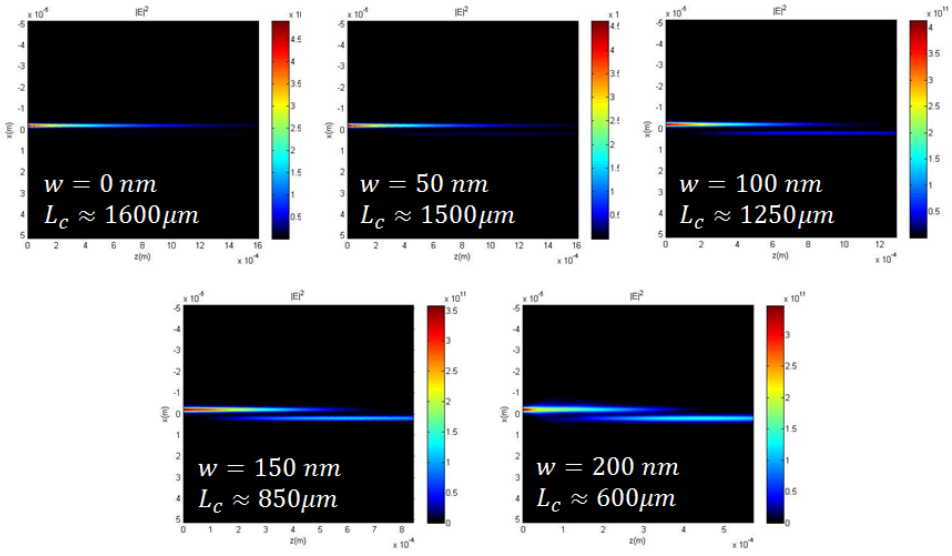

Figure 2. 12. Coupling in two adjacent waveguides with two micron width and two micron separation distance for different ridge waveguide height.

Considering the two results from figure 2. 12 and figure 2. 11, an optimum depth has been simulated and designed in our wafer structure for best mode confinement and reasonable coupling length. The parameter w is finally designed to be $100nm$ in such systems. Yet one can always etch the passive regions, areas with no directional coupler, to reduce the propagation loss. The question remained to be answered is would the mode mismatching, or reflection from passing through one region to the other bring an excessive amount of loss. To answer this question we have investigated the effective mode refractive index for three different ridge waveguide height presented in figure 2. 13. The reflection caused by passing through one region to the other is calculated from

$$R = \left(\frac{n_{eff_1} - n_{eff_2}}{n_{eff_1} + n_{eff_2}}\right)^2 \qquad (2.\ 6)$$

where n_{eff} represent the effective refractive index of the mode propagating in the ridge waveguide.

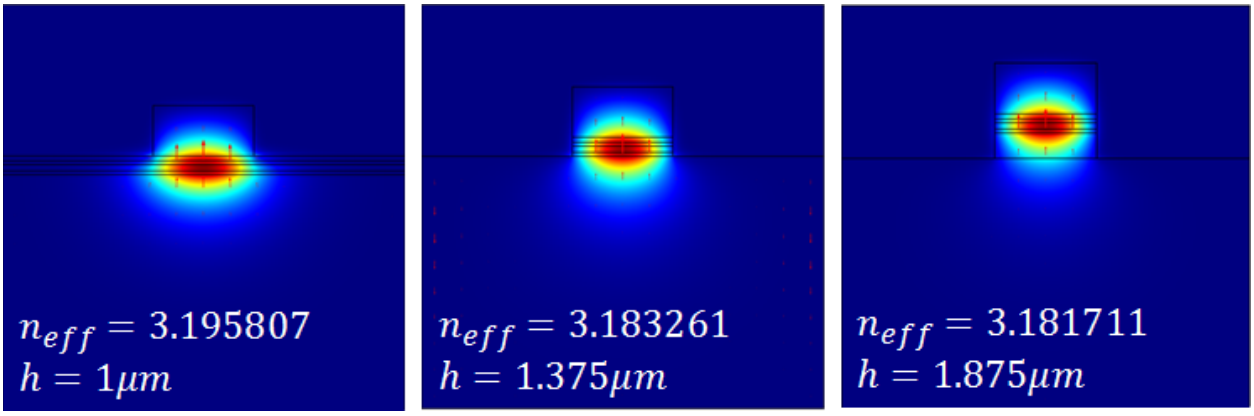

Figure 2. 13. Single mode electrical field distribution in a two micron width ridge waveguide for three different heights.

From equation (2. 6), passing through a ridge waveguide with one micron height to the next with $1.375\mu m$, the mode would experience less than %0.0004 loss which is negligible in respect to the material loss of the system.

2.2. Circulator design and simulations with RSoft

Finding the best design for the directional coupler in our MQW platform, we proceed to the circulator design. Due to the topological concerns of our design, we used the program RSoft to simulate the beam propagation in our structure. Figure 2. 14 shows a first draft of the circulator based on best coupling lengths find in section 2. a, All the distances are expressed in micrometer.

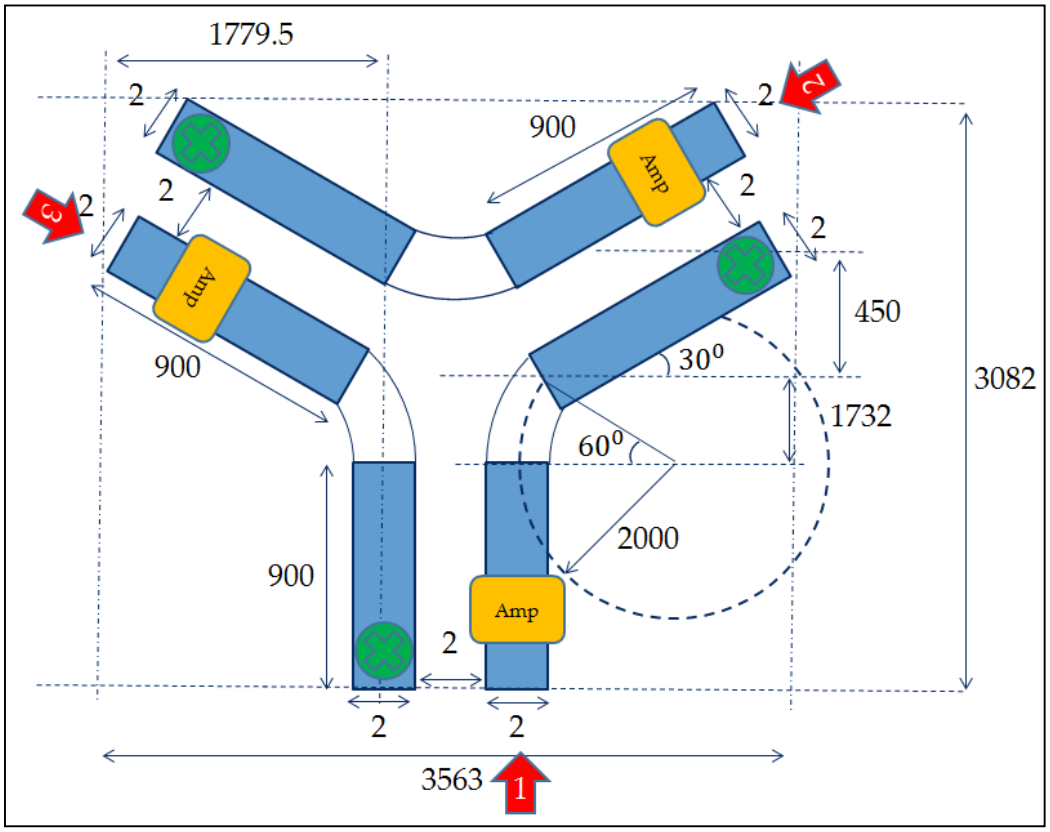

Figure 2. 14. Three port circulator design with directional coupler legs. All the distances are expressed in micrometer.

Launching from port 1, due to the amplification before the coupler, the light will stay in first channel. However after passing the first curve due to all the losses caused by the bending structure, the intensity reaches to low enough values to switch to the port 2. The same concept is valid for switching from port 2 to 3 and 3 to 1 as the structure is symmetrical from the central point. In contrast to the directional coupler, the second channel would be dead end to guarantee the best switching performance. A challenging feature of the design presented in figure 2. 14 is the bending structure. Due to the lateral offset in a bend, significant amount of losses would be introduced in large values of bends ($\sim\theta > 20^0$) as the result of optical mode replacement. However this difficulty can be overcome by increasing the bending radius in a way that the optical wave would experience a slight amount of lateral displacement at each time [59-61]. Different designs have been tested using the RSoft program to achieve the best coupling from input 1 to input 2. The final values are presented in figure 2. 14. Figure 2. 15, shows the electrical field distribution in a circulator design when the light is launched from port 1. As it is shown in this picture, in spite all the losses due to the bend, the ratio of power ended up in port 2 is significantly higher than port 3. In this design the degree of isolation defines as logarithmic ratio of power in port 2 in respect to port 3 is about 38dB. The losses due to the bend, measured as the power ratio right before and after the bend is about seven percent.

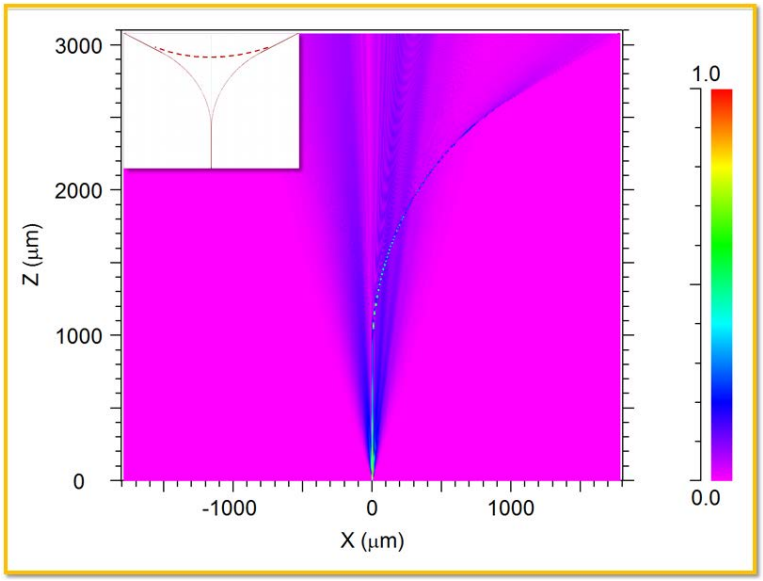

Figure 2. 15. Electrical field distribution in 3-port circulator design when 10mw power is launched from port 1.

Other designs with smaller bending radius shows a significant loss in the bending area and a lower degree of isolation as the consequence.

In addition to the complexity of the large degree bending losses, one should keep in mind that the 3-port design would impose a great deal of obstacles in respect to the measurements and alignments. For this very reason, we have reached a 4 port design utilizing a 45 degree titlted total internal reflection mirrors (TIR) substituted for bending curves. The same approach can be employed for a 3-port design with 60^0 mirrors. Figure 2. 16 present such a design for a 4 port circulator.

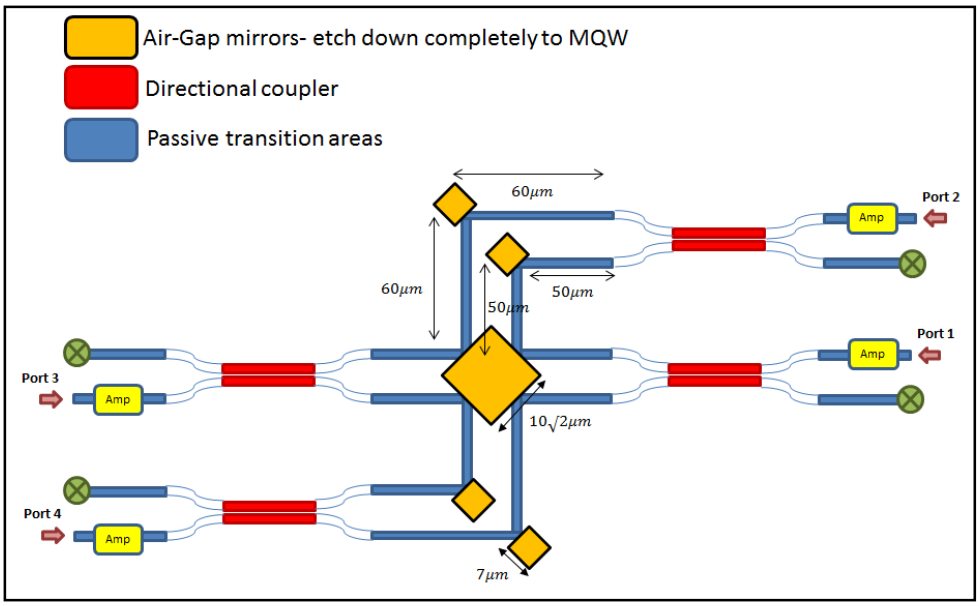

Figure 2. 16. A 4-port circulator with 45^0 TIR mirrors to rotate and guide the wave packet at the center to the next waveguide channel.

This new design not only compensate all the losses from the previous model, but also offer e a compact structure, $70 \times 6500\ \mu m^2$, compatible with common fabrication processes and topologically matching the semiconductor lattice orientations in its cleaving points. As the directional coupler section of this design has been studied before using the BPM, we have only checked the extension, mostly passive parts of the design using RSoft package. Radius and shape of the s-bends are one of those passive areas that has been design to have the minimum loss and maximum transmission of the light from and to the coupler sections. As it is shown in figure 2. 17. a, a transmission of almost hundred percent is expected through a bend with $120\mu m$ length. Total internal reflection mirrors in the centers, a familiar idea in device fabrication [62-66], has been studied using the same simulation package. Figure 2. 17. b and c shows the power transmission through the reflection from such structures. An overall loss of five percent has been predicted through this reflections for each leg.

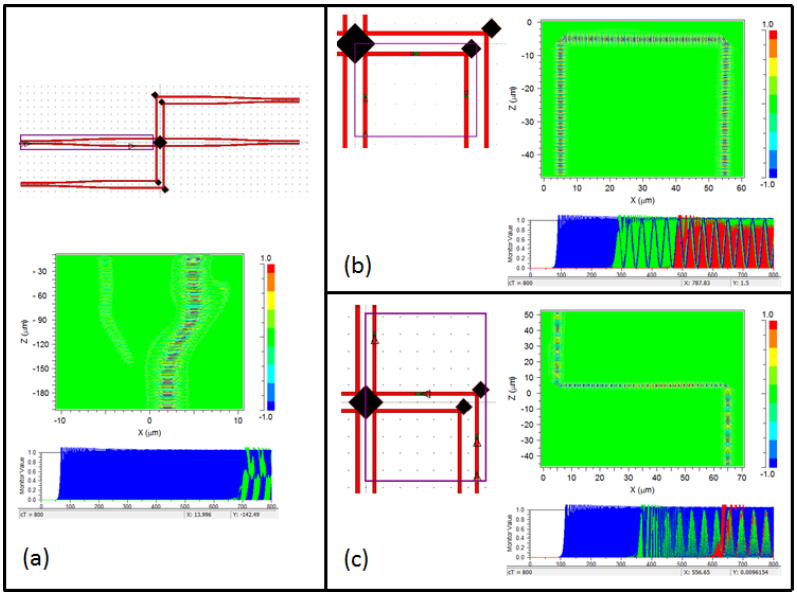

Figure 2. 17. RSoft simulation results for the passive regions of a 4-port circulator where the purple square indicates the area of study on the structure. a) The s-bend transition of optical power. The blue curve monitor the power before and the green monitor it after the curve. b) Power transmission through passing two TIR mirrors, where blue, green and red shows the power monitor values before first mirror, in between, and after the second mirror respectively. c) Power transmission through two mirrors on the extended leg.

CHAPTER 3: MQW STRUCTURE AND DEVICE FABRICATION

3.1. Ridge waveguide fabrication process

In this study we have examined two different MQW wafers (A and B). Both structures involve six InGaAsP quantum wells grown by metal organic chemical vapor deposition (MOCVD) at a commercial semiconductor foundry. Each p-i-n structure is grown epitaxially on a Si doped InP substrate with a 70nm thick undoped InP buffer at the p-i interface. The active region of wafer A consists of six undoped InGaAsP ($\lambda_g = 1.56\,\mu m$) quantum wells each 10nm thick sandwiched between five undoped layers of 15nm thick InGaAsP ($\lambda_g = 1.13\,\mu m$) barriers while that of wafer B consists of six undoped InGaAsP ($\lambda_g = 1.59\,\mu m$) quantum wells each 8nm thick sandwiched between five undoped layers of 15nm thick InGaAsP ($\lambda_g = 1.13\,\mu m$) barriers, where λ_g is the bandgap wavelength. A schematic cross section view of the wafer design is shown in figure 3. 1.

InGaAs p-type	150nm
InP p-type (Zn dopped)	1550nm
InGaAsP U/D	70nm
5×InGaAsP (15nm)/6×InGaAsP(10nm)	
InGaAsP U/D	70nm
InP n-type (Si dopped)	2500nm
InGaAs n-type (Si dopped)	50nm
InP Substrate (Si dopped)	

Figure 3. 1. Schematic cross sectional view of MQW design A grown by MOCVD.

The samples used in this study were ultrasonically cleaned with acetone to remove debris and organic residue from the top layer, followed by rinsing with isopropyl alcohol (IPA) and deionized (DI) water. The samples were then immersed in buffered oxide etch (BOE) to remove any native oxide from the surface. Then a sacrificial layer of 200nm SiN has been deposited using plasma-enhanced chemical vapor deposition (PECVD), to be used as etching mask (Table 3. 1). The pattering of the waveguides is done using photolithography with the positive photoresist S-1805 (Table 3. 2).

Table 3. 1. Sacrificial SiN PECVD recipe.

Pressure(mTorr)	900
Temp(oC)	250
RF Power	20
N_2 (sccm)	400
SiH_4 (sccm)	120
NH_3 (sccm)	4.56
Ratio(nm/min)	9

Table 3. 2. Spin-coat recipe for positive photoresist S1805.

Spin (S1805)	3500 (rpm) / 40 (sec)
Soft-Bake	120^0C / 4 (min)
UV Exposure	12 mW/cm^2 / 5.5 (sec)
Develop 351/DI Water (1:7)	25 (sec)
Hard-Bake	120^0C / 4 (min)

Table 3. 3. PECVD etch recipe for SiN films.

Pressure(mTorr)	75
RF Power	100
O_2 (sccm)	1
CF_4 (sccm)	12
Ratio(nm/min)	67

The SiN film then has been etched using the PECVD machine with the recipe presented in table 3. 3 for 5minutes and 15 seconds. We then removed the photoresist mask by immersing the sample in acetone on 100^0C hot plate for 5 minutes.

Due to the gas type limitation in our PECVD machine, the specific reactive ion etching (RIE) for InP based materials was not available at the time. For this very reason we chose chemical acid-based etch recipes for our coupler device. After removing the photoresist, to remove the top InGaAs layer, the sample were immersed in the solution $H_3PO_4 : H_2O_2 : H_2O$ with the proportion of $1:1:30$ respectively. The ratio of this chemical etch is measured to be around $125\ nm/min$ and the next layer (InP) would properly act as an etch stop film. As the wet InP etch is highly sensitive to the photoresist, after the first layer etch, we have cleaned the sample under RIE ash removal recipe with O_2/He clean for about 20 minutes. The second layer, InP, is etched with using $HCL : H_3PO_4$ with fractions of $1:1$. This later wet etch is rather fast in respect to the previous step which is followed by an InGaAs etch stop cover beneath. The etch rate was measured to be $1\mu m/min$. Finally the sacrificial layers on top has been removed completely using the RIE etch for SiN mask.

Later on another step has been added to our wet etch recipe, as it was explained before in chapter 2, the mode coupling in two adjacent waveguides is highly sensitive to the remaining top

InP layer before the diffusion protection layers InGaAsP. On the other hand, on the single waveguide paths, deeper the ridge waveguide height is, we have a better mode confinement and lower loss as the consequence. Thus we have added a step where we protect coupler section with the same sacrificial SiN layer, except this time we have opened some areas in between where we could etch the rest of the device deeper to achieve a better confinement and yet protecting our directional coupler. Figure 3. 2 shows the scanning electron microscopy (SEM) pictures of the final coupler device. This device has been fabricated to merely characterize the losses and the directional coupler, thus it only include the coupler section design.

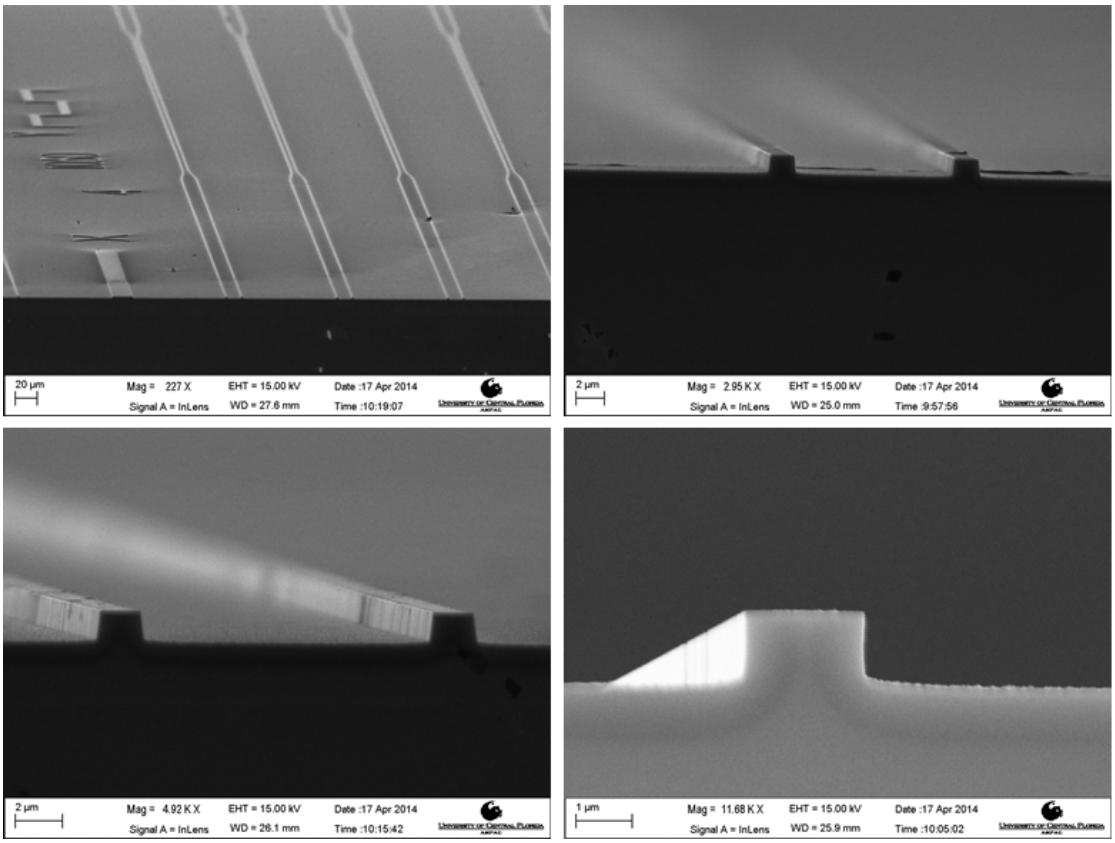

Figure 3. 2. SEM pictures of the coupler device.

The wet etch recipe works ideally for the coupler device where we had only straight waveguides. However one should keep in mind that our wet etch recipe is highly anisotropic where the etched profile depends on the orientation of the wafer. This could bring some complexity in the circulator design, where we have 45^o tilted mirrors. Figure 3. 3, shows this profile after the wet etch. As it is clear in figure 3. 3. a, due to anisotropic behavior of the wet etch, the 45^o mirrors profile would be tilted toward the waveguide structure. This can be confirmed by figure 3. 3. b, where we have removed the sacrificial top mask. To resolve this issue, we have moved to RIE based dry etch. Figure 3. 4 shows the mirror profiles after the dry etch while table 3. 4 shows the RIE recipe used in this step.

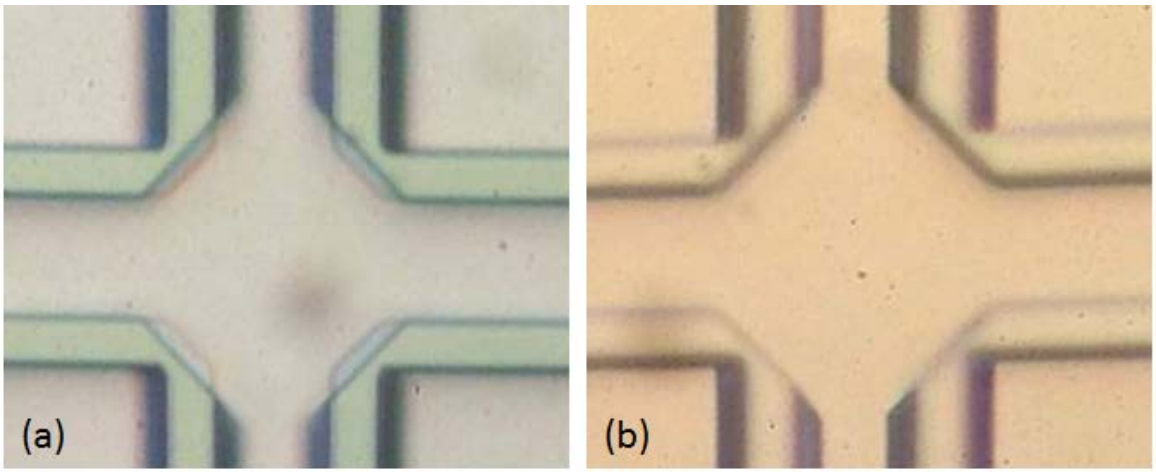

Figure 3. 3. Mirror profile using the wet etch recipe. a) with SiO2 mask on top. b) After removing the mask.

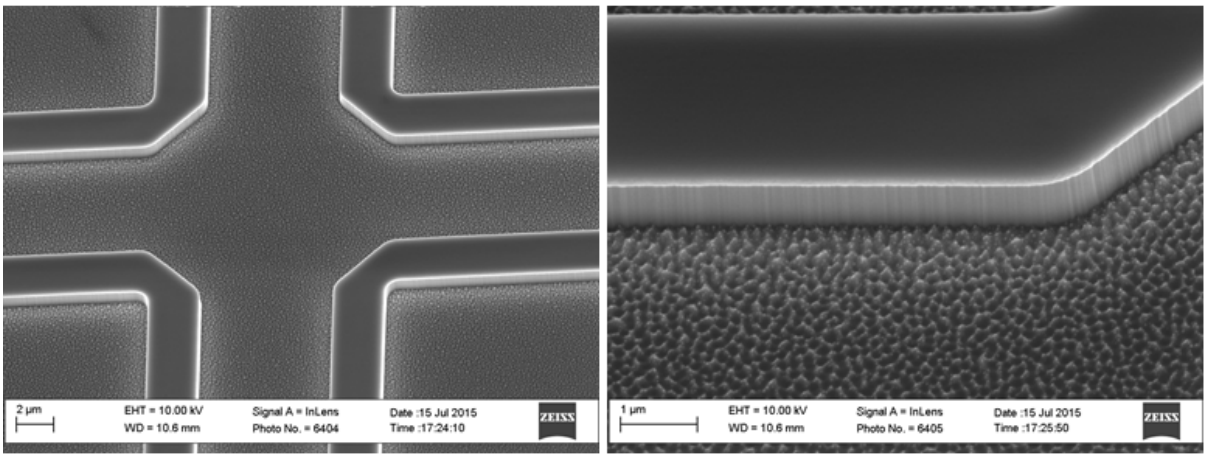

Figure 3. 4. SEM pictures of the circulator design etched with RIE.

Table 3. 4. RIE etch recipe for InP.

Pressure(mTorr)	5
Temp(oC)	25
ICP Power(w)	200
RF Power(w)	100
CH_4 (sccm)	17
H_2 (sccm)	8
Ar (sccm)	5
Ratio(nm/min)	120

Recall that the mirrors has to be etched through the quantum wells to perform as total internal reflection planes. Thus with the same approach in the coupler device, the directional coupler has been protected in the circulator design using a sacrificial SiN mask, while all other regions has been etched down through the quantum wells.

3.2. Active device process and metal contacts

After making the ridge waveguides for both circulator and directional coupler designs, the device would be ready for its final step of fabrication. Metal contacts has been designed properly to be fabricated on the p-i-n junction to serve as an semiconductor optical amplifiers (SOA), which would later be controlled actively through the measurement. To put the metal contacts, we need to first deposit a dielectric layer to planarize the underlying topography and thus provide a flat plane for subsequent metallic layers. For this purpose we have employed the Cyclotene resin, commercially known as BCB, for its unique planarization properties. In this process, the BCB has been span on each device with 3500rpm for 40 seconds. To solidify this resin then we put the samples in an oven to be cured for two hours in 250^oC. Having the solid resin we etched the

BCB using RIE etch up to the level where the top surface of the waveguides appears. We then spin and develop a negative photoresist NR7-1000 PY, to pattern the metal pads and later assist the lift-off process for the protected areas. For the top contacts, we deposit 10nm of titanium proceed by 4nm of zinc and 300nm of gold. After lift-off process, to fuse the metals we cure the samples in a rapid thermal annealing (RTA) machine for 30 seconds at 430^oC. The back side of the sample then is being polished and thinned up to $120\mu m$. We then deposit 4nm of nickel proceed with 20nm of germanium and 220nm of gold. The sample is then ready to be cleaved and tested in the measurement. Figure 3. 5. a and b shows the final appearance of the coupler device after the metal deposition while figure 3. 5. c and d present a complete circulator device from top view.

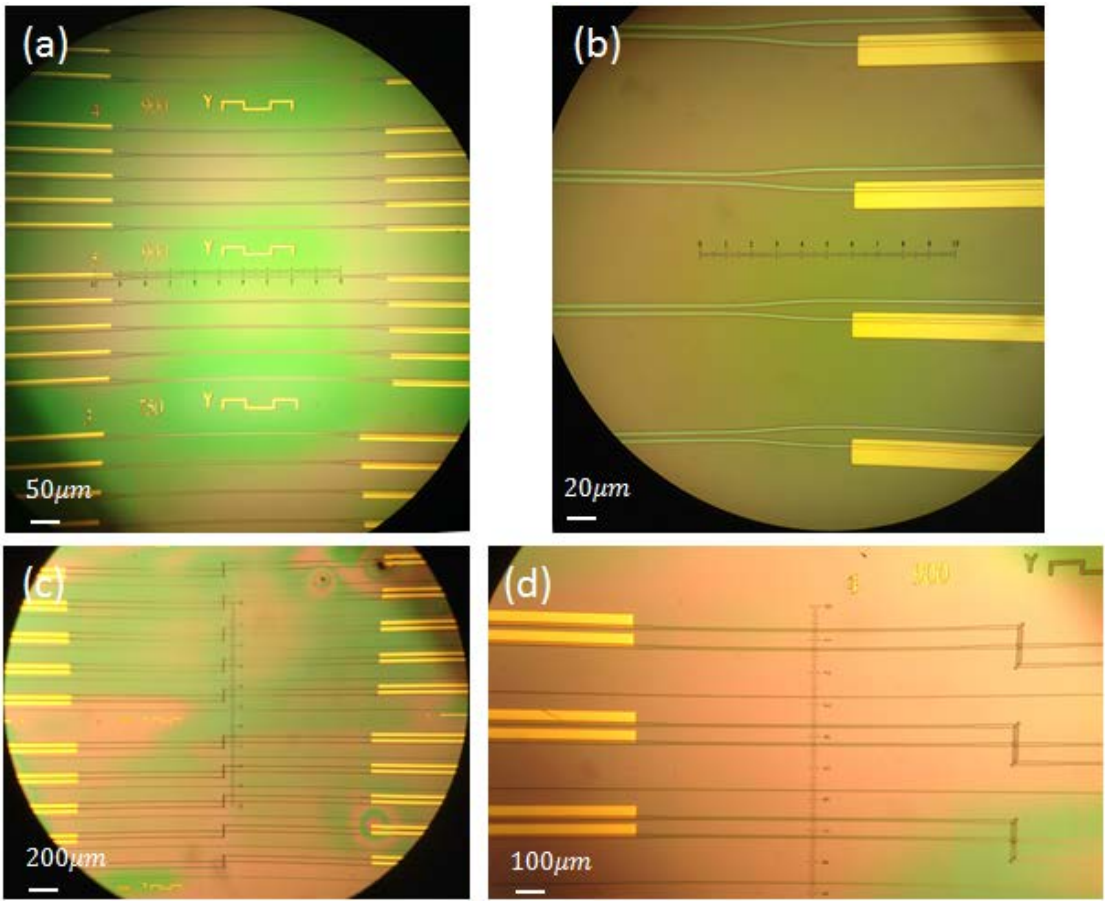

Figure 3. 5. a) Finalize active coupler device with metal pads. b) Complete circulator device.

.

CHAPTER 4: QUANTUM WELL AND RIDGE WAVEGUIDE CHARACTERIZATION

4.1. Selective area bandgap tuning of multiple quantum well structures

To reduce the amount of loss in the passive areas where the only objective is guiding the light we prefer to tune the bandgap in favor of minimum losses. Selective area bandgap tuning of multiple quantum well structures has been an ongoing task in optoelectronic device fabrication in the past few decades [67-83]. This matter is of particular importance in the fabrication of high-performance laser diodes (LD) and photonic integrated circuits (PIC) [84-88]. Among the variety of available techniques a great deal of attention has been focused on induced disordering of MQWs by impurity-free vacancy diffusion (IFVD), due to its inherent spatial selectivity between adjacent regions and its ability to conserve the electrical properties of the disordered and non-disordered sections alike. IFVD techniques however, rely on the application of a capping layer, usually SiO2 /SiNx, which promotes the out-diffusion of Ga from the top surface of the wafer into the dielectric film, thus leaving vacancies in the group III sub-lattice during a high temperature rapid thermal annealing. While relative simplicity of IFVD is an asset, the degree of intermixing that can be achieved through this technique is significantly susceptible to the film properties, the specific structure of MQW, the annealing conditions and even the duration of surface exposure to radio-frequency plasma during reactive ion etching [81, 83].

In the intermixing of InGaAsP MQW's, a SiO2 cap is usually employed to achieve considerable blue shift to the bandgap transition wavelength of up to 100nm [76, 77, 80], while a SiN cap behaves as an inhibitor to the intermixing process. On rare occasions, the MQW region covered by the SiNx cap undergoes a very slight bandgap change after the rapid thermal

annealing [76, 77, 80]. In this work we demonstrate a significant range in the degree of bandgap modification (up to 140nm in wavelength shift towards the blue wavelengths and 120nm towards the red wavelengths) by manipulating the chemical compositions of the SiOyNx and SiNx films. These bandgap tunings have been determined by measuring the room temperature photoluminescence spectra of the disordered MQW's samples. The reduction in the bandgap energy is also corroborated by measuring the emission spectra of several semiconductor optical amplifier (SOA) waveguide strips, fabricated on the MQW wafer that was covered by SiNx during the rapid thermal annealing.

In this study we have examined two different MQW wafers (A and B). Both structures involve six InGaAsP quantum wells grown by metal organic chemical vapor deposition (MOCVD) at a commercial semiconductor foundry. Each p-i-n structure is grown epitaxially on a Si doped InP substrate with a 70nm thick undoped InP buffer at the p-i interface. The active region of wafer A consists of six undoped InGaAsP (λ_g=1.56 μm) quantum wells each 10nm thick sandwiched between five undoped layers of 15nm thick InGaAsP (λ_g=1.13 μm) barriers while that of wafer B consists of six undoped InGaAsP (λ_g=1.59 μm) quantum wells each 8nm thick sandwiched between five undoped layers of 15nm thick InGaAsP (λ_g=1.13 μm) barriers, where λ_g is the bandgap wavelength. A schematic cross section view of the wafer design is shown in figure 4. 1.

InGaAs p-type	150nm
InP p-type (Zn dopped)	1550nm
InGaAsP U/D	70nm
5×InGaAsP (15nm)/6×InGaAsP(10nm)	
InGaAsP U/D	70nm
InP n-type (Si dopped)	2500nm
InGaAs n-type (Si dopped)	50nm
InP Substrate (Si dopped)	

Figure 4. 1. Schematic cross sectional view of MQW design A grown by MOCVD.

The samples used in this study were ultrasonically cleaned with acetone to remove debris and organic residue from the top layer, followed by rinsing with isopropyl alcohol (IPA) and deionized (DI) water. The samples were then immersed in buffered oxide etch (BOE) to remove any native oxide from the surface. In order to study the dependence of bandgap tuning of the MQWs on the different dielectric capping layers, a number of samples are prepared with a variety of SiO2, SiNx and SiOyNx films grown by plasma-enhanced chemical vapor deposition (PECVD). After each individual sample was coated with a film of SiNx or SiOyNx, the film was removed over half of the surface using a photoresist mask and reactive-ion etching (RIE). After having removed the photoresist, a final layer of SiO2 is grown by PECVD to cover everything. Consequently all the samples contain two sections, an area that is covered by a single layer of SiO2 and the remaining area that is covered with either SiNx or SiOyNx followed by an over-layer of SiO2. The latter is expected to perform as an inhibitor for the intermixing. To formulate SiOyNx films with various compositions, the ratio of N2O to NH3 used in the PECVD process is varied from five to one in small steps. Evidently a higher ratio of N2O/NH3 results in a SiOyNx

film with a larger oxygen content and hence the film has a lower refractive index. On the other hand, the SiNx film is grown in the absence of any N2O gas, and the composition is controlled by varying the ratio of SiH4 to NH3 during the PECVD process. In this case, higher SiH4 to NH3 ratios lead to Si rich films which have higher refractive indices. Therefore the refractive index of the film was used as a measure of the composition of SiNx or SiOyNx. Our PECVD machine utilizes a 2% silane gas (SiH4) pre-diluted with nitrogen gas and the SiNx films are usually under high tensile stress. By adding N2 and He to the growth recipes, the tensile or compressive behavior of the SiNx films can be controlled. However it was found that there was always some residual stress in the films and the only effective way to prevent film cracking during high temperature anneals was to limit the thickness of the SiNx/SiOyNx films to less than 50nm. In this study, the thickness of the SiNx/SiOyNx films was kept at 30nm as a good compromise between repeatability and film robustness to high temperature anneals. On the other hand the thickness of the SiO2 film that is expected to promote the intermixing, is kept at 200 nm for all the samples. Each sample was treated individually in a rapid thermal annealer (RTA) for 30 sec at 800oC. During the RTA process, the MQW samples were sandwiched between two GaAs wafers to maintain an As over-pressure and minimize the outgassing of As from the samples. Figure 4. 2 outlines the characteristic changes of the photoluminescence (PL) spectra measured at room temperature for the samples of MQW wafer A that were covered with different film compositions and annealed at 800°C for 30s. The absolute values of PL peak shift from that of the as-grown sample is plotted in figure 4. 2 as a function of the refractive indices of the covering films. The down-pointing and up-pointing triangles correspond to samples covered with SiOyNx and SiNx respectively. Overall, the shift of the PL peak that was obtained using the different film compositions is in the range of -140nm to +120nm. The results shown in figure 4.

2 indicate that the SiOyNx films that were grown using PECVD processes containing N2O in the gas mixture, tend to result in blue shifts of the PL peak, similar to SiO2 films, but to varying degrees depending on the ratio of NH3 to N2O mixtures.

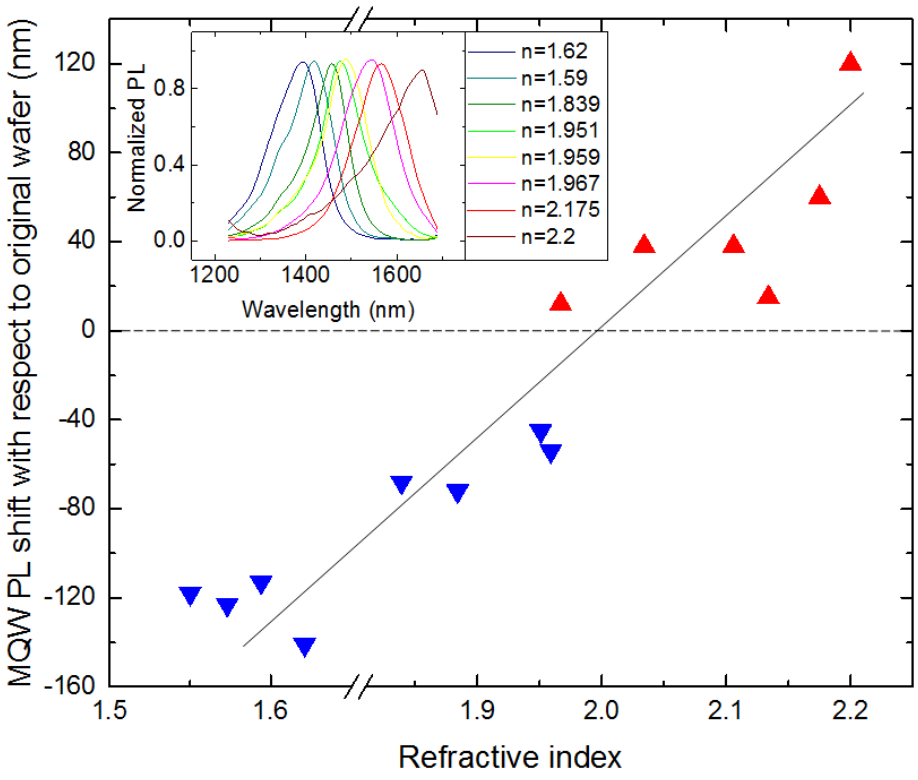

Figure 4. 2. Absolute value of the PL shift measured from RTA treated samples capped with different dielectric films, with respect to the refractive index of the film. The blue shift associated with SiON films for different ratios of NH3/N2O, while the red shift refers Si-rich compositions. The inset shows the absolute PL spectrum for selected data points.

Larger ratios of NH3/N2O produce SiOyNx films that contain larger x/y ratios with correspondingly higher refractive indices, and tend to shift the PL to a longer wavelength. In the absence of N2O during the PECVD process, the SiNx films lead to red shifting of the PL peak. However, it was observed that the degree of the PL peak shift could be controlled by the ratio of

SiH4 to NH3 gases during the PECVD growth of the capping film. A larger ratio of SiH4/NH3 leads to a film of higher refractive index which is consistent with a Si-rich film that results in a MQW disordering with more bandgap narrowing. The SiO2 covered sections of all these samples exhibited a blue shift of 140nm in the PL peak. Table 4. 1 shows a summary of the pertinent parameters that were employed in the PECVD growth of the SiOyNx /SiNx films.

Table 4. 1. Recipes for SiN/ SiO_yN_x film composition sorted with respect to their refractive index;

	Power(W)	Temp(oC)	SiH_4(sccm)	NH_3(sccm)	N_2O(sccm)	N_2(sccm)	HE(sccm)	Index of Refraction
1	150	300	200	4	20	800	0	1.55
2	100	250	200	10	35	600	0	1.573
3	100	250	200	10	29	600	0	1.594
4	150	300	180	3.5	10	800	0	1.621
5	150	300	180	3.5	5	800	0	1.839
6	100	250	180	4.2	0	200	219	1.884
7	150	300	180	4	0	0	450	1.951
8	150	300	200	4	4	800	0	1.959
9	100	250	240	4	0	200	219	1.967
10	150	300	180	4.2	0	200	219	2.034
11	150	300	180	3.75	0	200	219	2.106
12	150	300	200	4	0	800	0	2.134
13	150	300	220	4	0	200	219	2.175
14	150	300	200	3.5	0	800	0	2.2

Noting the compelling nature of this new observation of significant bandgap narrowing caused by selective area intermixing of InGaAsP MQWs, we decided to verify this technique of bandgap tuning using SiNx films of varying Si compositions on the MQWs wafer B. To reduce any other unintended influences, in the growth of the SiNx films, the SiH4, He and N2 mass flow rates as well as the plasma rf power and the substrate temperature were all kept constant while changing the NH3 flow for all different recipes. Figure 4. 3 shows the photoluminescence results of MQW PL shift toward red, treated with RTA and dielectric films with varying Si concentrations. The results clearly show a red shifting of the PL peak emission for Si-rich

compositions of SiNx with the largest shift occurring when the ratio of SiH4 to NH3 is highest during the PECVD process.

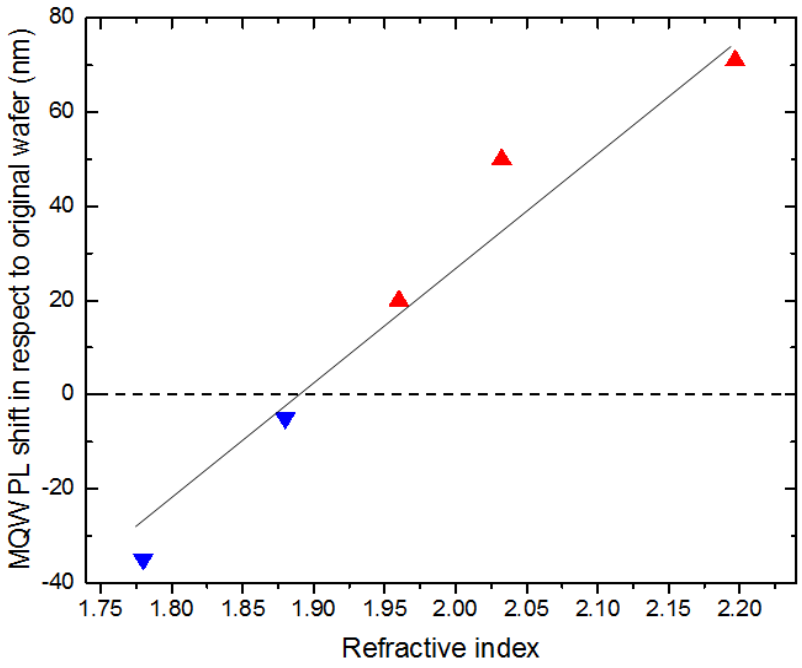

Figure 4. 3. Blue/Red shift report implying Si-rich films on a MQW structure

In order to eliminate the potential of the red-shifted PL spectra being caused by an unintended imbedded layer in the semiconductor wafer, the cladding coating of the wafer shown in figure 1 has been removed layer by layer and the photoluminescence spectrum of the wafer is measurement each time separately. As a result no change was revealed in the PL spectrum of a red shifted sample. To investigate this issue further, the electroluminescence spectrum of both red and blue shifted samples was obtained (Fig. 4. 4). This measurement was performed utilizing a semiconductor optical amplifier (SOA) fabricated on a waveguide strip.

In conclusion, we have presented a thorough study of broad bandgap tuning for InGaAs(P)/InP based multi-structure quantum wells, up to 140nm toward blue and 120nm toward red parts of the spectrum employing SiOyNx /SiNx PECVD growth films. We examined new techniques to achieve absolute red shifts of the bandgap with selectivity over a broad spectrum. This process is controlled by the Si concentration in the film compositions.

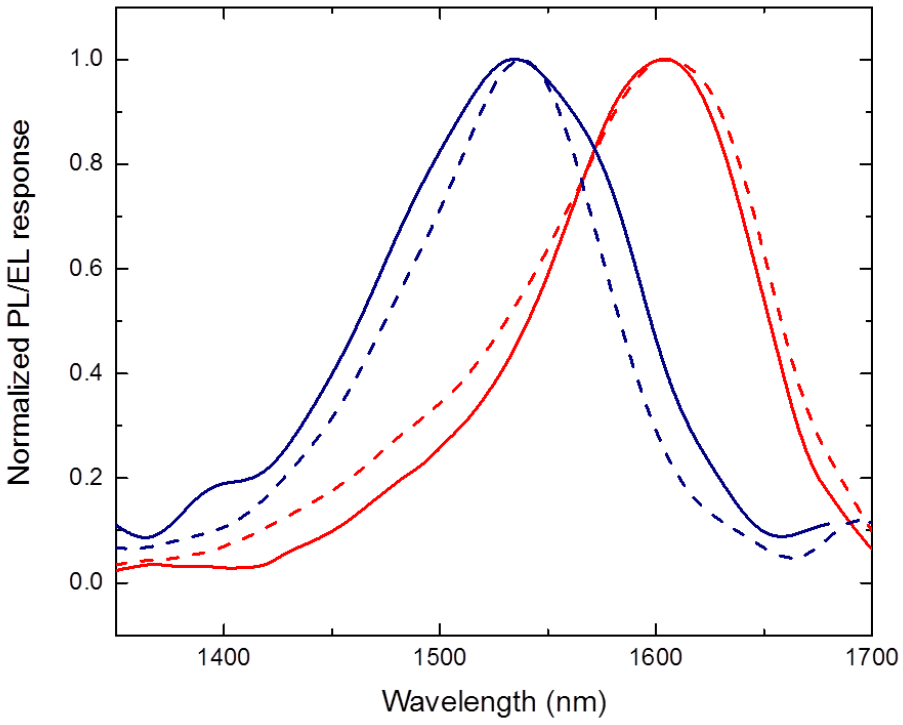

Figure 4. 4. The electroluminescence and photoluminescence response of a red shifted and a blue shifted sample. The solid line indicates the PL while the dash line represents the EL spectrum.

4.2. Waveguide loss measurements

As explained in the previous section, the passive region bandpag, excluding the directional coupler, is tuned to a shorter wavelength in respect to the pump laser to reduce the amount of material loss. In this section, we have characterized the optical losses for both shifted and preserved regions of the device.

Figure 4. 5 shows photoluminescence (PL) measurement performed using an optical spectrum analyzer (OSA), of a typical sample with two sections of blue shifted (a) and red shifted (b) bandgaps for passive and coupler/SOA regions respectively. We have then fabricated ridge waveguides, similar to the ones that we have on our devices, to measure the losses.

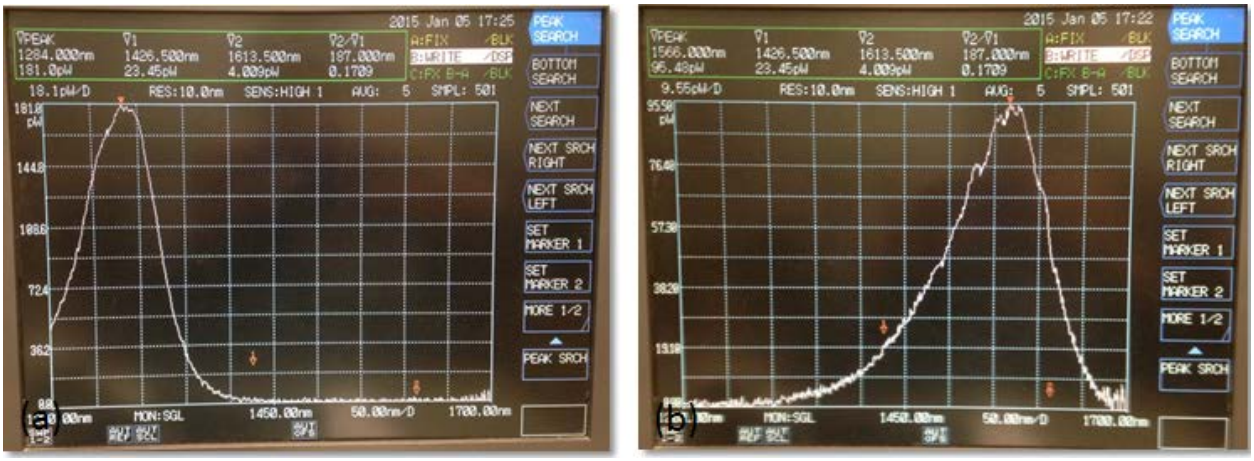

Figure 4. 5. a) Photoluminescence spectrum of a blue shifted sample measured with an OSA. b) PL of a red shifted sample.

Two general approaches has been adopted in these set of measurements. In the first method, by scanning through each waveguide we have utilized the Fabry-Perot fringes generated from a straight waveguide to measure the loss coefficient directly from the fringe visibility. For a Fabry-Perot cavity with losses we have

$$\frac{I_t}{I_i} = \frac{E_t E_t^*}{E_i^2} = \frac{(1-R)^2 \exp(-\alpha l)}{1 + R^2 \exp(-2\alpha l) - 2R cos(2\beta) \exp(-\alpha l)} \quad (4.1)$$

with R define as $R = \left(n_0 - n_{eff}/n_0 + n_{eff}\right)^2$. From equation 4. 1 one can find the loss coefficient as the following

$$\alpha = \frac{\ln\left(\frac{R(V-1)}{V+1-2\sqrt{V}}\right)}{L} \quad (4.2)$$

Here the V is the visibility and it's define as

$$V = \frac{T_{max}}{\left(T_{min,1} + T_{min,1}\right)/2} \quad (4.3)$$

with T_{max} and T_{min} expressed as

$$T_{max} = \frac{(1-R)^2 \exp(-\alpha l)}{1 + R^2 \exp(-2\alpha l) - 2R \exp(-\alpha l)} \quad (4.4)$$

$$T_{min} = \frac{(1-R)^2 \exp(-\alpha l)}{1 + R^2 \exp(-2\alpha l) + 2R \exp(-\alpha l)} \quad (4.4)$$

derived directly through equation 4. 1.

One should keep in mind that in this method the scan steps should be accurate enough to recognize the free spectral range of the Fabry-Perot, $\Delta\nu_{fsr} = c/2L'$, where c is the speed of light and L' is the optical path define as $L' = n_r L cos\theta$ with n_r being the effective refractive index of our single mode coupled into the waveguide. Substituting the values, for free spectral range in our system we find $\Delta\lambda \sim 0.2674nm$. However the full width half maximum (FWHM) the laser reported from the company is $<100KHz \rightarrow 0.155nm$ for $1550nm$. In this case we expect our loss measurements from Fabry-Perot fringes to be slightly higher than the actual losses due

to the possible overlap of these fringes as the FWHM of the laser is only about half of the free spectral range of our fringes.

Using 40x microscope objective we couple the light into our devices. The laser source used in this experiment is a broad band tunable laser, lightwave measurement system model 8164A. Another 20X objective is responsible to collect the transmitted light right after the sample. We then measure the output intensity using a THORLABS InGaAs amplified photodetector. The setup will be discuss in more detail in chapter 5. We first scan the sample with high resolution (0.01nm steps) in a short range of 1575nm to 1580nm for the red shifted sample and 1565-1570nm for blue shifted. After removing the background current of the photodiode and smoothen the data by averaging on five adjacent points, the loss parameter (α) can be found directly from fringe visibility of data recorded by the photodiode using equation 4. 2, for each wavelength.

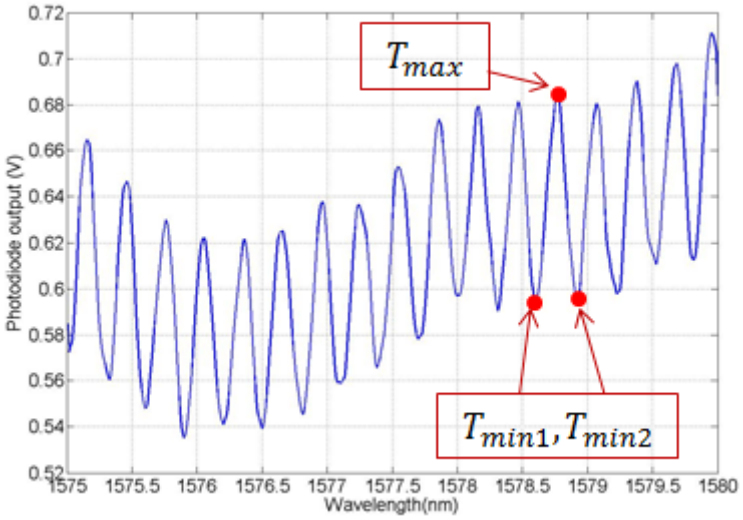

Figure 4. 6. Photodetector respond in respect to wavelength change for a light passing through a blue-shifted ridge waveguide.

Figure 4. 6 shows the photodiode respond for a typical blue-shifted sample. The Fabry-Perot fringes are evident in this figure. Having the loss coefficient for a small range of spectrum through the Fabry-Perot fringes, we then scan the sample with lower resolution (0.5nm) for longer range (from 1530-1580nm). We then collect the output power by the photodiode, smoothing the data by averaging on 30 adjacent points. We call this P_2. In a separate measurement we find the input power (P_1) by removing the sample and collecting the laser spectral passing through all the optical elements excluding the sample and objectives.

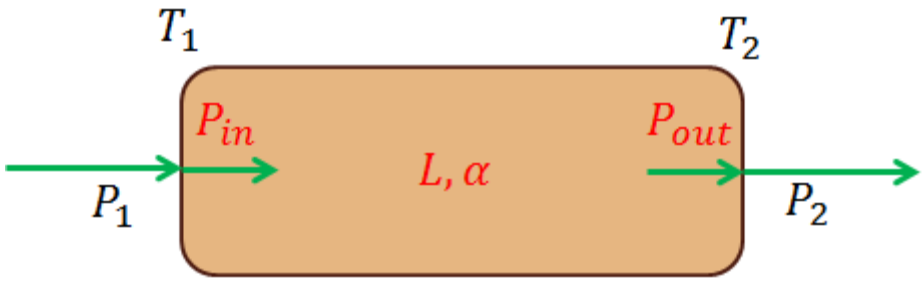

Figure 4. 7. Defining input and output power inside and outside a close box system.

The actual powers inside the Fabry-Perot resonator is related to the outside system powers by relations:

$$P_{in} = P_1 \times T_1$$

$$P_{out} = P_2 \times T_2 \tag{4.5}$$

Following the definition for loss, having the actual input and output powers, one can derive a new formula for loss coefficient with a correction factor that can be measured through a comparison of direct loss measurements with the one from Fabry-Perot fringes as follow:

$$\frac{P_{out}}{P_{in}} = \exp(-\alpha.L) = \frac{P_2}{P_1}.\frac{1}{T_1T_2} \rightarrow \alpha.L = \ln\left(\frac{P_1}{P_2}\right) + \ln(T_1T_2)$$

$$\alpha = \frac{1}{L}\ln\left(\frac{P_1}{P_2}\right) + \frac{\ln(T_1T_2)}{L}$$

$$\alpha = \frac{1}{L}\ln\left(\frac{P_1}{P_2}\right) + \alpha_{corr} \qquad (4.6)$$

Using this α_{corr} and having P_1 and P_2 for the whole spectrum (1530-1580nm) we found the loss coefficient for ridge waveguides for two blue/red shifted regions by averaging over 10 different waveguides. Figure 4. 8 shows the result of this measurements where SiN covered indicated the red shifted area and SiO_2 denote blue shifted waveguides.

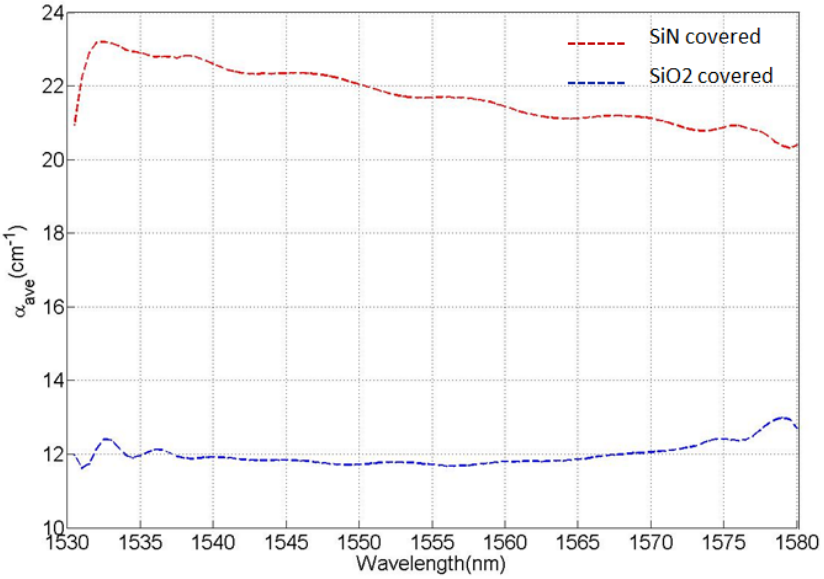

Figure 4. 8. Loss spectrum for a blue/red bandgap shifted (SiO2/SiN covered) waveguides by averaging over results from 10 waveguides.

4.3. Characterization of nonlinear response of InGaAsP quantum wells

A significant distinction in optical properties rise in a multi-structure quantum well (MQW) in respect to a bulk semiconductor material, due to its quantum confinement. A relatively smooth absorption spectrum in bulk materials give its way to a sharp, enhanced excitonic interaction, resulting in step like absorption spectrum influenced by discrete energy levels of the quantum

well in valance and conduction band. These excitonic interactions rise to a new interesting optical effects that can only be seen in such quantum confined structures. The band filling effect is among those, where for high optical power in a very short time, due to optical absorption the conduction band become occupied with electrons while the valance band is populated with holes. As a results, the electrons from the valance band require a greater amount of energy to fill in the conduction band and the absorption spectrum is blue shifted. Following the Kramers-Kronig relations, one can refer to this change in the absorption to obtain a change in the refractive index. In this chapter we tried to measure and characterized this refractive index change.

Typically to measure the nonlinear refractive index, one should monitor the phase change in respect to optical power intensity of a light passing through the material. Figure 4. 9 shows a Mach-Zehnder free space interferometer we designed for this measurement.

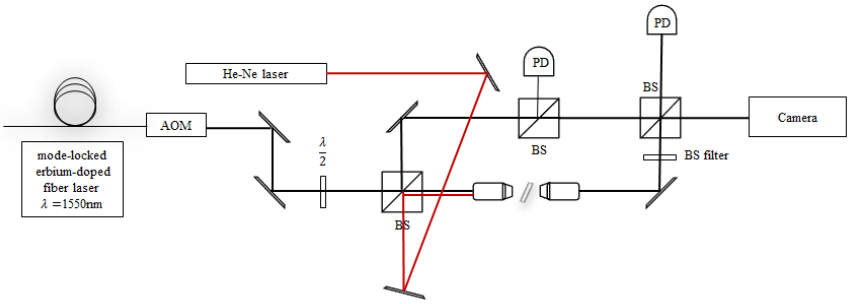

Figure 4. 9. The Mach-Zehnder free space interferometer design to measure the phase change occurs in MQW due to the refractive index change for high optical powers.

The nonlinear refractive index coefficient can be measured from

$$\Delta\phi = \frac{2\pi}{\lambda} n_2 \Delta I L \qquad (4.7)$$

where λ is the frequency of the light, and L present the length of the sample. The optical light intensity change, ΔI, can be translated with the optical power through the definition $\Delta I = \Delta P_0/dA$, with dA defines through our ridge waveguide effective mode size. As the result, the nonlinear refractive index can be measured through

$$n_2 = \frac{\Delta m \cdot \lambda}{\Delta P_0 \cdot L} dA \tag{4.8}$$

with Δm being the number of fringes moved due to the change of peak power ΔP_0. One should keep in mind that the change of power by itself is not sufficient to measure the nonlinear phase change, as the average power variation can bring thermal positive nonlinear effects into play which might compensate the negative nonlinear in the transparent region due to absorption change. To make sure we factored out the influence of average power, we have only changed the intensity by pulsing the source power. The light source in this measurement is an erbium doped mode lucked fiber laser pumped with a diode laser, with the frequency of 26MHz. We have externally pulsed this laser, using a free space acousto-optic modulator to keep the average power the same with controlling the pulse width, while the intensity is changed using the pulse height. The peak power in this case is given by

$$P_0 = \frac{TP_{avg}}{t} \tag{4.9}$$

where the T refers to pulse repetition time and t indicates pulse width. The repetition T remains at $2\mu s$ during all the measurements while the t is changed from 100 to $950ns$. The height of the pulses is fixed accordingly to keep the average power identical in one set of experiment. A correction factor from comparison of the loss measurement in the previous section is used to find the actual power coupled intro the device. Figure 4. 10 shows a typical fringe movement for $\lambda = 1560nm$, when the pulse width is changing from 100 to $950ns$. The same measurement has

been repeated for different wavelengths. Figure 4. 11, shows the nonlinear coefficients measured for different wavelengths from equation 4. 8. The results are in agreement with our expectations from the wafer design in order of magnitude.

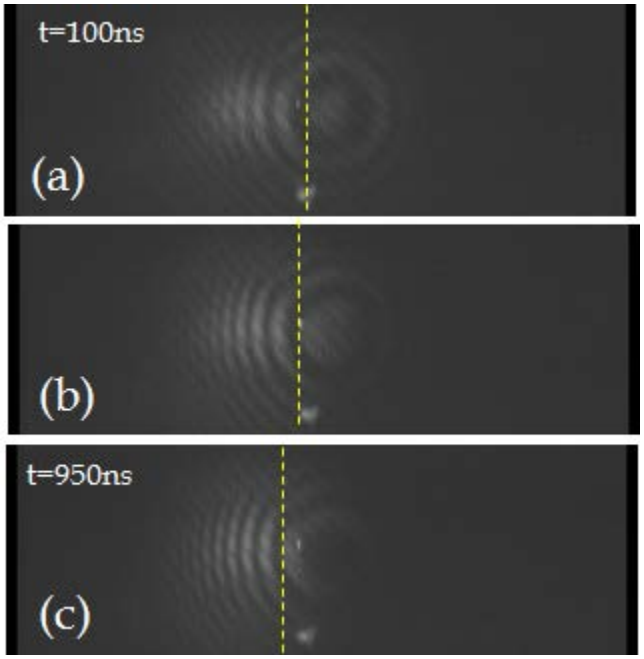

Figure 4. 10. Fringe movement due to intensity variation of the input light for $\lambda = 1560nm$.

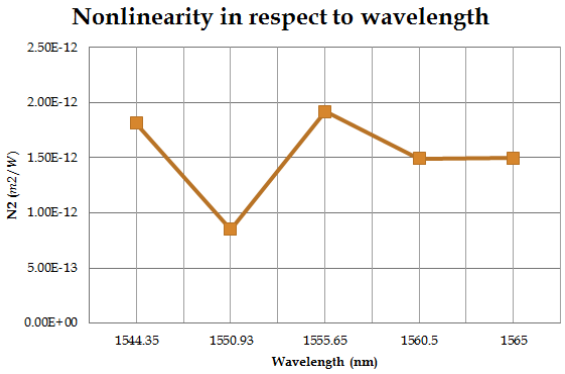

Figure 4. 11. Nonlinear coefficient measured for different wavelengths in InGaAsP quantum well waveguides.

4.4. Gain calibrations and semiconductor optical amplifier device characterization

Finding a healthy absorption spectrum from the quantum well platform, one should expect and appreciable amplified spontaneous emission (ASE) and stimulated emission in such an environment in the presence of free carrier injection. To characterize these properties, we have fabricated semiconductor optical amplifiers (SOA) to measure and calibrate the gain. This chapter is a summary on our SOA device measurements and its characterization.

Metal contacts has been fabricated on ridge waveguides with different widths as explained in section 3. b. Following the same method as expressed in section 4. b, a SOA device could be considered as a Fabry-Perot cavity with gain medium and consequently the gain coefficient could be characterized directly from the Fabry-Perot fringe visibility[89]. However one should keep in mind that a SOA is not a Fabry-Perot resonator cavity by itself as the feedback is killed from each facet. On the other hand the gain measurement through a laser device, in the presence of the feedback, is going to be misleading as for above the threshold current, lasing can filter out a specific mode and as a consequence the result gain coefficient is expressing a partial contribution of the actual gain. Then again, below the threshold, a net gain

would be measured as the results of loss presence. However a laser device could be very beneficial as through direct measurement of Fabry-Perot fringes one could measure and exact point were both the losses and gain compensate each other in a way that $\alpha = \gamma = 0$, which is called the transparency point. The point $\gamma_{net} = 0$ occurs slightly below the threshold, before the lasing start to happen. Finding this threshold current, one could then characterized a SOA device to measure the actual gain spectrum.

Gain coefficient in a Fabry-Perot resonator can be obtained from the fringe visibility utilizing the formula

$$\gamma_{net} = \ln\left[\frac{\mathrm{R} \times (v-1)}{v+1-2\times\sqrt{v}}\right] \tag{4.10}$$

where again in the same manner as loss measurements, v represent the visibility of the fringes and R express the reflectivity of the waveguide facets. Figure 4. 11 represent equation 4. 10, where the net gain is plotted in respect to the visibility. As it is shown in this figure, the point $v = 3.36085$ is the critical visibility were the net gain is zero and our point of interest.

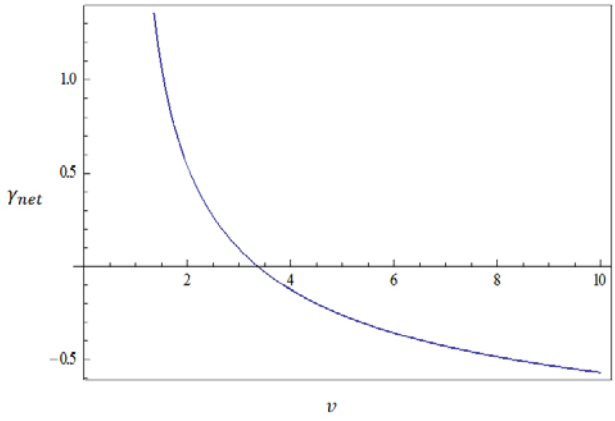

Figure 4. 12. Net gain in respect to Fabry-Perot fringe visibility.

The P-I curve of a laser device has been obtained in figure 4. 13 to locate the threshold current. From this figure, I_{th} is measured around $75mA$. The gain measurements then has been performed on the SOA device for the currents higher than this I_{th}. In the SOA device the feedback from the facets has been destroyed by depositing 200nm layer of SiN on each end, which eventually broadened the FWHM of the lasing spectra from less than1nm in laser device to 35nm for 100mA current applied.

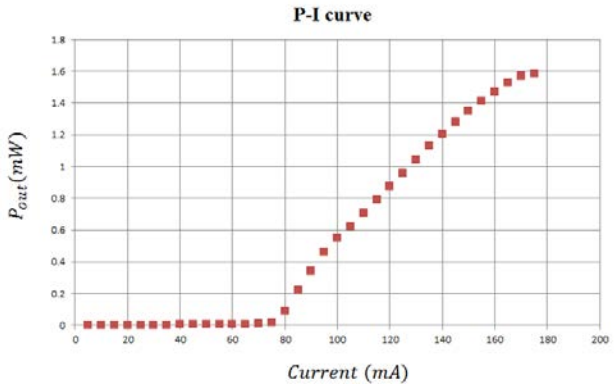

Figure 4. 13. The P_I curve of a laser device fabricate on quantum well structure to characterize the threshold current.

One should keep in mind that the net gain value would be zero only for one specific point. The actual gain coefficient then can be normalized using the net gain values for below and above this transparency turning position. To characterize this gain spectrum for different currents, we have found the net gain coefficient for a laser device below the threshold for different currents (figure 4. 14).

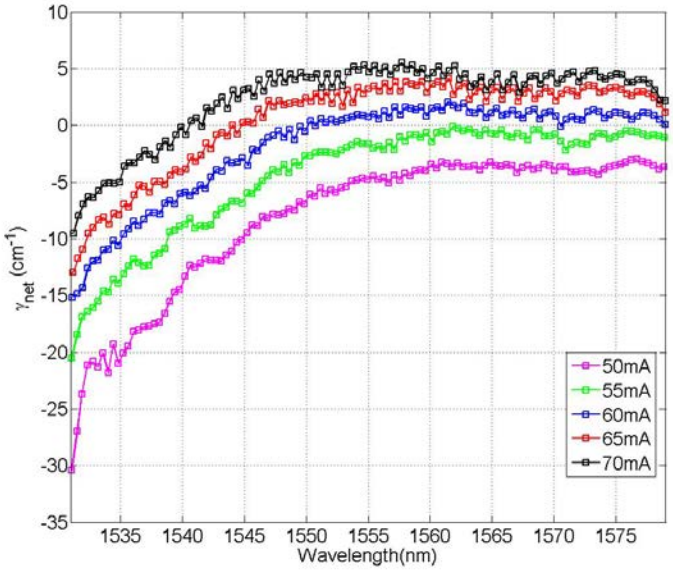

Figure 4. 14. Net gain measured for a laser device directly from the Fabry-Perot fringes for currents below the threshold.

The actual gain then has been collected through the direct input/output power measurement with considering the correction of net gain obtained through figure 4. 14. Figure 4. 15 shows the final results of gain measurement in such medium.

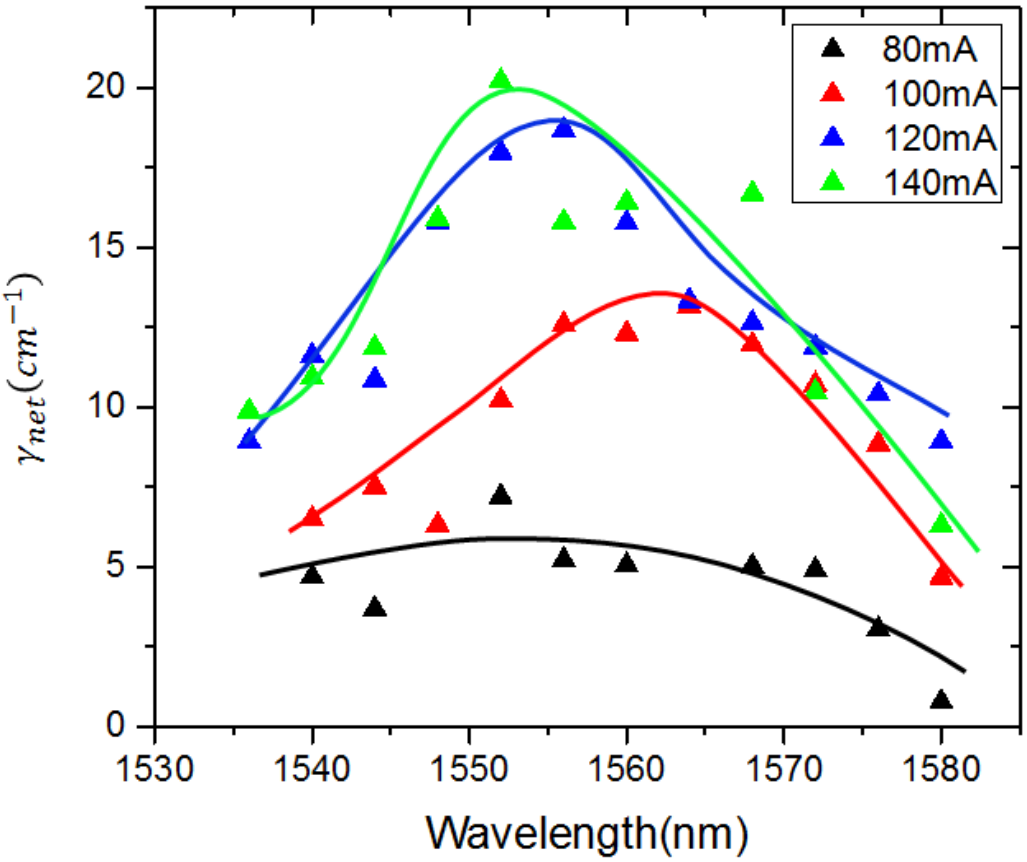

Figure 4. 15. Gain spectrum for currents above threshold for SOA devices.

CHAPTER 5: EXPERIMENTAL SETUP AND DEVICE MEASUREMENTS

5.1. General measurement setup design

The setup prepared to measure o devices has two general component. A visible light for alignment and the original tunable Erbium-doped mode locked fiber laser performing at 1550nm. Figure 5. 1 shows a schematic view of the designed experimental setup. An IR camera is provided to observe the mode shape collected from the sample and an extra optical free space branch is added for Mach-Zehnder interferometer design. The input light is pulsed through an acousto-optic modulator to control the intensity and distinguish the signal from background noise. The polarization of the light is controlled through a half-wave plate before the sample. A 40X objective is responsible to couple the light into $2\mu m$ waveguides and a 20X objective collect the transmitted light from the other side. The sample sat on a Peltier cooler while a slow stream of water is passed through its stage to keep the TE cooler maintaining a constant temperature (Figure 5. 2).

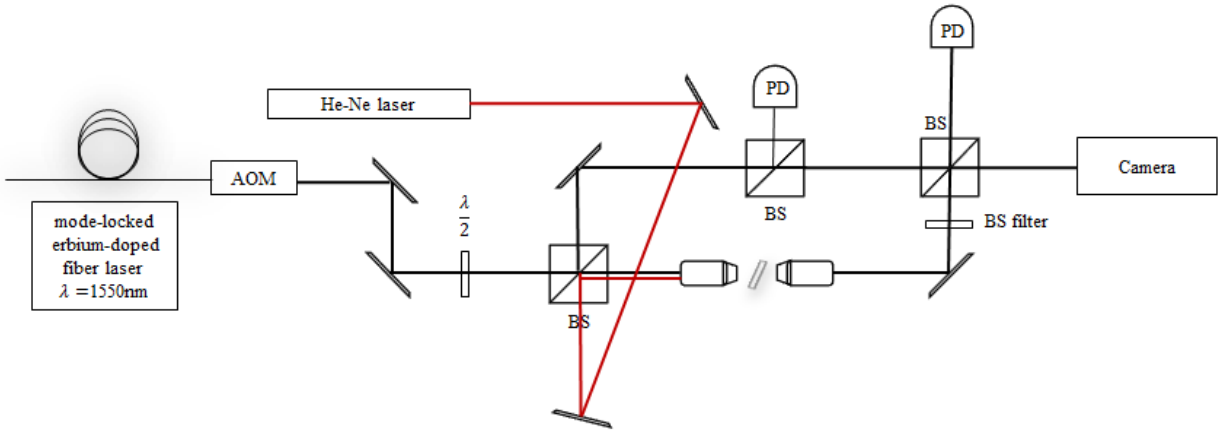

Figure 5. 1. Schematic view of the setup designed to measure the coupler/circulator devices

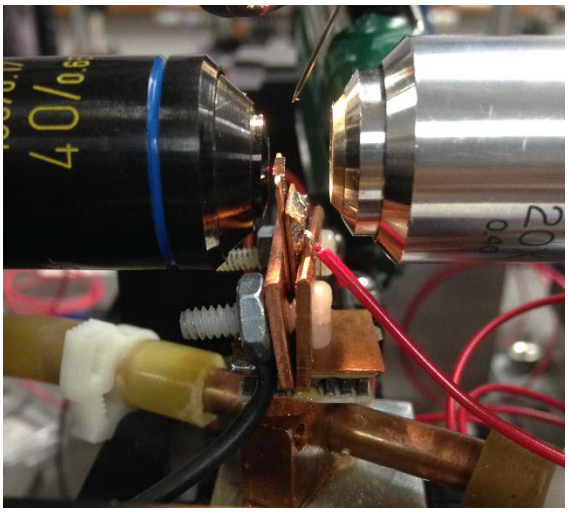

Figure 5. 2. The TE cooler stage holding the sample.

To pass the current through the sample we have employed a needle, connected to the Lightwave current source model LDX-3525, to locate each SOA fabricated in our device individually. The ground is connected through the stage holder back to the current source. A bandpass filter is added in the collecting branch to remove any possible ASE (amplified spontaneous emission), and eventually a THORLABS InGaAs amplified photodetector is responsible for intensity measurements of the switching occur in devices. The setup is occasionally modified as described briefly in previous sections, to be compatible with several measurements regarding the characterization experiments.

5.2. Directional coupler measurements and characterization

As mentioned in the previous sections, a solely directional coupler segment has been designed, fabricated and characterized, intending to direct for a better design of the circulator device. For this purpose, directional couplers with different lengths, from 1400nm to 750nm, has been fabricated on a single device while the ridge waveguide widths has been changed from $2-3\mu m$,

with the spacing differs from $2-3\mu m$. As the wet etch procedure brings us narrower structure in respect to the mask, a design with $3\mu m$ width and $2\mu m$ spacing was finally selected as the best pattern to be studied and fabricated. Utilizing the setup reported in the previous section, in the first set of experiments we have measured the best coupling length in a passive device by measuring the output ratio from port 3 to port 4 while the input light is couple in either port 1 or port 2 (figure 5. 3). Figure 5. 4, shows a plot this ratio in respect to different coupler lengths. From this measurement, we figured the best coupling length should occur close to $950\mu m$.

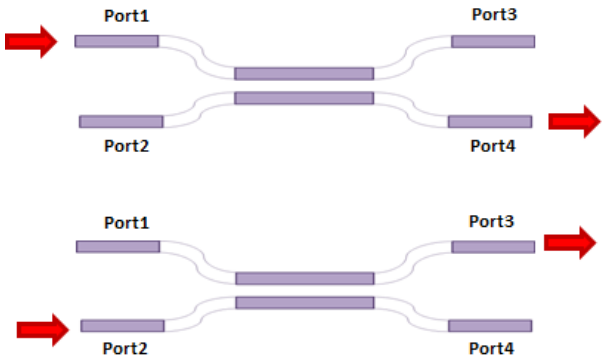

Figure 5. 3. Definition of different ports in our directional coupler device.

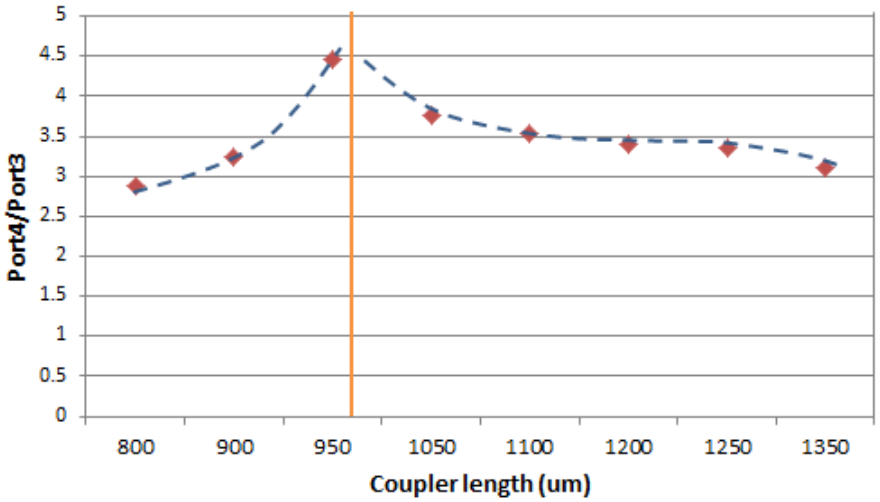

Figure 5. 4. The coupling ratio in a directional coupler in respect to the coupler length

Finding the best coupling length for a complete switching in the presence of low optical power, we have to validate the device performance under the high optical power influence in nonlinear regime. One should keep in mind that the high optical power is provided utilizing an SOA fabricated on the device. In this case an optical ASE is inevitable due to the high current requirements, which has to be monitored and distinguished from the pump signal. For this purpose we have designed four set of experiments to fully understand the ASE behavior and following the signal passage through the directional coupler. In the first set of these experiments, by blocking the input light, we only trigger the ASE by increasing the applied current on SOA from 0-150mA. As it is shown in figure 5. 5, in the absence of the signal the ASE intend to stay in the upper channel as the output is screened on port 3. This is reasonably expected as the ASE is known and measured to have broadband spectrum while the coupler is designed for a only selective frequency switching.

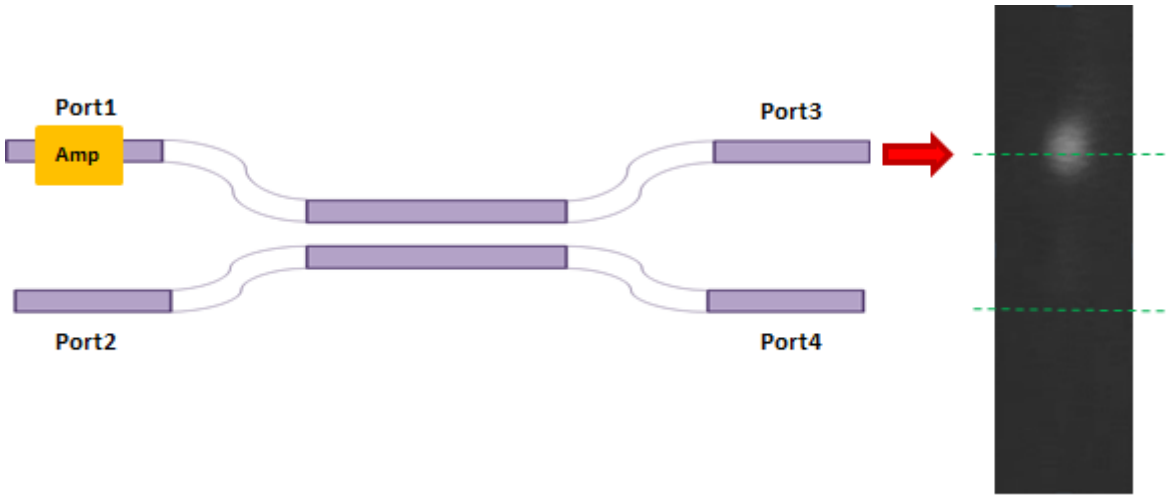

Figure 5. 5. ASE triggered from port 1, passage through a directional coupler device.

In the next set of experiments, directionality of the coupler in the presence of high optical power has been tested where the input light has been coupled through port one, and its transition through the device has been monitored when the amplifier on port 1 is turned on and off. Figure 5. 5. a, shows the output as captured by the camera, where the amplifier is off while figure 5. 5. b, indicate the case where a maximum current of 150mA has been passed through the amplifier. A complete switching in the output facet is obvious in this results. Notice that in the presence of input light, despite figure 5. 5. where only ASE existed, alignment fringes appears on the camera which is eventually removed from intensity measurements utilizing a slit.

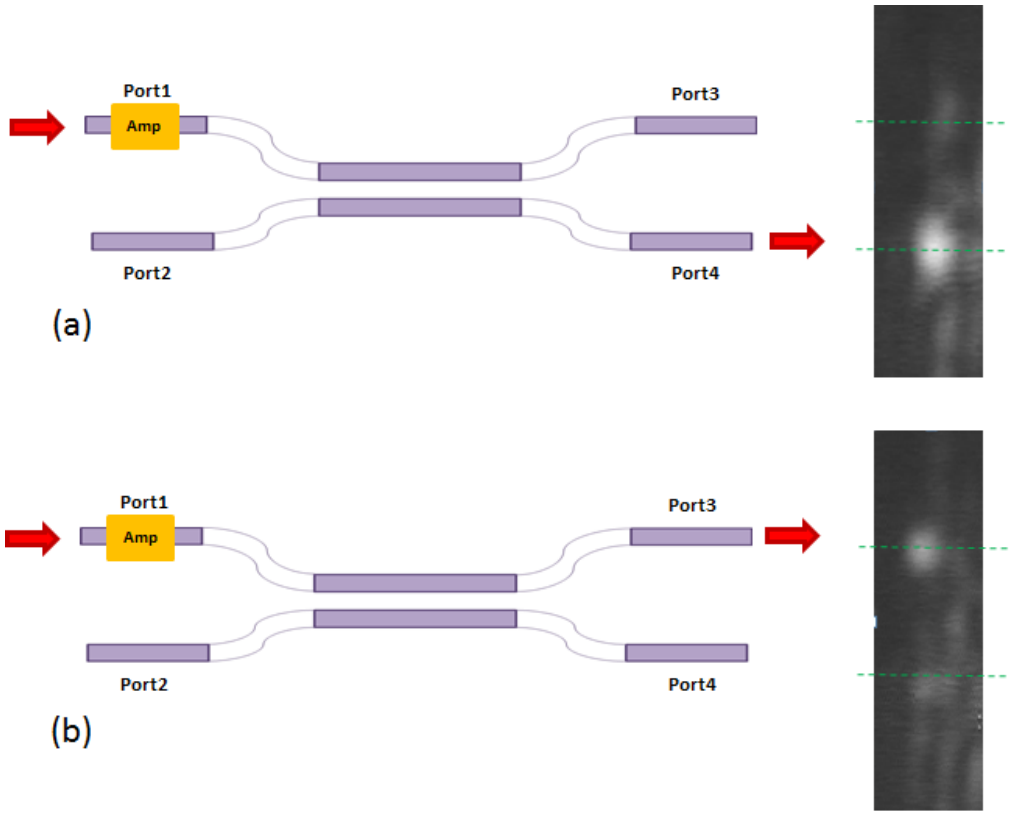

Figure 5. 6. a) Directional coupler functionality when a low power light is launched through port 1. b) when the light in channel 1 is amplified before reaching the coupler section.

To distinguish the possible ASE in port 3 for the case presented in figure 5. 6. a, from the original signal, each output has been collected individually and send to an optical spectrum analyzer. The peak power of the signal exiting port 4 then has been monitored during the switching. A 60 times drop in the output power has been recorded due to the switching which indicate a healthy degree of isolation for our directional couplers.

In the final version of the device, the amplifier in port 1 is supposed to work in its full functionality all the time, directing the input light from port 1 toward port 3, while any incoming light in port 3 is supposed to be directed to port2. One question that should be discussed in this design is then, can the presence of a high power ASE in such a system, trigger the nonlinearity in a way that even the low power light remain in its original input port branch. To investigate this hypothesis, we have designed an experiment presented in figure 5. 7, where the light is coupled from one side through one port, while the SOA on the other side is turned on. As it is shown in this figure, by increasing the current on the SOA on port 4, no nonlinear switching has been observed for the input light launched through port1. Port 3 in this experiment has been monitored by coupling through an optical spectrum analyzer and as the result no abrupt change in the signal power has been detected. Only a power change can be observed in port 4 due to the excessive amount of ASE from the SOA which can be eventually filtered out in the final experiment by utilizing a bandpass filter.

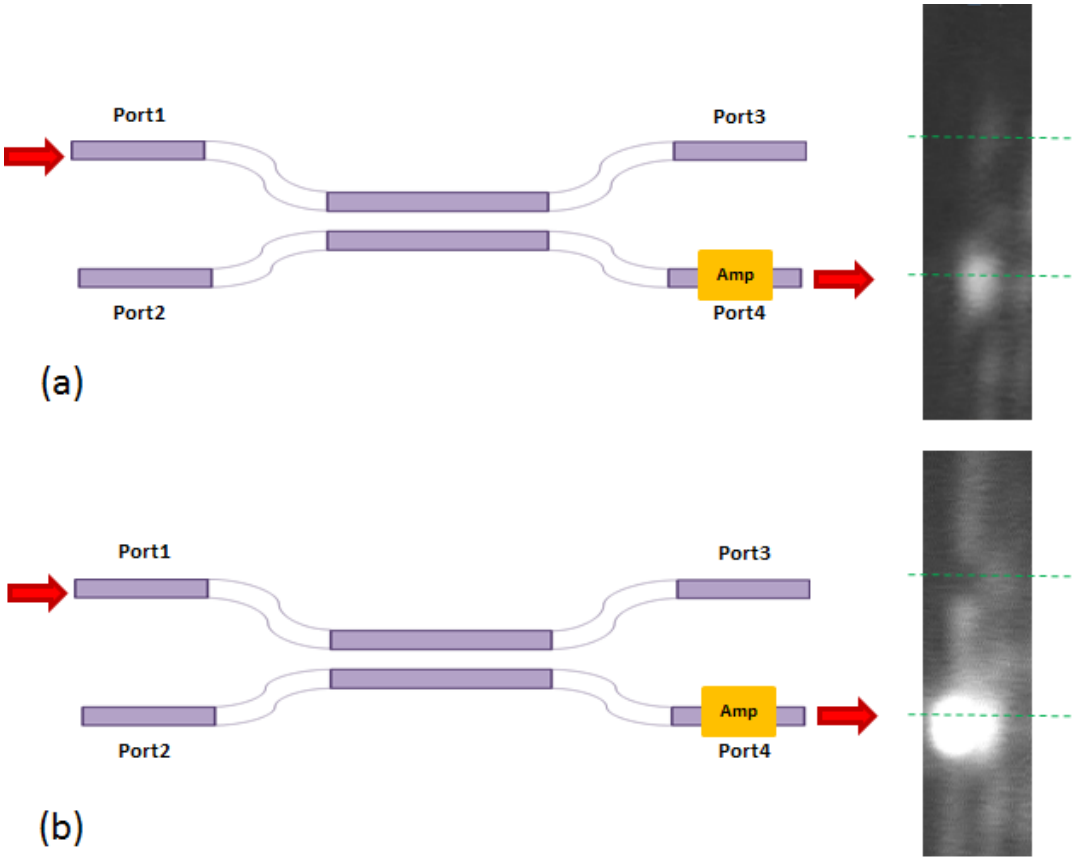

Figure 5. 7. a) coupling of light launched through port 1, to port 4 where no SOA is on. b) Coupling of light from port 1 to port 4 in the presence of SOA turned on in port 4.

5.3. Unidirectional 4 × 4 circulator measurements and characterization

As discussed in chapter 2, the 4-port circulator is designed based on the unidirectional couplers. The resulting counter-clockwise unidirectional optical transport (1→2→3→4→1) was accomplished by exploiting the interplay between successive amplification/attenuation stages and coupling elements displaying large resonance nonlinearities associated with InGaAsP quantum wells. To obtain the counter-clockwise transportation between adjacent ports, total internal reflection (TIR) mirrors has been employed in the center of the structure to guide optical

pulses along the circulated path. The performance of these TIR mirrors has been tested by FDTD methods in full-wave package of RSoft which has been explained in detail in chapter 2. However, the actual experimental losses in this section can be critical in the final performance of the circulator. To characterize this losses we have fabricated a waveguide with two mirrors along with a single waveguide as it is shown in figure 5.8 (a) and (b).

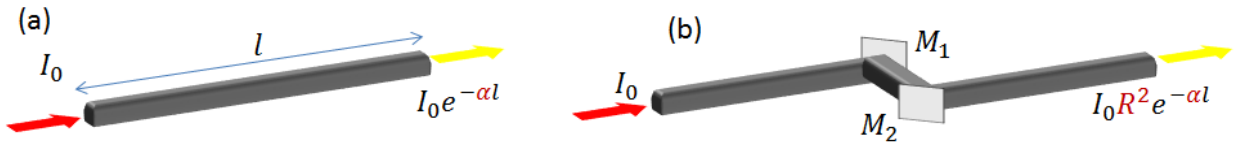

Figure 5.8. a) Schematic view of a single waveguide compare to (b) a waveguide with two mirrors.

Following the same techniques described in chapter 4.2, we have measured the losses in each structure of figure 5.8. Figure 5.9 shows the loss measurement of a single waveguide derived directly from its Fabry-Perot fringes. The value of this loss is much smaller than the previous measurements as a result of employing dry etch techniques for fabrication.

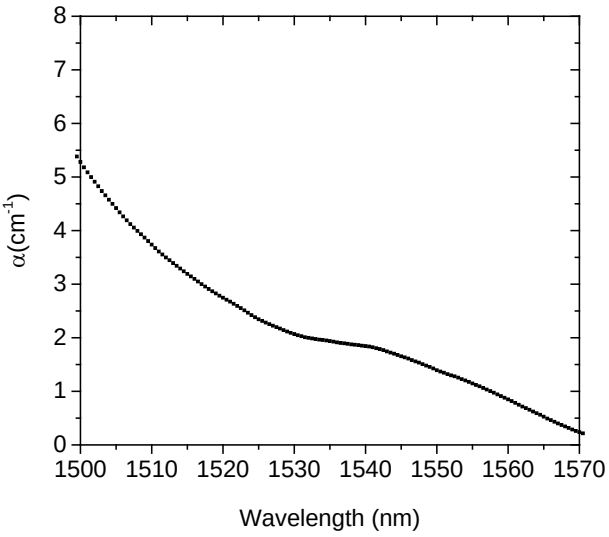

Figure 5.9. Loss measurements of a single waveguide through the Fabry-Perot fringes.

Based on similar principles, we have also measured losses in the structure with mirrors. Figure 5.10 shows loss measurement of the two structure. Comparing the outputs, we have extrapolated the reflectivity of each mirrors which is about 94%.

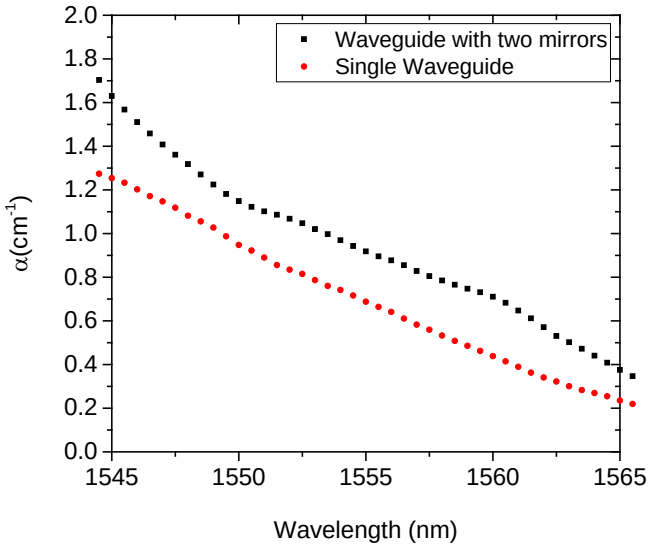

Figure 5.10. Loss measurements of a single waveguide compares with a waveguide with two mirrors.

Measuring a healthy reflectivity on the mirror sections, we followed with the device measurements. Although the system is nonlinear, for our circulator we have defined a linear scattering matrix (S) to characterize the output of each port in the presence of excitation at one channel ($P_{out} = P_{in}S$). The scattering matrix S is defined as

$$S = \begin{pmatrix} c_{11} & c_{12} & c_{13} & c_{14} \\ c_{21} & c_{22} & c_{23} & c_{24} \\ c_{31} & c_{32} & c_{33} & c_{34} \\ c_{41} & c_{42} & c_{43} & c_{44} \end{pmatrix}. \quad (5.\ 1)$$

Where component c_{ij} indicate the output at port *j*, when port *i* is excited. Due to the symmetry in the system and direction of propagation, most of the components in scattering matrix would be

zero. The main remaining element to be measured is port to port transition, where channel *i* is excited and channel *j* is the following anticlockwise rotated port in the structure to be measured. Because of the symmetrical design in our circulator, $c_{12} = c_{23} = c_{34} = c_{41}$. We define the port to port transition matrix element by c_f where *f* stands for the forward beam propagation. On the other side, any leak to the unwanted channel (i.e. when one is excited, four is marked as the unwanted) should be characterized. For this case we define c_b where *b* stands for backward propagation and indicate the leak in the system. The final form of the scattering matrix in this case is then represented as

$$S = \begin{pmatrix} 0 & c_f & 0 & c_b \\ c_b & 0 & c_f & 0 \\ 0 & c_b & 0 & c_f \\ c_f & 0 & c_b & 0 \end{pmatrix} \tag{5.2}$$

For characterization of the c_f, as shown in figure 5.11 (a), we have excited channel one and collect the output from channel two. For low optical power at the input, with finely choosing the best coupling length over the coupler devices, most of the light will couple to the adjacent waveguide in port one and guided toward port four as the consequence. However, by increasing the power, or in this case amplifying the signal by injecting the current through the gain medium, the detuning triggered by nonlinear response will guide the pulse toward port two. Figure 5.11 shows the normalized mode distribution in channel two monitored by an IR camera while the injected current on channel one is increased from zero to 200mA. We have also monitored port four, when channel one was excited for different injected currents. This time, the output will decrease by increasing the current as it is expected (figure 5.12).

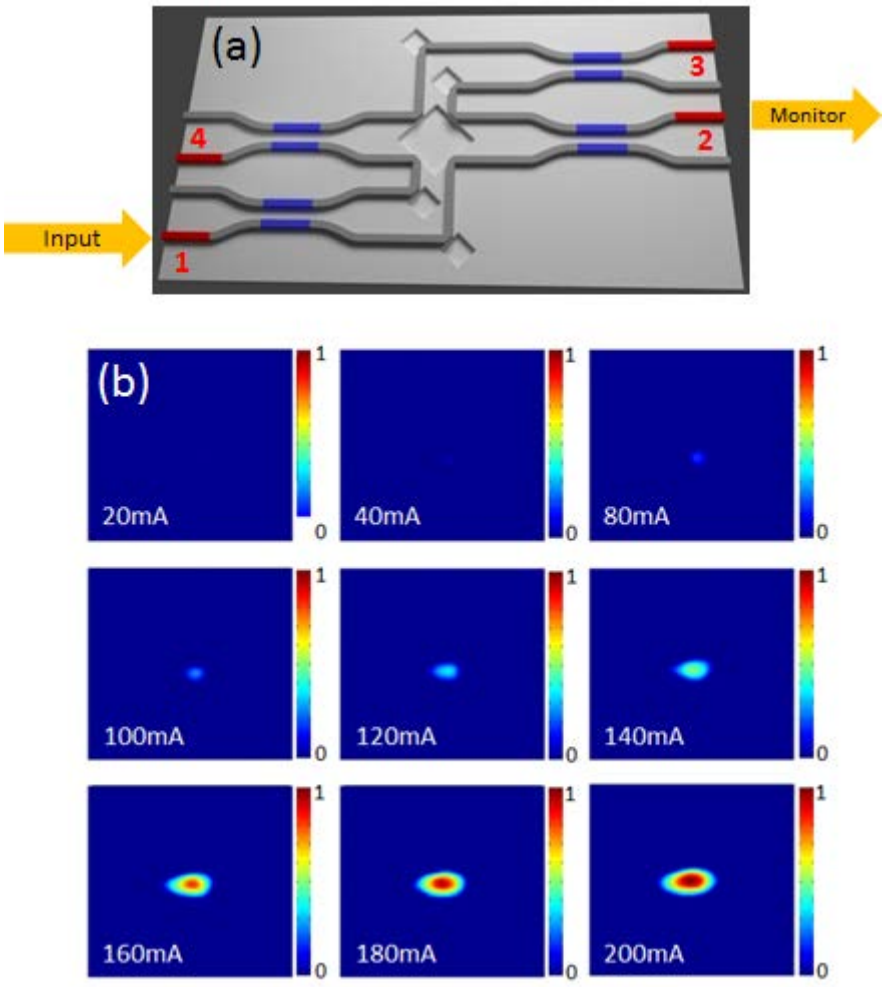

Figure 5.11. (a) Schematic view of the four port circulator for port to port measurements. (b) Output at channel two, while the injected current on channel one is increased from 0-200mA.

The best performance of the device is in a state where $c_f \gg c_b$. Therefore, we define the isolation degree in terms of $\beta = 10\,log\frac{P_{circulated}}{P_{leak}}$. To calculate this ratio, we have plotted the normalized output intensity of channel two and channel four on the same graph when the injected current on the excite port one is increased from $0 - 200mA$ (Figure 5.13).

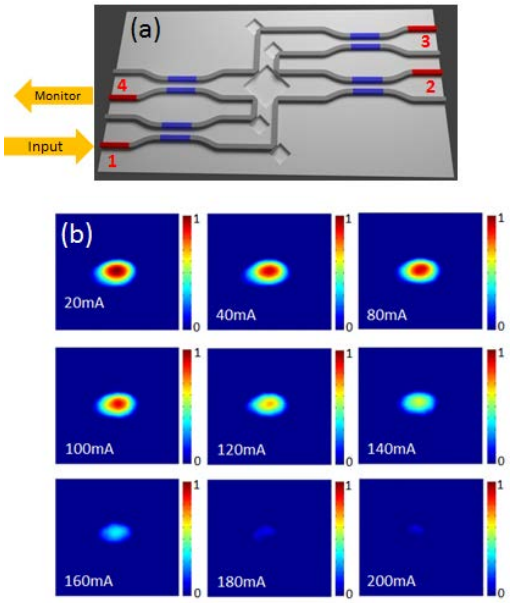

Figure 5.12. (a) Schematic view of the four port circulator for leak measurements. (b) Output at channel two, while the injected current on channel one is increased from 0-200mA.

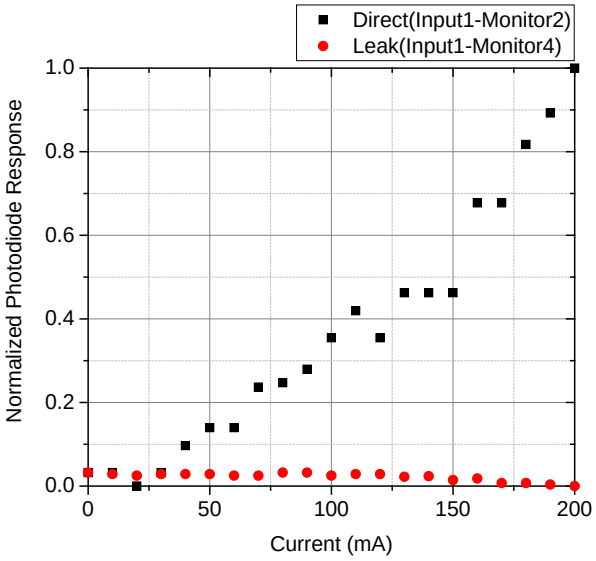

Figure 5.13. The normalized intensity of the output light from (black) channel two, and (red) channel four, when port one is excited, in respect to the injected current on port one.

The isolation degree, when all three SOA's on channel one, two and four are active, is reported at 21.3dB.

Finally we have to characterize the device spectral response. For this purpose, we have measured the isolation degree for different wavelengths achievable with our hand-made mode-lock laser. Figure 5.14 shows the results of this measurement. As one can see from this figure, the device has been designed to perform with the highest isolation degree at $1.5\mu m$. This is partially due to the design on directional coupler section. Figure 5.15 shows the isolation degree of a directional coupler in respect to wavelength. As it is shown in this figure, the isolation degree of a directional coupler is wavelength dependent and it has its maximum value for $1.5\mu m$.

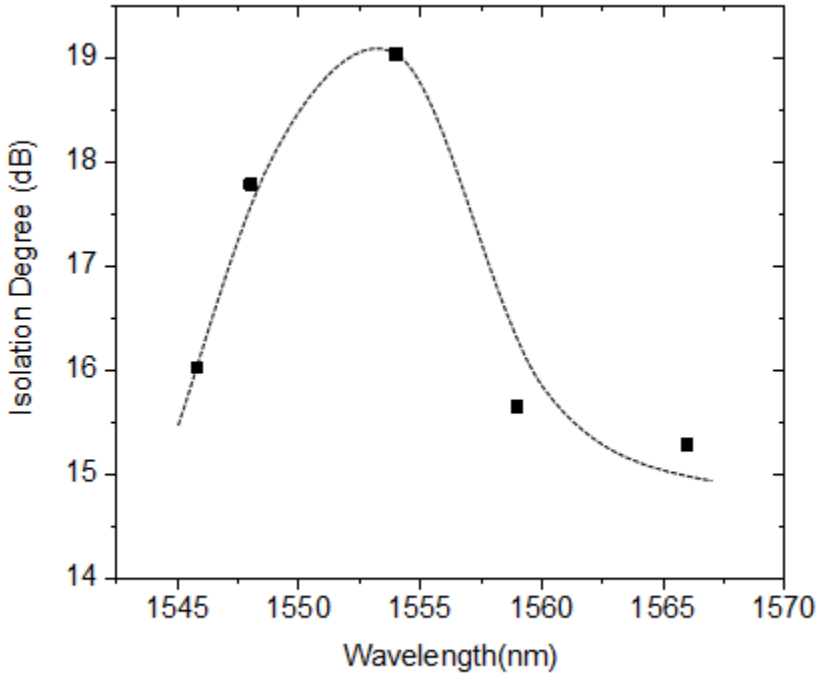

Figure 5.14. Isolation degree of circulator device in respect to the wavelength.

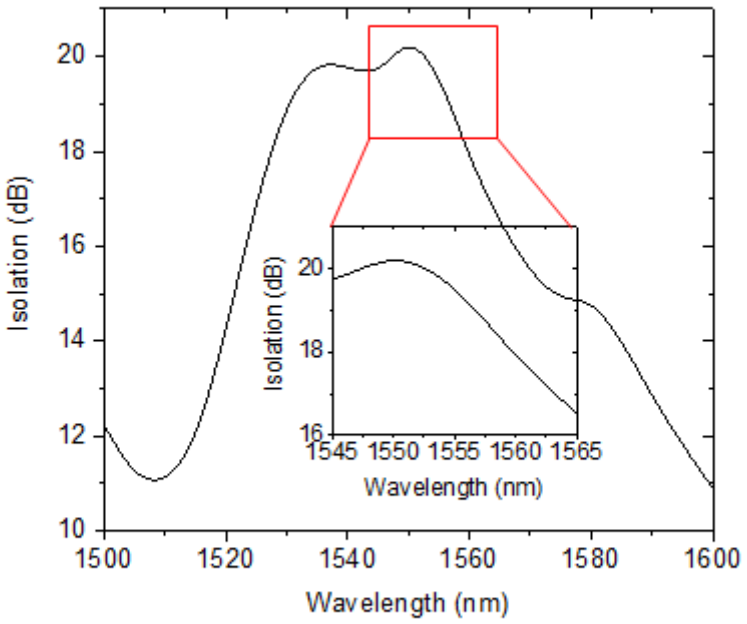

Figure 5.15. Isolation ratio of an isolator (directional coupler) device in respect to the wavelength. The inset shows the zoom-in figure for 1545-1565nm.

Another crucial element that can influence the isolation degree is the laser response in respect to the laser. As out laser source is an Erbium-doped handmade mode lock laser, the output optical power by itself is not uniform along different wavelengths. Figure 5.16 characterize the response of our laser. And finally one should recall that the SOA's gain spectrum can effect device performance and consequently the isolation degree. Considering all the elements, as it is shown in figure 5.14, the ultimate isolation only drop to the twenty percent of its maximum value over 20nm range.

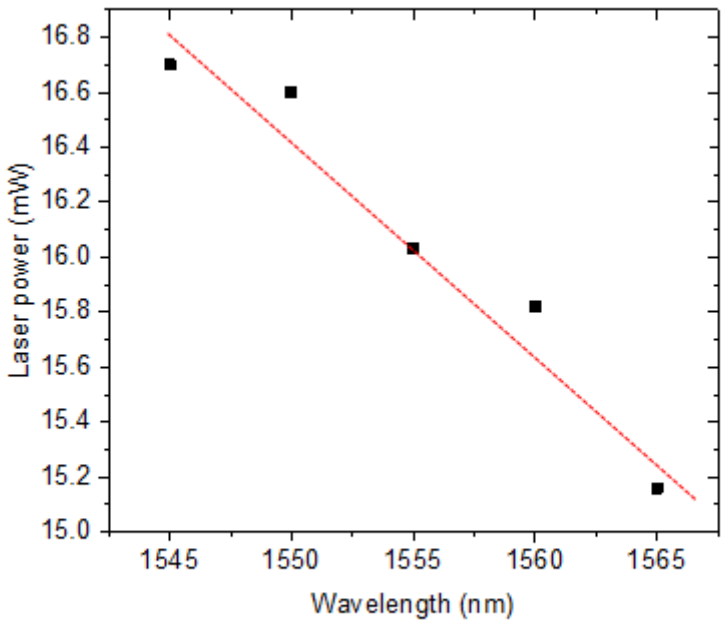

Figure 5.16. Erbium-doped laser response in respect to the wavelength.

CHAPTER 6: FULLY VECTORIAL ACCELERATING DIFFRACTION-FREE HELMHOLTZ BEAMS

6.1. Theoretical analysis of dynamical evolution of Bessel wave-packets in 2D

We begin our analysis by considering the Helmholtz equation in two dimensions $(\boldsymbol{\nabla^2} + \boldsymbol{k^2})\{\vec{\boldsymbol{E}}, \vec{\boldsymbol{H}}\} = \boldsymbol{0}$, where $\boldsymbol{k} = \boldsymbol{\omega n/c}$ represents the wave number. Without any loss of generality we here assume a transverse-electric mode, i.e., $\vec{\boldsymbol{E}} = \boldsymbol{E_y}(\boldsymbol{x}, \boldsymbol{z})\hat{\boldsymbol{y}}$. When this problem is treated in cylindrical coordinates, the following circulating mode can be directly obtained in terms of Bessel functions:

$$\vec{E} = J_\nu(kr)e^{i\nu\phi}\hat{y} \qquad (6.1)$$

where $\boldsymbol{r} = \sqrt{\boldsymbol{x^2 + y^2}}$ and $\boldsymbol{\phi} = \boldsymbol{\tan^{-1}(z/x)}$. Using the Fourier transform to decompose the Helmholtz equation in plane waves we get the familiar diffraction integral in the form

$$E_y(x,z) = \frac{1}{2\pi}\int_{-\infty}^{\infty} d\omega\, F(\omega)e^{i\omega x}e^{iz\sqrt{k^2-\omega^2}}, \qquad (6.2)$$

where z is the propagation direction and $F(\omega)$ represents the Fourier transform of the electric field at $z = 0$. For a Bessel function of the form $J_\nu(kx)$, where ν stands for the order of the Bessel function, $F(\omega)$ has a closed analytical form,[90]

$$F_c(\omega) = (k^2 - \omega^2)^{-\frac{1}{2}}\cos\left\{\nu \sin^{-1}\left(\frac{\omega}{k}\right)\right\}, \quad ,\omega < k \qquad (6.3\_a)$$

$$F_c(\omega) = -k^\nu sin\left(\frac{\nu\pi}{2}\right)(\omega^2 - k^2)^{-\frac{1}{2}}\left\{\omega + (\omega^2 - k^2)^{\frac{1}{2}}\right\}^{-\nu} \quad ,\omega > k \qquad (6.3\_b)$$

$$F_s(\omega) = (k^2 - \omega^2)^{-\frac{1}{2}}\sin\left\{\nu \sin^{-1}\left(\frac{\omega}{k}\right)\right\}, \quad ,\omega < k \qquad (6.3\_c)$$

$$F_s(\omega) = k^{\nu} cos\left(\frac{\nu\pi}{2}\right)(\omega^2 - k^2)^{-\frac{1}{2}}\left\{\omega + (\omega^2 - k^2)^{\frac{1}{2}}\right\}^{-\nu} . \omega > k \qquad (6.3\_d)$$

where $F_c(\omega) = \int_0^{\infty} J_{\nu}(kx)\, cos(\omega x)\, dx$ and $F_s(\omega) = \int_0^{\infty} J_{\nu}(kx)\, sin(\omega x)\, dx$. Note that the symmetry properties of a Bessel function eliminate the evanescent contributions from Eq. 6.3 for $\omega > k$ to the propagation integral in Eq. 6.2. Therefore to investigate the role of this component we study the dynamical evolution of a half-branch Bessel wave-packet-an arrangement very typical in experiments where the initial symmetries are broken using a Heaviside step function ($H(x)$). i.e. $E_y(x, 0) = H(x)J_{\nu}(kx)$. Writing the Fourier transform in Eq. 6.2 , in terms of sine (odd) and cosine (even) parts i.e. $F(\omega) = e(\omega) - io(\omega)$, and by rewriting the oscillating exponential as $e^{i\omega x} = \cos(\omega x) + isin(\omega x)$, then after removing the odd terms the integral in Equation 6.2 assumes the form

$$E_y(x, z) = \frac{1}{2\pi}\int_{-\infty}^{\infty} d\omega\, [e(\omega)\, cos(\omega) + o(\omega)sin(\omega x)]e^{iz\sqrt{k^2-\omega^2}}, \qquad (6.4)$$

Due to the symmetry properties of Eq. 6.3, it is more convenient to study the even and odd orders of a Bessel function individually. Starting from an even-order Bessel function, where $\nu = 2m$, it is clear from Eq.6.3 that for the limit $\omega > k$ the even part of the Fourier transform is proportional to $\sin(m\pi)$ and consequently cancels. Therefore the only contribution to the evanescent field comes from the second term in the integral of Eq. 6.4. Substituting Eq. 6.3 (d) in eq. 6.4 and by using the change of variable as $\omega = kcosh\theta$ the integral for the evanescent part gets the form

$$E_y(x, z) = \frac{(-1)^m}{\pi} Im\left[\int_0^{\infty} d\theta\, e^{ikxcosh\theta} e^{-zksinh\theta} e^{-2m\theta}\right]. \qquad (\omega > k) \qquad (6.5)$$

The dominant contribution to the integral comes mainly from the region around $\theta \approx 0$, since the integrant oscillate very fast outside the mentioned range and would cancel out. In this case, it

would be valid to use the approximations $sinh\theta \sim \theta$ and $cosh\theta \sim 1 + \theta^2/2$. Given these limits, one is able to obtain a closed analytical form for the integral in equation 6.5:

$$E_y(x,z) = \frac{(-1)^{\mathrm{m}}}{\pi} Im\left[e^{ikx}\sqrt{\frac{i\pi}{2kx}}\, e^{\frac{i}{2kx}(zk+2m)^2}\left(1-\mathrm{erf}\left(\frac{zk+2m}{\sqrt{-2ikx}}\right)\right)\right], \quad (\omega > k) \qquad (6.6)$$

To evaluate the propagation integral in the region $|\omega| < k$, for the case of an even Bessel function, i.e., $\nu = 2m$ one should consider both the sine and cosine contributions in the Fourier transform separately. Substituting Eq. 6.3_a in Eq. 6.2 and using the change of variable as $\omega = ksin\theta$ the integral for the cosine part assumes the form

$$E_y(x,z) = \frac{1}{2\pi}\int_{-\frac{\pi}{2}}^{\frac{\pi}{2}} d\theta \cos\{2m\theta\}\, e^{ikxsin\theta} e^{izkcos\theta}. \qquad (6.7)$$

For convenience we define a new variable as $\phi = \sin^{-1} z/r$, so the integral in Eq. 6.7 changes to

$$E_y(x,z) = \frac{1}{2\pi}\int_{-\frac{\pi}{2}}^{\frac{\pi}{2}} d\theta \cos\{2m\theta\}\, e^{ikrsin(\theta+\phi)}. \qquad (6.8)$$

By expanding the exponential component in terms of Bessel functions and by using the relation, $e^{ixsin\theta} = \sum_{n=-\infty}^{\infty} e^{in\theta} J_n(z)$,[91] and changing the order of integration with the summation, one can get an exact closed form solution to the integral in Eq. 6.8:

$$E_y^c(x,z) = \frac{1}{2} cos2m\phi\, J_{2m}(kr)$$

$$+\frac{i}{\pi}(-1)^m \sum_{n=0}^{\infty} (-1)^n J_{2n+1}(kr)\sin[(2n+1)\phi]\frac{4n+2}{(2n+1)^2-4m^2}. \qquad (6.9)$$

Here the index c represent the cosine contribution to the field. One can follow the same procedure in order to obtain a similar solution for the sine contribution, $E_s(x,z)$

$$E_y^s(x,z) = \frac{-1}{2} sin2m\phi\, J_{2m}(kr)$$

$$+\frac{i}{\pi}(-1)^m \sum_{n=0}^{\infty}(-1)^n J_{2n+1}(kr)\cos[(2n+1)\phi]\frac{4m}{(2n+1)^2-4m^2}. \quad (6.10)$$

Combining the two solutions in Eqs .6.9 and 6.10 with the evanescent contribution from Eq. 6.6, the propagation dynamics of a half even Bessel function of the order $\nu = 2m$ can be described in the form

$$E_y(x,z) = \frac{1}{2}J_{2m}(kr)e^{2im\phi}$$

$$+\frac{i}{\pi}(-1)^m \sum_{n=0}^{\infty}(-1)^n J_{2n+1}(kr)[\sin(2n+1)\phi\frac{4n+2}{(2n+1)^2-4m^2}$$

$$-i\cos(2n+1)\phi\frac{4m}{(2n+1)^2-4m^2}]$$

$$+\frac{(-1)^{\mathrm{m}}}{\pi} Im\left[e^{ikx}\sqrt{\frac{i\pi}{2kx}}e^{\frac{i}{2kx}(zk+2m)^2}\left(1-\mathrm{erf}\left(\frac{zk+2m}{\sqrt{-2ikx}}\right)\right)\right]. \quad (6.11)$$

A similar analytical result can be obtained for the propagation of an odd-order Bessel function when $E_y(x,0) = H(x)J_{2m+1}(kx)$. In this case the odd part of Fourier transform is proportional to $sin(m\pi)$ for the range $(\omega > k)$ and therefore the only contribution from evanescent fields comes from the even component. Substituting Eq. 6.3_b in the integral of equation 6.2 one should get a similar result to the even-order Bessel for the evanescent field contribution to the propagation:

$$E_y(x,z) = \frac{(-1)^{m+1}}{\pi} Re\left[e^{ikx}\sqrt{\frac{i\pi}{2kx}}e^{\frac{i}{2kx}(zk+2m+1)^2}\left(1-\mathrm{erf}\left(\frac{zk+2m+1}{\sqrt{-2ikx}}\right)\right)\right]$$

$$(\omega > k) \qquad (6.12)$$

Evidently, analytical solutions for the region $|\omega| < k$ can be evaluated for the odd-order Bessel propagation in the form

$$E_y(x,z) = \frac{1}{2}J_{2m+1}(kr)e^{i(2m+1)\phi}$$

$$+\frac{(-1)^m}{\pi}\sum_{n=1}^{\infty}(-1)^n J_{2n}(kr)\,[cos2n\phi\,\frac{4\mathrm{m}+2}{(2m+1)^2-4n^2}$$

$$+\mathrm{isin}\,2n\phi\,\frac{4n}{(2m+1)^2-4n^2}]\,. \qquad (-k<\omega<k) \quad (6.13)$$

Figures 6.1 (a, b) show the two-dimensional intensity patterns for such accelerating half even-Bessel wave packets, based on the analytical solutions of equations 6.11, when $m = 5$ and $m = 25$ respectively. To check the validity of the approximations that have been used to derive the evanescent components, we have also plotted the normalized intensity profile at $z = 0$ obtained from analytical results in equations 6.11 and compare it with the initial Bessel functions in Fig 6.1 (c, d). This comparison shows an error less that 10^{-5} when $m = 5$ and a difference of 10^{-7} for $m = 25$. Note that this difference diminishes as the order of the Bessel functions increases. One can show that for higher orders the radius increases asymptotically

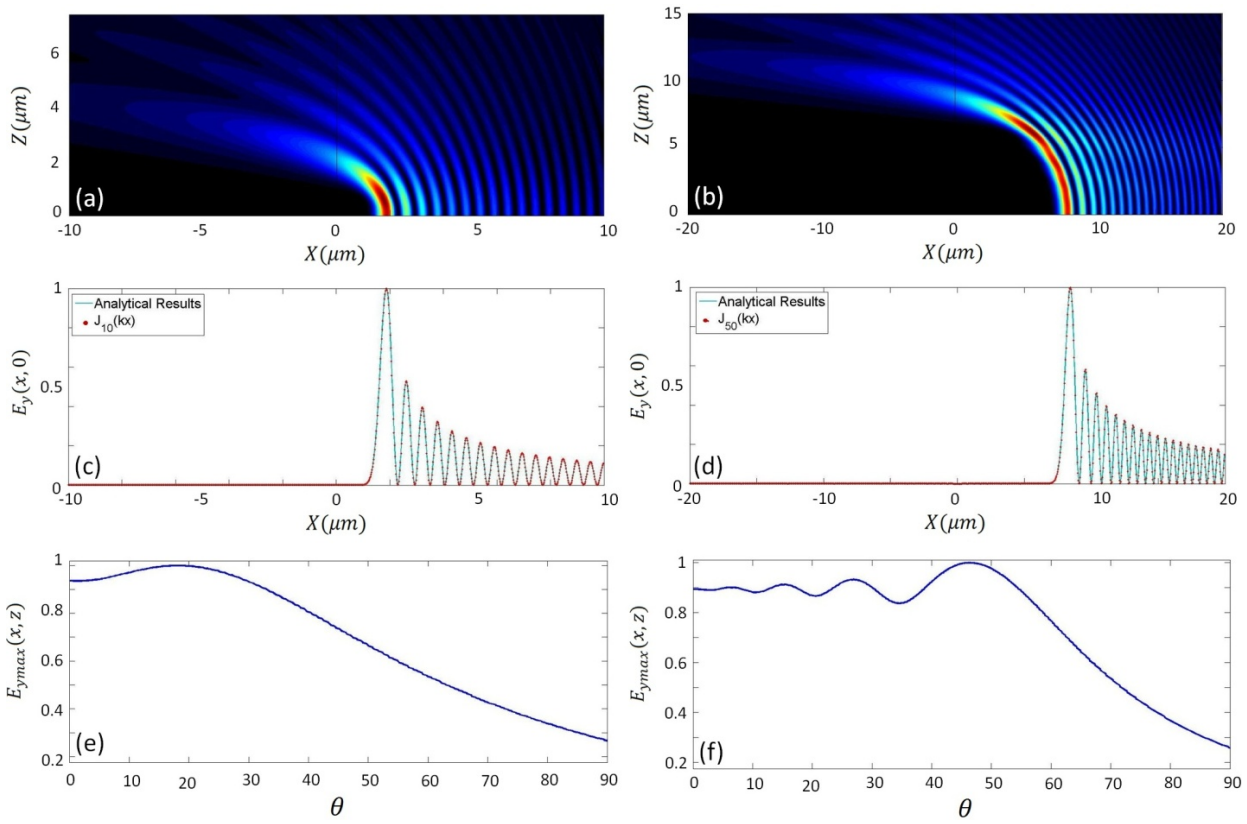

Figure. 6.1. (color online). Intensity profile resulting from the self-bending dynamics of an even-order Bessel beam (a) with 2m=10, and (b) 2m=50. (c, d) Corresponding normalized initials field at $z = 0$ (e, f) Normalized intensity change of the first lobe correspond to the patterns in (a, b) in respect to the angle of propagation up to 90^o.

According to the relation $r \sim \lambda/2\pi[\,\nu + 0.808\nu^{\frac{1}{3}} + 0.072\nu^{-\frac{1}{3}}]$, where ν stands for the order of the Bessel function. As a result the beam-envelope will travel a longer path for higher Bessel orders and the evanescent part will disappear after a certain distance. This effect can be seen in Eqs 6.6 and 6.12, where the argument of the error function increases by raising the order of the Bessel wavepacket, i.e., ν. Moreover the width of the first lobe can be approximated asymptotically by $\Delta \sim \lambda/2\pi[\,2.094\nu^{\frac{1}{3}} + 1.921\nu^{-\frac{1}{3}}]$ for large orders. Figures 6.1 (e, f) show the intensity variation of the main lobe as a function of the angle of propagation for $2m = 10$ and $2m = 50$ respectively. As it is clear from these figures, the higher order Bessel beams tend to

experience more oscillations during propagation as the evanescent field contribution fades out faster.

6.2. Propagation dynamics of half branch apodized Bessel-Beams

As it was mentioned before, all the optical diffraction-free wavefronts possess an infinite norm which makes it necessary to apodize them in order to observe them experimentally. This apodization can affect the propagation pattern dramatically. To investigate these effects we have studied the propagation pattern of an apodized version of such accelerating Bessel beams. Here we choose the apodization to be $1/x$, ensuring that the wave-packet has finite energy. In this case by using the equation $J_\nu(kx)/x = \frac{1}{2\nu}[J_{\nu-1}(kx) + J_{\nu+1}(kx)]$ and by using the results of the previous section, the propagation dynamics of such apodized even order Bessel beams (i.e, $\nu = 2m$), can be expressed in a closed form as folows

$$
\begin{aligned}
E(x,z) = \frac{1}{8m}[J_{2m+1}(kr)\,\mathrm{e}^{i(2m+1)\phi} + J_{2m-1}(kr)\,\mathrm{e}^{i(2m-1)\phi}] \\
+ \frac{(-1)^m}{4m\pi}\sum_{n=1}^{\infty}(-1)^n J_{2n}(kr)\left\{cos2n\phi\left[\frac{4m+2}{(2m+1)^2-4n^2} + \frac{-4m+2}{(2m-1)^2-4n^2}\right]\right. \\
\left. + i\sin 2n\phi\left[\frac{4n}{(2m+1)^2-4n^2} + \frac{-4n}{(2m-1)^2-4n^2}\right]\right\} \\
+ \frac{(-1)^{\mathrm{m+1}}}{4m\pi} Re\left[e^{ikx}\sqrt{\frac{i\pi}{2kx}}\, e^{\frac{i}{2kx}(zk+2m+1)^2}\left(1-\mathrm{erf}\left(\frac{zk+2m+1}{\sqrt{-2ikx}}\right)\right)\right] \\
+ \frac{(-1)^{\mathrm{m}}}{4m\pi} Re\left[e^{ikx}\sqrt{\frac{i\pi}{2kx}}\, e^{\frac{i}{2kx}(zk+2m-1)^2}\left(1-\mathrm{erf}\left(\frac{zk+2m-1}{\sqrt{-2ikx}}\right)\right)\right] \qquad (6.14)
\end{aligned}
$$

Figure 6.2 shows the plots of analytical results as obtained from Eq. 6.14 for two different orders of $\nu = 10$ and $\nu = 50$. To check the validity of the approximations, again in this case we have plotted the initial Bessel distribution along with the analytical results at $z = 0$. As it is shown in figure 6. 2 (b, c) a good agreement has been achieved between the results in Eq. 6.14 and the initial distribution. Note that in this case the oscillations don't show up in the intensity of the main lobe. This happens because the apodization affects both the evanescent and propagating parts of this beam.

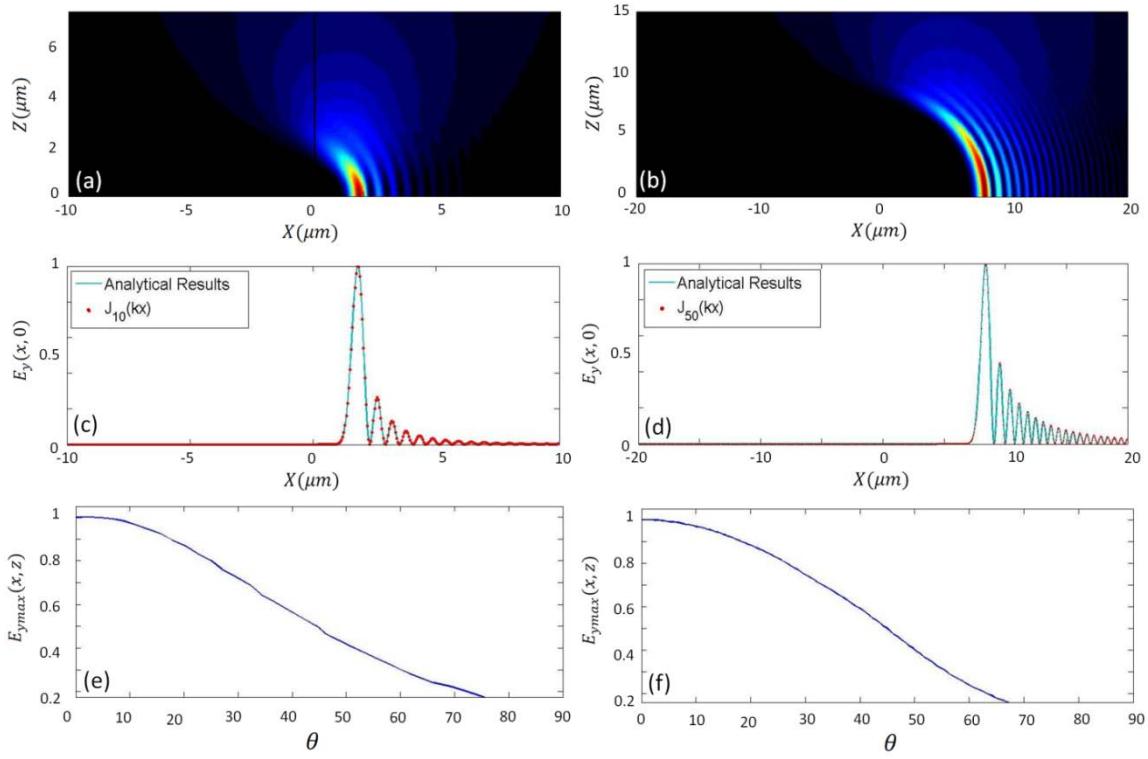

Figure. 6. 2. (color online). Intensity profile resulting from the self-bending dynamics of an even-order apodized Bessel beam (a) with 2m=10, and (b) 2m=50. (c, d) Corresponding normalized initials field at $z = 0$ (e, f) Normalized intensity change of the first lobe correspond to the patterns in (a, b) in respect to the angle of propagation up to 90^o.

6.3. Dynamical evolution of fully symmetrical accelerating Bessel beams

As it was mentioned before the whole Bessel accelerating wave-packets are evanescent free due to their symmetrical distribution. For this reason the dynamical evolution of such beams is entirely different from the half branch Bessel case. As an example for an even Bessel function in the initial distribution i.e., $E_y(x,0) = J_\nu(kx)$ where $\nu = 2m$ with m being an integer, the sine contributions to the Fourier transform cancels out due to the symmetries. Moreover, as it is clear in Eq. 6.3_b that the evanescent part for the case $\omega > k$ would be proportional to $\sin(m\pi)$ which is going to be zero all along propagation. Hence by substituting the only remaining term from Eq. 6.3_a, the integral in Eq. 6.2 with a change of variable as $\omega = ksin\,\theta$, gets the form

$$E_y(x,z) = \frac{1}{\pi}\int_{-\frac{\pi}{2}}^{\frac{\pi}{2}} d\theta \cos\{2m\theta\}\, e^{ikxsin\theta} e^{izkcos\theta}. \qquad (6.15)$$

To evaluate the integral in Eq. 6. 3.1 a similar approach to the one described before should be followed. However it is important to stress that this time only the cosine part of the Fourier transform contributes to the propagation. One can get an exact close form solution to the integral in Eq. 6. 15 as follows

$$E_y(x,z) = cos2m\phi\, J_{2m}(kr)$$

$$+\frac{2i}{\pi}(-1)^m \sum_{n=0}^{\infty}(-1)^n J_{2n+1}(kr)\sin[(2n+1)\phi]\frac{4n+2}{(2n+1)^2-4m^2}. \qquad (6.16)$$

Equation 6. 16 describes the acceleration pattern of an even-Bessel function in free space. The first term in this equation, ensures that the initial Bessel function would accompany the whole pattern during evolution. However the second term introduces variations in the initial distribution. A similar result can be obtained when, $\nu = 2m+1$, for an odd-order Bessel

function. Note that in this case the cosine part of the Fourier transform of the initial distribution would vanish due to the symmetries of odd-order Bessel function. Also, the evanescent field, given by Eq. 6.3_d is proportional to $\sin(m\pi)$ and is canceled out. Following the same technique described before, one can get a similar result to Eq. 6.16 for the propagation pattern of an odd-order Bessel function:

$$E_y(x,z) = \cos(2m+1)\,\phi\, J_{2m+1}(kr)$$

$$+\frac{2i}{\pi}(-1)^m \sum_{n=1}^{\infty}(-1)^n J_{2n}(kr)\sin[(2n)\phi]\frac{4n+2}{(2n+1)^2-4m^2}\,. \qquad (6.17)$$

Similarly in the case of odd-order Bessel function, the initial field configuration persists during the propagation and the disturbing terms only contribute to the pattern shortly after the origin. It would be easy to show from Eq. 6.16 and 6.17 that the analytical results would converge to the initial field distributions at $z = 0$ for each case. Figures 6.3 show two-dimensional plots correspond to the intensity profile of an even/odd order Bessel distribution described in eqs. 6.16 and 6.17, where $m = 25$.

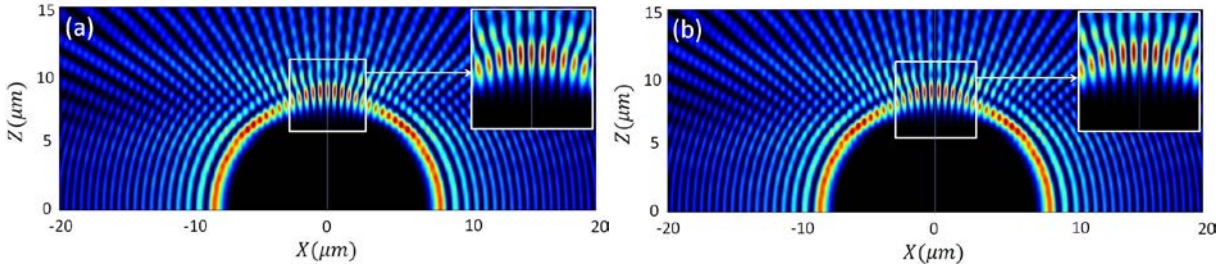

Figure. 6. 3. (color online). Intensity profile of an (a) even-order Bessel accelerating beam when 2m=50, and (b) odd-order Bessel propagation with 2m+1=51.

As it is clear from Fig. 6. 3, interference patterns occurs in both left and right branches, even for small distance of propagation. Note that this alternation would just affect the lobes, while the intensity profile of the semicircle remains unchanged and as a result the acceleration trajectory

stays circular. As Fig. 6. 3 shows, this interference pattern can lead to the focusing of two branches to give maximum on the z-axis for even order Bessel function whereas is zero for the odd case due to destructive interference.

6.4. Elliptical coordinates and Mathieu wave packets analysis

Given that Airy beams are unique within 1D paraxial optics, the question naturally arises if the aforementioned higher-order Bessel accelerating diffraction-free waves represent the only possible solution. In other words, are there any other vectorial solutions to the full-Maxwell equations that could in general accelerate along more involved trajectories? If so, can they be extended in the three-dimensional vectorial regime, and are they again self-healing in character?

In this section, we show that indeed other families of accelerating nondiffracting wave solutions to Maxwell's equations also exist. By utilizing the underlying symmetries of the corresponding Helmholtz problem, we demonstrate both theoretically and experimentally self-healing vectorial wave fronts—capable of following elliptic trajectories and hence experiencing a nonuniform acceleration. The existence of such beams clearly indicates that shape preservation is not an absolute must in attaining accelerating diffraction-free propagation. Our results may pave the way toward synthesizing more general classes of accelerating waves for applications in optics and ultrasonics.

We begin our analysis by first considering the Helmholtz equation in two dimensions $\left(\partial_{xx} + \partial_{yy} + k^2\right)\{\vec{E}, \vec{H}\} = 0$, that governs both the electric and magnetic field components of an optical wave. For the transverse-electric (TE) case, the electric field involves only one component, i.e.,

$\vec{E} = E_z(x,y)\hat{z}$ from where the magnetic vectors H_x , $H_y$can be readily deduced from Maxwell's equations for a given wave number $k = \omega n/c$. By introducing elliptic coordinates, the Helmholtz problem takes the form

$$\left[\frac{2}{f^2\left(\cosh 2u - \cos 2v\right)}\left(\frac{\partial^2}{\partial u^2}+\frac{\partial^2}{\partial v^2}\right)+k^2\right]E_z = 0 \qquad (6.17)$$

where $x = f\cosh u\cos v$, $y = f\sinh u\sin v$ with $u \in [0,\infty)$ and $v \in [0,2\pi)$. In this representation, f represents a semifocal distance and is associated with the ellipticity of the system. Equation 6.17 is in turn solved via standard separation of variables, e.g., $E_z = R(u)S(v)$ in which caseone obtains the following ordinary differential equations:

$$\left[\frac{d^2}{dv^2}+(a-2q\cos 2v)\right]S(v) = 0 \qquad (6.18-\text{a})$$

$$\left[\frac{d^2}{du^2}-(a-2q\cosh 2u)\right]R(u) = 0 \qquad (6.18-\text{b})$$

with the dimensionless quantity $q = f^2k^2/4$. On the other hand, the parameter 'a' in eqs. 6.18 can be obtained from a sequence of eigenvalues $a_m\,(m = 1,2...)$ corresponding to the Mathieu eq. 6. 4. 2 (a). From this point on, both the angular $S_m(v)$ and radial $R_m(u)$ Mathieu functions can be uniquely determined. A possible elliptic solution to these equations is expected to display a circulating power flow in the angular direction. This can be achieved through a linear superposition of the standard solutions to Eqs. 6.18 with constant real coefficients A and B,[53, 54, 91]

$$E_z^m(u,v;q) = Ace_m(v;q)Mc_m^{(1)}(u;q) + iBse_m(v;q)Ms_m^{(1)}(u;q), \qquad (6.19)$$

where ce_m and se_m represent even and odd angular Mathieu functions of order m while $Mc_m^{(1)}$ and $Ms_m^{(1)}$ stand for their corresponding radial counterparts (of the first kind). Figures 6. 4 (a) and (b) show a two-dimensional plot of these elliptic modes for two different values of q when $m = 8$ and $A = B = 1$. As one would expect, the ellipticity of the light trajectory increases with the semifocal parameter f. What is also clearly evident from these figures is the fact that the intensity of the rings does not remain constant in the angular domain. In other words, unlike other families of diffraction-free beams, these elliptical beams can propagate in an accelerating fashion up to 90 without exactly preserving their shape. Note that the power density, especially that of the first lobe, tends to increase along the major axis while it reaches its lowest value when it is passing the minor axis of the ellipse. Interestingly, this behavior persists even under dynamic conditions, i.e., when such a field configuration is launched on axis.

Given that all optical diffraction-free arrangements (including those mentioned here) possess, strictly speaking, an infinite norm, in practice they have to be apodized in order to be experimentally observed. Figure 6. 4 (c) depicts an elliptic trajectory when a weakly truncated (using a Gaussian apodization) version of the field profile in Eq. 6.19 is used at $v = 0$, e.g., when launched from the major axis. These simulations are carried out for $\lambda = 1\ \mu m$, $m = 150$, and $f = 31.8\ \mu m$ provided that the width of the first lobe is approximately $550\ nm$. In this case, the intensity $|E_z|^2$of the main lobe follows an ellipse, starting at $34\ \mu m$ and eventually reaching $12\ \mu m$, on the y axis. On the other hand, when this same beam is launched from the y axis [$v = \pi/2$, in Eq. 6.19] the main lobe meets the major axis at $34\mu m$ [Fig. 6.4 (d)]. Unlike the previously reported Bessel wave fronts propagating on circular trajectories,[50] these beams can exhibit diffraction-free behavior in spite of the fact that their intensity features are no longer

invariant during propagation because of their varying acceleration. Figure 6. 4 (d) also indicates that the intensity of the lobes tends to eventually increase before intersecting the x axis. Conversely, it decreases when reaching the y axis for the case shown in Fig. 6. 4 (c). Interestingly, this response is in agreement with the results of Figs. 6. 4 (a) and (b) when taken over the first quadrant.

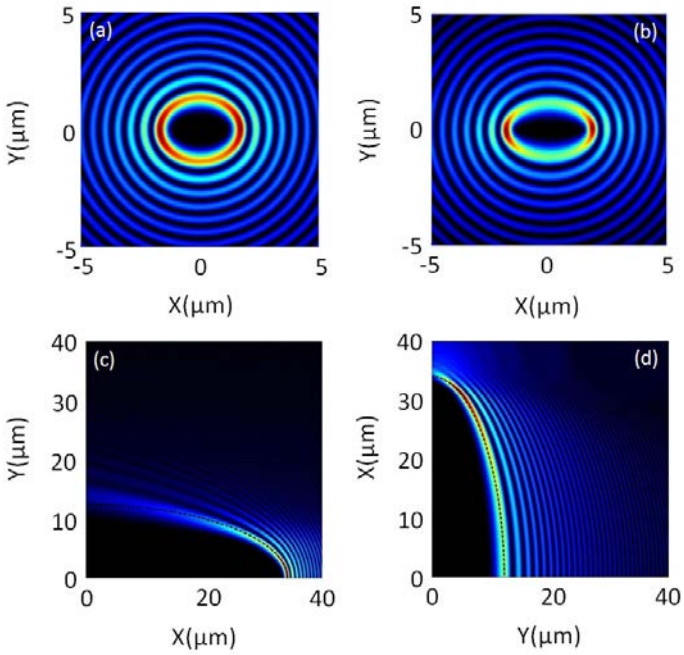

Figure. 6. 4. (Color online). Intensity profiles of elliptic modes of order m = 8 when (a) q=10 and (b) q=20. (c) Propagation pattern of a weakly truncated Mathieu beam when it islaunched from the major axis, when m = 150 and q = 10000, starting from x = 34μm and reaching y = 12μm on the minor axis. (d) Same Mathieu beam as in (c), launched from the minor axis, starting at y = 12μm and reaching x = 34μm. In (d), note the increase in intensity at the apogee point.

The variation of the intensity levels along these elliptic trajectories can be better understood from power conservation requirements. Given that in elliptic coordinates, a given lobe moves on a $u = const$ trajectory, then, as u increases (needed for establishing a broad wave front), the encompassing region becomes almost circular. As a result, this same power flow happens to be

constricted when crossing the major axis, hence elevating the intensity levels within the beam. Conversely, the intensity drops in the other regime [Fig. 6. 4 (c)]. To demonstrate that these beams remain actually diffraction-free, we next examine their self-healing properties. Figure 6. 5 (a) depicts the propagation dynamics of such a Mathieu wave front when its main lobe is initially obstructed [Fig. 6. 5 (b)]. The parameters used are the same as those of Fig. 6. 4 (c). The self-healing mechanism is here clearly evident after propagating a distance of 5 μm.

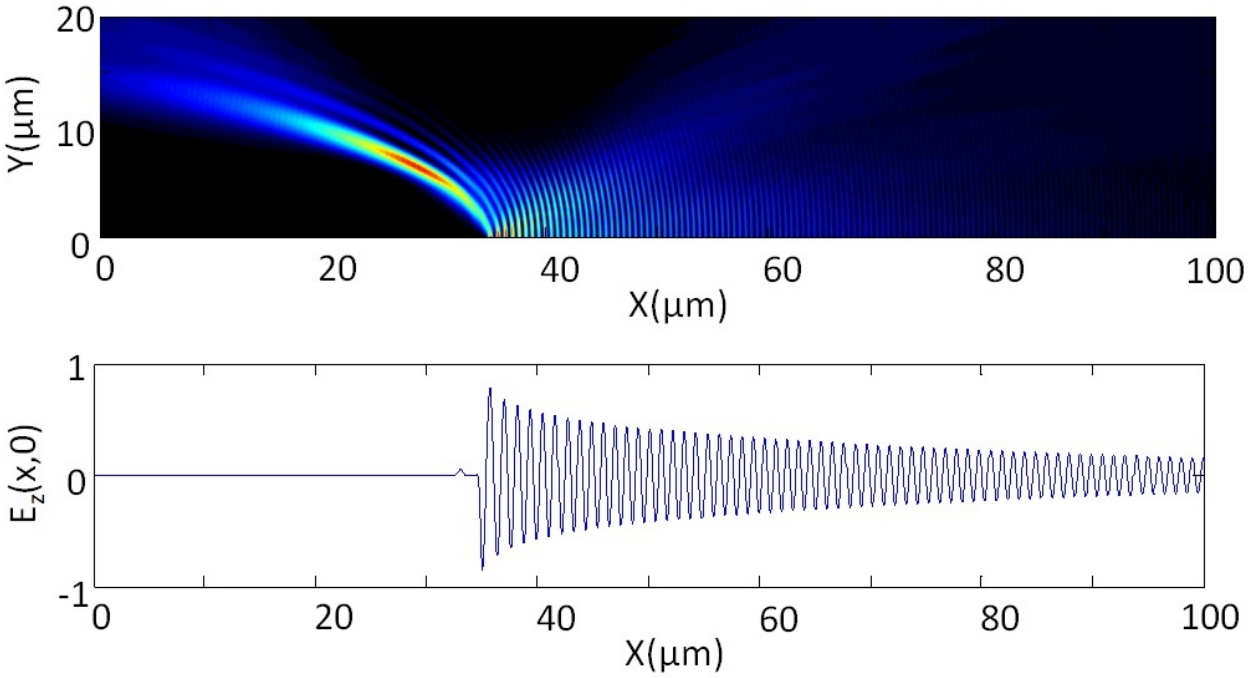

Figure. 6. 5 (color online). (a) Self-healing property of a truncated Mathieu beam (b), when it is launched from the major axis, with $m = 150$, $q = 10^4$, and with its main lobe initially truncated.

In our experiments, elliptic Mathieu beams were generated in the Fourier domain by appropriately imposing a phase function through a spatial light modulator. In this setup a broad Gaussian beam from a continuous-wave $\lambda = 633\, nm$ laser source was used. The resulting phasemodulated wave was then demagnified and projected onto the back focal plane of a 60 × objective lens in order to produce the Mathieu function in the spatial domain. Subsequently the

evolution of this beam was monitored along the propagation direction using a $60\times$ objective lens and a CCD camera. Figure 6. 6 (a) depicts experimental results associated with the intensity profile of a Mathieu elliptic beam when $m = 1400$ and $q = 2.5 \times 10^5$. In this case, the phase mask was judiciously designed so as to launch this elliptic beam toward the major axis (where apogee was reached) under the constraint of a limited numerical aperture($\sim$0.7), arising from the first lens in the system. This beam was found to intersect again the horizontal launching line after $200\ \mu m$. Conversely, when this same beam was launched in a complementary fashion, its apogee was attained on the minor axis, Fig. 6. 6 (b). In both cases the elliptic trajectory is clearly apparent. The fact that the intensity of this elliptic beam is maximum on the major axis is also evident, in accord with theoretical predictions [Fig. 6. 4 (d)]. These results are in good agreement with their corresponding simulations presented in Figs. 6. 6 (c) and (d).

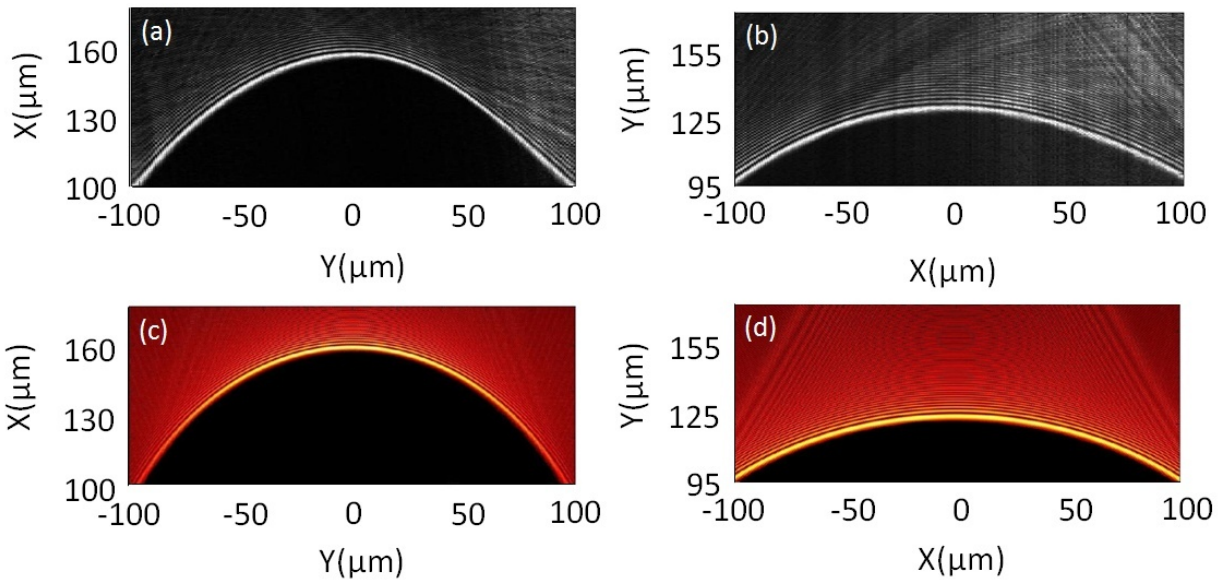

Figure. 6. 6 (color online). Observed intensity profile of an elliptic Mathieu beam with $m = 1400$ and $q = 2.5 \times 10^5$ when propagating (a) toward the major axis and (b) minor axis. (c), (d) Corresponding theoretical simulations for the experimental results in (a),(b).

6.5. Dynamics of Helmholtz beam in spherical and spheroidal coordinate in 3D

Apart from the aforementioned two-dimensional accelerating diffraction-free solutions, other more involved three-dimensional accelerating field configurations also exist. To demonstrate this possibility, we consider the Helmholtz equation in its more general form. To treat this problem we introduce auxiliary magnetic and electric vector potentials, $\boldsymbol{A}$ and $\boldsymbol{F}$, through which one can recover the electrodynamic field components,[92] i.e.,

$$\boldsymbol{E} = -\nabla \times \boldsymbol{F} - \frac{1}{i\omega\epsilon}\nabla \times \nabla \times \boldsymbol{A} \quad (6.20)$$

$$\boldsymbol{H} = +\nabla \times \boldsymbol{A} - \frac{1}{i\omega\mu}\nabla \times \nabla \times \boldsymbol{F}\,.$$

By employing a proper Lorentz gauge along with their respective scalar potentials, one arrives at a vectorial Helmholtz equation for the vector potentials, $\nabla^2\{\boldsymbol{A},\boldsymbol{F}\} + k^2\{\boldsymbol{A},\boldsymbol{F}\} = 0$. Pertinent solutions to the underlying Maxwell equations can be obtained by separately considering transverse electric and transverse magnetic field arrangements. For example if we set $\boldsymbol{A} = 0$, $\boldsymbol{F} = \hat{y}\psi$ this leads to a transverse electric solution with respect to y, i.e., $E_y = 0$. On the other hand, if $\boldsymbol{A} = \hat{y}\psi$, $\boldsymbol{F} = 0$, a transverse magnetic field mode is established with respect to y, implying that the y component of magnetic field is now zero. In both cases the scalar function ψ satisfies $\nabla^2\psi + k^2\psi = 0$.

In spherical coordinates, this latter scalar Helmholtz problem can be directly solved. More specifically, we find

$$\psi(x,y,z) = j_n(kr)P_n^m(cos\theta)e^{im\phi} \quad (6.\ 21)$$

where $j_n(x)$ represents spherical Bessel functions of the first kind, of order n, $P_n^m(x)$ stands for associated Legendre polynomials of degree n with $-n \le m \le n$, and k denotes the free space wavenumber. From here, $\{\boldsymbol{E},\boldsymbol{H}\}$ can be deduced from Eqs.(6. 5. 1) depending on whether the

mode is TE or TM. Figures 6. 7 (a) and 6. 7 (b) show two-dimensional profiles of the electric vector potential $\boldsymbol{F}$ associated with a TE field configuration when $m = n = 50$ and $n = 50$, $m = 49$, respectively. The corresponding diffraction-free dynamics resulting from apodized versions of these beams are shown in Figs. 6. 7 (c) and (d) when launched in the $x - z$ plane. These five-component vectorial waves propagate in a self-similar fashion within the first quadrant of the $x - y$ plane, by revolving around the z axis. The TM case can be similarly analyzed.

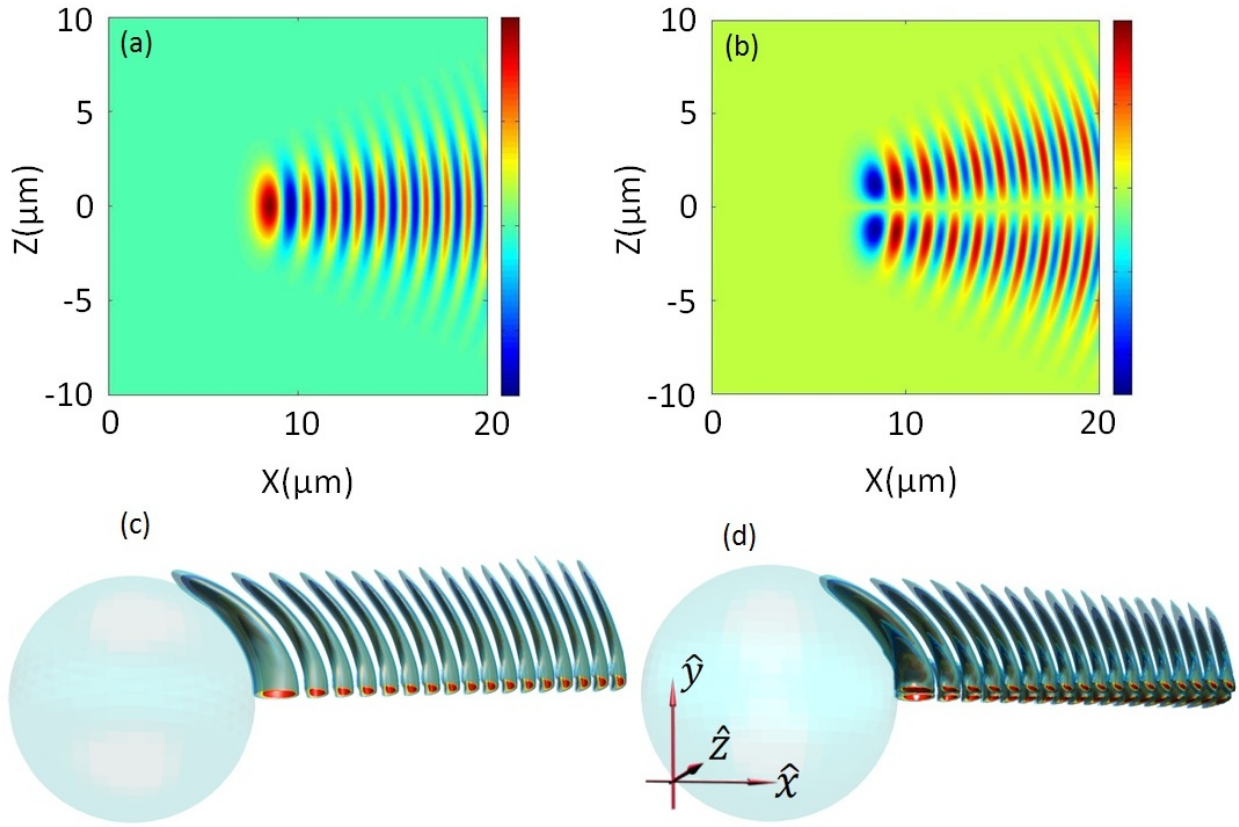

Figure. 6. 7 (color online). Two-dimensional cross section of the TE mode electric vector potential F associated with spherical coordinates when (a) $m = n = 50$ and (b) $n = 50;\ m = 49$. (c),(d) Accelerating diffraction-free dynamics when an apodized beam in (a),(b) is launched in the x-z plane.

Additional families of three-dimensional accelerating solutions also exist in other coordinate systems. For example, by adopting prolate spheroidal coordinates, (ξ, η, ϕ), the scalar function

ψ can be determined and is given by $\psi = R_{mn}(\xi,\gamma)S_{mn}(\eta,\gamma)e^{im\phi}$ where $\gamma = fk/2$ with f being the semifocal distance in this system. In the last equation, R_{mn} , S_{mn} represent radial and angular prolate spheroidal wavefunctions of orders m,n. Figure 6.8 (a) provides a two-dimensional plot of the electric vector potential **F** associated with a TE accelerating mode, within the $x-z$ plane. The dynamical evolution of this beam (after a Gaussian apodization) is depicted in figure 6.8 (b). The self-similar behavior of this field distribution is again evident. Similarly, accelerating solutions in oblate spheroidal coordinates can also be found under TE or TM conditions.

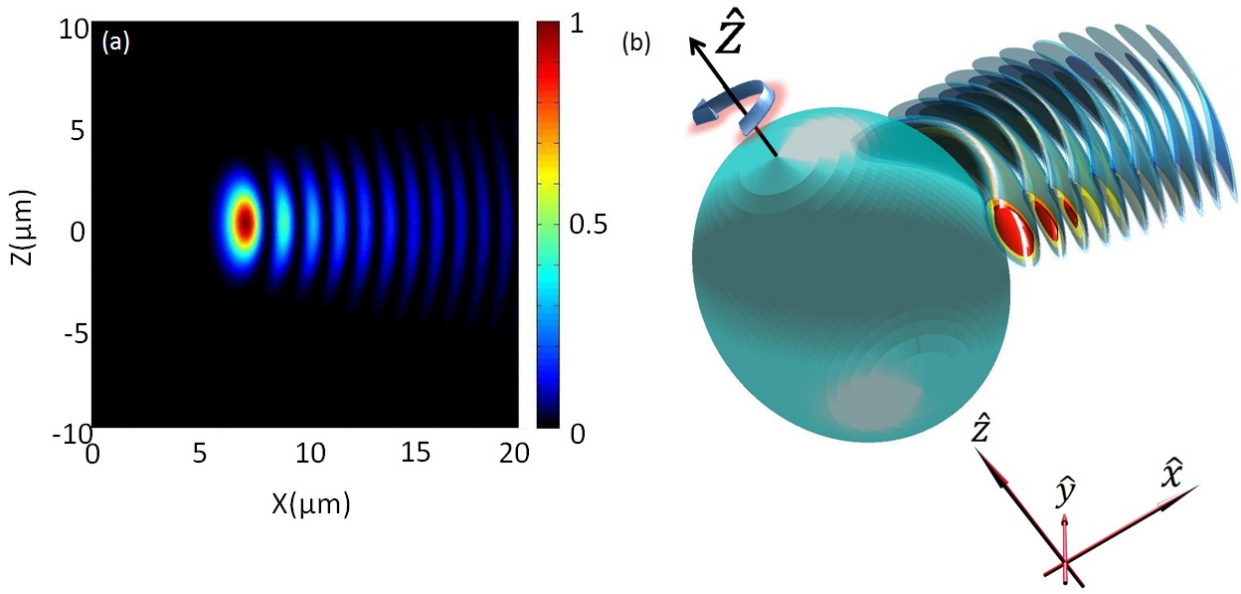

Figure. 6.8. (Color online). (a) Two dimensional profile associated with the electric vector potential F in prolate spheroidal coordinates when *m* = *n* = 30 and = 20. (b) Dynamical evolution of this beam when launched in the x-z plane.

LIST OF REFERENCES

1. Bi, L., et al., *On-chip optical isolation in monolithically integrated non-reciprocal optical resonators.* Nature Photonics, 2011. **5**(12): p. 758-762.
2. Shoji, Y., et al., *Magneto-optical isolator with silicon waveguides fabricated by direct bonding.* Applied Physics Letters, 2008. **92**(7): p. 071117.
3. Lira, H., et al., *Electrically Driven Nonreciprocity Induced by Interband Photonic Transition on a Silicon Chip.* Physical Review Letters, 2012. **109**(3).
4. Fan, L., et al., *An All-Silicon Passive Optical Diode.* Science, 2011. **335**(6067): p. 447-450.
5. Harrington, R.F., *Time-Harmonic Electromagnetic Fields*, ed. D.G. Dudley. 2001: Wiley-IEEE Press.
6. Ghosh, S., et al., *Ce:YIG/Silicon-on-Insulator waveguide optical isolator realized by adhesive bonding.* Optics Express, 2012. **20**(2): p. 1839.
7. Iwamura, H., S. Hayashi, and H. Iwasaki, *A compact optical isolator using a Y3Fe5O12 crystal for near infra-red radiation.* Optical and Quantum Electronics, 1978. **10**(5): p. 393-398.
8. Shiraishi, K., S. Sugaya, and S. Kawakami, *Fiber Faraday rotator.* Applied Optics, 1984. **23**(7): p. 1103.
9. Tien, M.-C., et al., *Silicon ring isolators with bonded nonreciprocal magneto-optic garnets.* Optics Express, 2011. **19**(12): p. 11740.
10. LiKamWa, P., et al., *130 ps recovery of all-optical switching in a GaAs multiquantum well directional coupler.* Applied Physics Letters, 1991. **58**(19): p. 2055.
11. Peng, B., et al., *Parity–time-symmetric whispering-gallery microcavities.* Nature Physics, 2014. **10**(5): p. 394-398.
12. Chang, L., et al., *Parity–time symmetry and variable optical isolation in active–passive-coupled microresonators.* Nature Photonics, 2014. **8**(7): p. 524-529.
13. Wang, J., et al., *A Theoretical Model for an Optical Diode Built With Nonlinear Silicon Microrings.* Journal of Lightwave Technology, 2013. **31**(2): p. 313-321.
14. Fan, L., et al., *Silicon optical diode with 40 dB nonreciprocal transmission.* Optics Letters, 2013. **38**(8): p. 1259.
15. Nazari, F., et al., *Optical isolation via 𝒫𝒯 -symmetric nonlinear Fano resonances.* Optics Express, 2014. **22**(8): p. 9574.
16. Bender, N., et al., *Observation of Asymmetric Transport in Structures with Active Nonlinearities.* Physical Review Letters, 2013. **110**(23).
17. Miroshnichenko, A.E., E. Brasselet, and Y.S. Kivshar, *Reversible optical nonreciprocity in periodic structures with liquid crystals.* Applied Physics Letters, 2010. **96**(6): p. 063302.
18. Smith, R., *Use of the acoustooptic light deflector as an optical isolator.* IEEE Journal of Quantum Electronics, 1973. **9**(5): p. 545-546.
19. Ibrahim, S.K., et al., *Non-magnetic 30 dB integrated optical isolator in III/V material.* Electronics Letters, 2004. **40**(20): p. 1293.

20. Bhandare, S., et al., *Novel nonmagnetic 30-dB traveling-wave single-sideband optical isolator integrated in III/V material.* IEEE Journal of Selected Topics in Quantum Electronics, 2005. **11**(2): p. 417-421.
21. Yu, Z. and S. Fan, *Complete optical isolation created by indirect interband photonic transitions.* Nature Photonics, 2009. **3**(2): p. 91-94.
22. Gallo, K., et al., *All-optical diode in a periodically poled lithium niobate waveguide.* Applied Physics Letters, 2001. **79**(3): p. 314.
23. Kang, M.S., A. Butsch, and P.S.J. Russell, *Reconfigurable light-driven opto-acoustic isolators in photonic crystal fibre.* Nature Photonics, 2011. **5**(9): p. 549-553.
24. Doerr, C.R., N. Dupuis, and L. Zhang, *Optical isolator using two tandem phase modulators.* Optics Letters, 2011. **36**(21): p. 4293.
25. Svirko, Y.P. and N.I. Zheludev, *Reversality of optical interactions in noncentrosymmetric media.* Optics Letters, 1995. **20**(17): p. 1809.
26. Treviño-Palacios, C.G., G.I. Stegeman, and P. Baldi, *Spatial nonreciprocity in waveguide second-order processes.* Optics Letters, 1996. **21**(18): p. 1442.
27. Siviloglou, G.A. and D.N. Christodoulides, *Accelerating finite energy Airy beams.* Optics Letters, 2007. **32**(8): p. 979-981.
28. Siviloglou, G.A., et al., *Observation of accelerating airy beams.* Physical Review Letters, 2007. **99**(21): p. 213901.
29. Baumgartl, J., M. Mazilu, and K. Dholakia, *Optically mediated particle clearing using Airy wavepackets.* Nature Photonics, 2008. **2**(11): p. 675-678.
30. Ellenbogen, T., et al., *Nonlinear generation and manipulation of Airy beams.* Nature Photonics, 2009. **3**(7): p. 395-398.
31. Porat, G., et al., *Airy beam laser.* Optics Letters, 2011. **36**(20): p. 4119-4121.
32. Sztul, H.I. and R.R. Alfano, *The Poynting vector and angular momentum of Airy beams.* Optics Express, 2008. **16**(13): p. 9411-9416.
33. Froehly, L., et al., *Arbitrary accelerating micron-scale caustic beams in two and three dimensions.* Optics Express, 2011. **19**(17): p. 16455-16465.
34. Greenfield, E., et al., *Accelerating Light Beams along Arbitrary Convex Trajectories.* Physical Review Letters, 2011. **106**(21).
35. Dolev, I., T. Ellenbogen, and A. Arie, *Switching the acceleration direction of Airy beams by a nonlinear optical process.* Optics Letters, 2010. **35**(10): p. 1581-1583.
36. Besieris, I.M. and A.M. Shaarawi, *Accelerating Airy wave packets in the presence of quadratic and cubic dispersion.* Physical Review E, 2008. **78**(4).
37. Efremidis, N.K., *Airy trajectory engineering in dynamic linear index potentials.* Optics Letters, 2011. **36**(15): p. 3006-3008.
38. Berry, M.V. and N.L. Balazs, *Non-Spreading Wave Packets.* American Journal of Physics, 1979. **47**(3): p. 264-267.
39. Greenberger, D.M., *Nonspreading Wave-Packets - Comment.* American Journal of Physics, 1980. **48**(3): p. 256-256.
40. Polynkin, P., et al., *Curved Plasma Channel Generation Using Ultraintense Airy Beams.* Science, 2009. **324**(5924): p. 229-232.
41. Chong, A., et al., *Airy-Bessel wave packets as versatile linear light bullets.* Nature Photonics, 2010. **4**(2): p. 103-106.

42. Ament, C., P. Polynkin, and J.V. Moloney, *Supercontinuum Generation with Femtosecond Self-Healing Airy Pulses.* Physical Review Letters, 2011. **107**(24).
43. Salandrino, A. and D.N. Christodoulides, *Airy plasmon: a nondiffracting surface wave.* Optics Letters, 2010. **35**(12): p. 2082-2084.
44. Li, L., et al., *Plasmonic Airy Beam Generated by In-Plane Diffraction.* Physical Review Letters, 2011. **107**(12).
45. Minovich, A., et al., *Generation and Near-Field Imaging of Airy Surface Plasmons.* Physical Review Letters, 2011. **107**(11).
46. Zhang, P., et al., *Plasmonic Airy beams with dynamically controlled trajectories.* Optics Letters, 2011. **36**(16): p. 3191-3193.
47. Kaminer, I., M. Segev, and D.N. Christodoulides, *Self-Accelerating Self-Trapped Optical Beams.* Physical Review Letters, 2011. **106**(21).
48. Dolev, I., et al., *Experimental Observation of Self-Accelerating Beams in Quadratic Nonlinear Media.* Physical Review Letters, 2012. **108**(11).
49. Bekenstein, R. and M. Segev, *Self-accelerating optical beams in highly nonlocal nonlinear media.* Optics Express, 2011. **19**(24): p. 23706-23715.
50. Kaminer, I., et al., *Nondiffracting Accelerating Wave Packets of Maxwell's Equations.* Physical Review Letters, 2012. **108**(16).
51. Zhang, P., et al., *Generation of linear and nonlinear nonparaxial accelerating beams.* Optics Letters, 2012. **37**(14): p. 2820-2822.
52. Courvoisier, F., et al., *Sending femtosecond pulses in circles: highly nonparaxial accelerating beams.* Optics Letters, 2012. **37**(10): p. 1736-1738.
53. Aleahmad, P., et al., *Fully Vectorial Accelerating Diffraction-Free Helmholtz Beams.* Physical Review Letters, 2012. **109**(20): p. 203902.
54. Zhang, P., et al., *Nonparaxial Mathieu and Weber Accelerating Beams.* Physical Review Letters, 2012. **109**(19).
55. Daino, B., G. Gregori, and S. Wabnitz, *Stability analysis of nonlinear coherent coupling.* Journal of Applied Physics, 1985. **58**(12): p. 4512.
56. LiKamWa, P., et al., *All optical multiple-quantum-well waveguide switch.* Electronics Letters, 1985. **21**(1): p. 26.
57. Das, U., Y. Chen, and P. Bhattacharya, *Nonlinear effects in coplanar GaAs/InGaAs strained-layer superlattice directional couplers.* Applied Physics Letters, 1987. **51**(21): p. 1679.
58. Friberg, S.R., et al., *Ultrafast all-optical switching in a dual-core fiber nonlinear coupler.* Applied Physics Letters, 1987. **51**(15): p. 1135.
59. Berglund, W. and A. Gopinath, *WKB Analysis of Bend Losses in Optical Waveguides.* JOURNAL OF LIGHTWAVE TECHNOLOGY, 2000. **18**(8).
60. Melloni, A., et al., *Determination of Bend Mode Characteristics in Dielectric Waveguides.* JOURNAL OF LIGHTWAVE TECHNOLOGY. **19**(4).
61. Marcatili, E.A.J. and S.E. Miller, *Improved relations describing directional control in electromagnetic wave guidance.* Bell Syst. Tech. J. , 1969. **48**.
62. Espinola, R., et al., *A study of high-index-contrast 90 degree waveguide bend structures.* Optics Express, 2001. **8**(9): p. 517.
63. Song, W. and D. Psaltis, *Pneumatically tunable optofluidic 2 × 2 switch for reconfigurable optical circuit.* Lab on a Chip, 2011. **11**(14): p. 2397.

64. Fuchida, A., A. Matsutani, and F. Koyama, *Slow-light total-internal-reflection switch with bending angle of 30 deg.* Optics Letters, 2011. **36**(14): p. 2644-2646.
65. Orlic, S., et al., *<title>3D waveguides with fiber couplers and 90 degree bends in holographic photopolymer</title>*. 2007. **6657**: p. 66570F-66570F-6.
66. Zhang, R., Z. Ren, and S. Yu, *Fabrication of InGaAsP Double Shallow Ridge Rectangular Ring Laser With Total Internal Reflection Mirror by Cascade Etching Technique.* IEEE Photonics Technology Letters, 2007. **19**(21): p. 1714-1716.
67. Rao, S., W. Gillin, and K. Homewood, *Interdiffusion of the group-III sublattice in In-Ga-As-P/In-Ga-As-P and In-Ga-As/In-Ga-As heterostructures.* Physical Review B, 1994. **50**(11): p. 8071-8073.
68. Rao, E.V.K., et al., *New encapsulant source for III–V quantum well disordering.* Applied Physics Letters, 1995. **66**(4): p. 472.
69. Pepin, A., et al., *Evidence of stress dependence in SiO2/Si3N4 encapsulation-based layer disordering of GaAs/AlGaAs quantum well heterostructures.* Journal of Vacuum Science & Technology B, 1997. **15**(1): p. 142-153.
70. Choi, J., et al., *Dependence of dielectric-cap quantum-well disordering of GaAs-AlGaAs quantum-well structure on the hydrogen content in SiN/sub x/ capping layer.* IEEE Journal of Selected Topics in Quantum Electronics, 1998. **4**(4): p. 624-628.
71. Kowalski, O.P., et al., *A universal damage induced technique for quantum well intermixing.* Applied Physics Letters, 1998. **72**(5): p. 581.
72. Sang Kee, S., et al., *Area selectivity of InGaAsP-InP multiquantum-well intermixing by impurity-free vacancy diffusion.* IEEE Journal of Selected Topics in Quantum Electronics, 1998. **4**(4): p. 619-623.
73. Helmy, A.S., et al., *Control of silica cap properties by oxygen plasma treatment for single-cap selective impurity free vacancy disordering.* Applied Physics Letters, 1999. **74**(5): p. 732-734.
74. Liu, X.F., et al., *Control of multiple bandgap shifts in InGaAs-AlInGaAs multiple-quantum-well material using different thicknesses of PECVD SiO₂ protection layers.* IEEE Photonics Technology Letters, 2000. **12**(9): p. 1141-1143.
75. Lee, A.S.W., et al., *Enhanced band-gap blueshift due to group V intermixing in InGaAsP multiple quantum well laser structures induced by low temperature grown InP.* Applied Physics Letters, 2001. **78**(21): p. 3199.
76. Teng, J.H., et al., *Controlled group V intermixing in InGaAsP quantum well structures and its application to the fabrication of two section tunable lasers.* Journal of Applied Physics, 2002. **92**(8): p. 4330.
77. Choi, W.J., et al., *Dependence of the intermixing in InGaAs/InGaAsP quantum well on capping layers.* Journal of the Korean Physical Society, 2004. **45**(3): p. 773-776.
78. Skogen, E.J., et al., *Multiple-band-edge quantum-well intermixing in the InGaAs/InGaAsP/InGaP material system.* Applied Physics Letters, 2005. **86**(24): p. 241117.
79. Helmy, A.S., et al., *Spatially resolved photoluminescence and Raman spectroscopy of bandgap gratings fabricated in GaAs/AlAs superlattice waveguide using quantum well intermixing.* Journal of Crystal Growth, 2006. **288**(1): p. 53-56.
80. Yu, J.S. and Y.T. Lee, *Impurity-free vacancy diffusion of InGaAsP/InGaAsP multiple quantum well structures using SiH4-dependent dielectric cappings.* Japanese Journal of

Applied Physics Part 1-Regular Papers Brief Communications & Review Papers, 2007. **46**(10A): p. 6509-6513.
81. May-Arrioja, D.A., et al., *Intermixing of InP-based multiple quantum wells for integrated optoelectronic devices.* Microelectronics Journal, 2009. **40**(3): p. 574-576.
82. McKerracher, I., et al., *Intermixing of InGaAs/GaAs quantum wells and quantum dots using sputter-deposited silicon oxynitride capping layers.* Journal of Applied Physics, 2012. **112**(11): p. 113511.
83. Bickel, N. and P. LikamWa, *Enhanced control over selective-area intermixing of In0.15Ga0.85As/GaAs quantum dots through post-growth exposure to radio-frequency plasma.* Thin Solid Films, 2011. **519**(6): p. 1955-1959.
84. Yu, S.F. and E.H. Li, *Semiconductor lasers using diffused quantum-well structures.* Ieee Journal of Selected Topics in Quantum Electronics, 1998. **4**(4): p. 723-735.
85. Kim, C., et al., *Ultrafast all-optical multiple quantum well integrated optic switch.* Electronics Letters, 2000. **36**(23): p. 1929-1930.
86. Choy, W.C.H. and K.S. Chan, *Theoretical analysis of diffused quantum-well lasers and optical amplifiers.* Ieee Journal of Selected Topics in Quantum Electronics, 2003. **9**(3): p. 698-707.
87. Taniguchi, H., et al., *25-W 915-nm lasers with window structure fabricated by impurity-free vacancy disordering (IFVD).* Ieee Journal of Selected Topics in Quantum Electronics, 2007. **13**(5): p. 1176-1179.
88. Zhao, J., et al., *Spatial control based quantum well intermixing in InP/InGaAsP structures using ICP.* Journal of Semiconductors, 2012. **33**(10): p. 106001.
89. Hakki, B.W. and T.L. Paoli, *Gain spectra in GaAs double−heterostructure injection lasers.* Journal of Applied Physics, 1975. **46**(3): p. 1299.
90. Oberhettinger, F., *Tables of Fourier Transforms and Fourier Transforms of Distributions*. 1990, Berlin: Springer-Verlag.
91. Abramowitz, M. and I. Stegun, *Handbook of Mathematical Functions* 1972, New York: Dover.
92. Harrington, R.F., *Time-harmonic electromagnetic fields*. IEEE Press series on electromagnetic wave theory. 2001, New York: IEEE Press : Wiley-Interscience. xiii, 480 p.